

**HEAT TRANSFER IN NANO/MICRO MULTI-COMPONENT AND
COMPLEX FLUIDS WITH APPLICATIONS TO HEAT TRANSFER
ENHANCEMENT**

A Dissertation
Presented to
The Academic Faculty

by

Reza Haji Aghaee Khiabani

In Partial Fulfillment
of the Requirements for the Degree
Doctor of Philosophy in the
G.W. Woodruff School of Mechanical Engineering

Georgia Institute of Technology
August 2010

**HEAT TRANSFER IN NANO/MICRO MULTI-COMPONENT AND
COMPLEX FLUIDS WITH APPLICATIONS TO HEAT TRANSFER
ENHANCEMENT**

Approved by:

Dr. Yogendra Joshi, Co-Advisor

School of Mechanical Engineering

Georgia Institute of Technology

Dr. Cyrus Aidun, Co-Advisor

School of Mechanical Engineering

Georgia Institute of Technology

Dr. Mostafa Ghiaasiaan

School of Mechanical Engineering

Georgia Institute of Technology

Dr. David Bader

College of Computing

Georgia Institute of Technology

Dr. Thorsten Stoesser

School of Civil and Environmental
Engineering
Georgia Institute of Technology

Date Approved: May 28, 2010

*To my parents
for their love, endless support and encouragement.*

ACKNOWLEDGEMENTS

I would like to express my sincere thanks to my advisors, Dr. Yogendra Joshi and Dr. Cyrus Aidun, for their support, guidance and encouragement during my doctoral studies. I am grateful for their insight and career advice, but most of all their confidence in me. I am also grateful to my dissertation committee members, Dr. Bader, Dr. Stoesser, and Dr. Ghiaasiaan for their valuable suggestions and commitment to this dissertation. I am thankful for all my colleagues in Microelectronics and Emerging Technologies Thermal Laboratory and Lattice Boltzmann Research Group for the valuable discussions we have had concerning this and many other research topics. I acknowledge the support of IPST and also the TIM Consortium at Georgia Institute of Technology. I acknowledge National Science Foundation for supporting this research in part through TeraGrid resources.

I would like to express my appreciation to my family for their love and encouragement.

TABLE OF CONTENTS

ACKNOWLEDGEMENTS	III
LIST OF TABLES	VIII
LIST OF FIGURES	IX
NOMENCLATURE	XIII
List of Symbols	xiii
List of Abbreviations	xvii
SUMMARY	XVIII
CHAPTER 1 INTRODUCTION	1
1.1 Objectives	4
CHAPTER 2 THERMAL LATTICE BOLTZMANN METHODS	6
2.1 Lattice Boltzmann Method	6
2.2 Thermal Lattice Boltzmann Methods	9
2.2.1 Multispeed Approach	10
2.2.2 Double Distribution Function or Passive Scalar Approach	11
2.2.3 Further Developments of TLBM	12
2.3 Thermal Lattice Boltzmann Model to Simulate Heat Transfer in Suspension Flows	14

CHAPTER 3 MODELING HEAT TRANSFER IN SUSPENSION FLOWS	
USING LATTICE BOLTZMANN METHOD COUPLED WITH ENERGY	
EQUATION	18
3.1 Sample Problem and Validation	18
3.2 Parallel Computation Implementation	25
3.2.1 Programming Style and Code Performance	27
CHAPTER 4 HEAT TRANSFER IN SUSPENSION FLOW IN	
MICROCHANNELS	
	33
4.1 Convective Heat Transfer in Suspensions	33
4.2 Problem Description	35
4.3 Detail Study of Effect of Individual Particles on Heat Transfer from	
Channel Walls	37
4.3.1 Effect of a single particle	37
4.3.2 Effects of multiple particles	43
4.3.3 Effect of a particle moving with a constant velocity	44
4.3.4 Effect of freely suspended particles	45
4.4 Large Domain Simulation Results	49
4.4.1 Effect of Particle Volume Fraction	58
4.4.2 Effect of Reynolds Number	59
4.4.3 Effect of Particle Thermal Conductivity	61
4.4.4 Effect of Particle Size	61
CHAPTER 5 HEAT TRANSFER IN HOT PRESS SECTION OF A PAPER	
MAKING MACHINE	
	63

5.1	Energy Consumption in Drying and the Effect of Hot Pressing	64
5.2	Modeling Hot Pressing of Fiber Suspension	68
5.2.1	Previous Experimental and Numerical Studies	69
5.2.2	Problem Description	70
5.2.3	Method Validation and Results	73
5.2.4	Effect of Temperature and Solid content on Effective Thermal Conductivity	79
5.2.4.1	Effect of Moisture Ratio on k_{eff}	79
5.2.4.2	Effect of Temperature on k_{eff}	80
5.2.5	Modeling Paper Sheet as a Semi-Infinite Body	82
CHAPTER 6 THERMAL PROPERTIES OF PARTICLE LADEN		
MIXTURES IN SQUEEZE FLOW		
		87
6.1	Thermal Interface Materials	87
6.2	Problem Description	92
6.3	Simple Cubic Arrangement	95
6.4	Microstructure and Particle Distribution	97
6.5	Effective Thermal Conductivity of TIM	101
6.5.1	Effect of Particle Size on TIM conductivity	103
6.5.2	Effect of Particle Shape on TIM conductivity	104
6.5.3	Effect of Particle Conductivity on TIM conductivity	108
CHAPTER 7 CONCLUDING REMARKS		
		110
7.1	Recommended Future Work	114
REFERENCES		
		116

LIST OF TABLES

Table 3.1. Strong scaling results on Mercury. The domain size is 128^3 cube.	31
Table 3.2. Strong scaling results on Steele. The domain size is 128^3 cube. ($\phi=5\%$).....	32
Table 5.1. Effect of consistency on energy usage	68
Table 5.2. Properties of wood fibers	72
Table 5.3. Minimum BW for validity of semi-infinite body modeling for Swedish softwood pulp ($t<50$ ms)	85
Table 5.4. Minimum BW for validity of semi-infinite body modeling for southern pine pulp ($t<50$ ms)	86

LIST OF FIGURES

Figure 2.1. Illustration of 18 directions in D3Q19 model	8
Figure 2.2. Bounce-back boundary condition	17
Figure 3.1. Comparing a) horizontal and b) vertical velocity and c) temperature profile for different lattice units	21
Figure 3.2. Streamlines and isotherms around a hot particle at a) $Re=5$, and b) $Re=50$	23
Figure 3.3. Snapshots of streamlines and isotherms around a hot particle at $Re=110$	24
Figure 3.4. Variation of average Nu with Re	25
Figure 3.5. Schematic of shared memory architecture	26
Figure 3.6. Schematic of distributed memory architecture.....	26
Figure 3.7. Schematic of Cartesian sub-domains and ghost cells.....	27
Figure 3.8. Strong scaling on Mercury. The domain size is 128^3 cube.	29
Figure 3.9. Efficiency of strong scaling on Mercury. The domain size is 128^3 cube.	30
Figure 3.10. Simulation run-time on Mercury. The domain size is 128^3 cube.	30
Figure 3.11. Strong scaling on Steele. The domain size is 128^3 cube. ($\phi=5\%$).....	31
Figure 3.12. Efficiency of strong scaling on Steele. The domain size is 128^3 cube. ($\phi=5\%$).....	32
Figure 4.1. Schematic of the physical domain.....	36
Figure 4.2. Streamlines and isotherms in a) an unblocked channel, and b) a channel containing a stationary particle.....	38
Figure 4.3. Streamlines and isotherms in a channel containing a particle a) moving with constant velocity, and b) freely suspended.....	39
Figure 4.4. Local Nu distribution along the channel wall; $b=35\%$	40
Figure 4.5. Effect of Re on Nu (stationary particle); $b=35\%$	41
Figure 4.6. Effect of blockage ratio on Nu (stationary particle); $Re=40$	42
Figure 4.7. Effect of Eccentricity on Nu (stationary particle); $Re=40$ and $b=35\%$	43
Figure 4.8. Nu distribution (multiple stationary particles); $Re=40$	44
Figure 4.9. Nu distribution for particle moving with const. velocity; $b=35\%$	45

Figure 4.10. Nu distribution at different times (freely suspended particle); Re=45 and b=35%.....	46
Figure 4.11. Effect of Re on Nu distribution; b=35%	47
Figure 4.12. Effect of blockage ratio on Nu (suspended particle); Re=110	48
Figure 4.13. Nu distributions for a fluid containing several suspended particles; Re=220 and b=6%.....	49
Figure 4.14. Computational domain decomposition.....	50
Figure 4.15. Particle distribution in a sample sub-domain at different times ($\phi=1\%$).....	52
Figure 4.16. The effect of flow disturbance caused by moving particles on the temperature field in a sample sub-domain at different times ($\phi=1\%$).....	53
Figure 4.17. Temperature field in a sample sub-domain (no solid particles)	54
Figure 4.18. Particle distribution in a sample sub-domain at different times ($\phi=5\%$).....	54
Figure 4.19. The effect of flow disturbance caused by moving particles on the temperature field in a sample sub-domain at different times ($\phi=5\%$).....	55
Figure 4.20. Comparing temperature field in a vertical plane in flow with 0, 1 and 5% solid particles	56
Figure 4.21. Wall Nusselt number at different times (no suspensions).....	57
Figure 4.22. Wall Nusselt number at different times ($\phi=5\%$)	57
Figure 4.23. Comparing wall Nusselt number at different times.....	58
Figure 4.24. Effect of volume fraction on Nu	59
Figure 4.25. Effect of Re on Nu	60
Figure 4.26. Effect of volume fraction and Re on Nu	60
Figure 4.27. Effect of particle size on Nu.....	62
Figure 5.1. Different sections in paper making machine.....	63
Figure 5.2. Effect of temperature on dynamic viscosity of water.....	66
Figure 5.3. Schematic of hot pressing of fiber suspension	71
Figure 5.4. Effect of temperature on water thermal conductivity.....	72
Figure 5.5. Effect of temperature on water Prandtl number	73
Figure 5.6. Temperature in paper sheet at 2/3 of caliper; $T_w=100\text{ }^\circ\text{C}$	74
Figure 5.7. Temperature in paper sheet at 2/3 of caliper; $T_w=150\text{ }^\circ\text{C}$	75
Figure 5.8. Temperature in paper sheet at 1/3 of caliper; $T_w=150\text{ }^\circ\text{C}$	75

Figure 5.9. Temperature in Swedish softwood pulp paper sheet; $T_w=100\text{ }^\circ\text{C}$	76
Figure 5.10. Temperature in Swedish softwood pulp paper sheet; $T_w=150\text{ }^\circ\text{C}$	77
Figure 5.11. Temperature in southern pine paper sheet; $T_w=100\text{ }^\circ\text{C}$	78
Figure 5.12. Temperature in southern pine paper sheet; $T_w=150\text{ }^\circ\text{C}$	78
Figure 5.13. Effect of MR on k_{eff}	79
Figure 5.14. Effect of solids on k_{eff}	80
Figure 5.15. Effect of temperature on k_{eff}	81
Figure 5.16. Effect of Swedish softwood pulp consistency and temperature on k_{eff}	82
Figure 5.17. Non-dimensional temperature in a paper with $c=180\text{ }\mu\text{m}$	84
Figure 5.18. Non-dimensional temperature at unheated surface	84
Figure 5.19. Non-dimensional temperature at unheated surface for Swedish softwood pulp at $\text{BW}=120\text{ g/m}^2$	85
Figure 6.1. Different models for the effective thermal conductivity of a particle laden TIM	91
Figure 6.2. Schematic of the physical domain.....	93
Figure 6.3. Particle distribution before (a), and after (b), squeezing	94
Figure 6.4. Effective thermal conductivity for simple cubic arrangement; $\frac{k_f}{k_m} = 10$	96
Figure 6.5. Effective thermal conductivity for simple cubic arrangement; $\frac{k_f}{k_m} \gg 1$	96
Figure 6.6. Particle distribution before (left) and after (right) 10% squeezing. a) three dimensional particle distribution, b) particle distribution projection at the horizontal plane ($x_2=0$), c) particle distribution , and d) temperature profile at the vertical (x_1-x_2) center plane.....	98
Figure 6.7. (a) particle stacking lines in the diagonal directions (adapted from Linderman et al. [14, 17]), (b) velocity vectors, and (c) temperature distribution in x_1-x_3 mid-plane	100
Figure 6.8. Effect of particle volume fraction on TIM effective thermal conductivity	101
Figure 6.9. Effect of particle size on TIM effective thermal conductivity	104
Figure 6.10. Effect of particle aspect ratio on TIM effective conductivity, $\phi=20\%$	106
Figure 6.11. Effect of particle aspect ratio on TIM effective conductivity, $\phi=40\%$	107

Figure 6.12. Effect of particle aspect ratio on TIM effective conductivity 107

Figure 6.13. Effect of particle thermal conductivity on TIM effective thermal conductivity..... 109

NOMENCLATURE

List of Symbols

AR	aspect ratio
b	blockage ratio
BLT	bond line thickness, m
BW	basis weight
c	caliper, m
c_p	specific heat, J/kg.K
d	diameter, m
D	diffusivity
e	eccentricity
\mathbf{e}	unit velocity vector
f	distribution function
F	force, N
h	convective heat transfer coefficient, W/m ² .K

H	channel height, m
I	inertia, kg.m^2
k	thermal conductivity, W/m.K
k_B	Boltzmann constant
K	permeability
L	channel length, m
m	mass, kg
M	mass, kg
MR	moisture ratio
Nu	Nusselt number
OD	oven dried
p	pressure, Pa
Pe	Peclet number
Pr	Prandtl number
q	heat flux, W/m^2
r	radius, m

R	thermal resistance, K/W
Re	Reynolds number
S	consistency, solids
t	time, s
T	temperature, K
T	torque, N.m
u	fluid velocity vector
U	particle velocity
x	position vector

Greek Symbols

α	Biot number, thermal diffusivity (m^2/s)
γ	shear strain
ε	internal energy per unit mass, J/kg
η	efficiency
θ	non dimensional temperature
μ	dynamic viscosity, N.s/m ²

ρ	density, kg/m ³
τ	relaxation time
ν	kinematic viscosity, m ² /s
ϕ	volume fraction
ω, Ω	angular velocity, 1/s

Subscripts

ave	average
b	boundary
c	contact, cold
eff	effective
f	filler, fiber
i	initial
in	inlet
m	matrix, mean
N	number of processors
th	thermal

w wall, water

List of Abbreviations

BTE Boltzmann Transport Equation

CNT Carbon Nano Tube

Flops Floating Point Operations Per Second

LBE Lattice Boltzmann Equation

LBM Lattice Boltzmann Method

MPI Message Passing Interface

TIM Thermal Interface Material

TLBM Thermal Lattice Boltzmann Method

SUMMARY

Suspension fluids are a class of complex fluids which are extensively used in industrial and biological systems. Examples of such fluids are nano/micro fluids, fiber suspensions in a paper making machine, particle filled thermal interface materials, food products, fluidized beds, chemical products and biological systems. The thermo-physical properties of these fluids are different from the pure fluids. Due to the various applications of such mixtures, it is important to determine the properties of the resultant complex fluid. In this research, thermal properties of complex suspension flows are investigated using numerical computations.

The objective of this research is to develop an efficient and accurate computational method to investigate heat transport in suspension flows. The method presented here is based on solving the lattice Boltzmann equation for the fluid phase, as it is coupled to the Newtonian dynamics equations to model the movement of particles and the energy equation to find the thermal properties. This is a direct numerical simulation that models the free movement of the solid particles suspended in the flow and its effect on the temperature distribution. This is a robust and efficient computational method for the analysis of solid particles suspended in fluid. An advantage of the lattice Boltzmann method is that the code can be easily implemented on parallel processors because of the local nature of the time evolution operator. Here, parallel implementations are done using MPI (message passing interface) method. Teragrid super computing resources have been used for large domain simulations.

In this study, convective heat transfer in internal suspension flow (low solid volume fraction, $\phi < 10\%$), heat transfer in hot pressing of fiber suspensions and thermal performance of particle filled thermal interface materials (high solid volume fraction, $\phi > 40\%$) are investigated. The effect of different parameters such as particle size or thermal conductivity on thermal performance is discussed. The results have been compared to previous experimental, analytical or numerical studies. Large domain simulations show that the flow disturbance due to movement of suspended particles is the main reason for local and overall thermal enhancements in convective heat transfer of internal suspension flows. The results show that the heat transfer rate is enhanced about 10% at 5% particle volume fraction.

Hot pressing of wood fiber suspensions is studied numerically. It is shown that effective pre-heating of fiber suspensions can lead to considerable energy savings in paper making process. The results show that the thermal properties are highly dependent on the wood fiber type. The effective thermal conductivity changes about 45% for suspensions of different softwood and hardwoods at 20-40% of solid fiber contents.

Detail study of particle laden thermal interface materials (a dense suspension) in squeeze flow, shows that the microstructure changes in assembly process. This affects the thermal properties and needs to be considered for realistic thermal predictions. The results show that effective thermal conductivity is enhanced 2-7 times at $\phi = 55\%$ depending on particle size and conductivity. It is also shown that using ellipsoidal particles with aspect ratio=4 enhances the thermal conductivity 2.5 times compared to a mixture with spherical particles at $\phi = 60\%$.

CHAPTER 1

INTRODUCTION

Mixing solid particles in a liquid forms a multi component fluid. The thermo-physical properties of these complex fluids are different from the base fluid. Due to the various applications of such mixtures, it is important to determine the properties of the resultant complex fluid. Nano/micro fluids, particle filled thermal interface materials or fiber suspensions in a paper making machine are examples of such fluids.

A nanofluid is a mixture of suspended highly conducting nano/micro size solid particles (such as Al_2O_3 or CuO) in a base liquid such as water. Because of the high thermal conductivity of the solid particles it is expected that the mixture results in a cooling medium with improved thermal properties [1-5]. It is a promising cooling solution for future high heat dissipating systems such as micro mechanisms or biological and electronic devices. The thermal conductivity models for composites such as the Maxwell-Garnett [6] model cannot predict the thermal conductivity in nanofluids [2, 7, 8]. Several mechanisms and models have been presented in the literature as the possible explanation for the heat transfer enhancement in nanofluids [2, 9, 10]. Some of the presented mechanisms are [7]: simple conduction through the liquid and solid composite; ordered layering of liquid near the solid particle; thermal energy transfer due to translational Brownian motion; thermal energy transfer due to the existence of an inter particle potential; thermophoresis, and localized convection in the liquid due to the

Brownian movement of the particles. None of these explanations are proved to be the primary reason for the improved thermal properties of nanofluid.

The analytical or semi-empirical models usually result in complicated and inaccurate correlations that are valid under limited conditions [11, 12]. Furthermore, there is no general agreement in the literature on the amount of enhancement in the thermal properties. Experimental results having uncertainties cannot be used as the primary source for determining the mechanism of heat transfer or in determining the design parameters [3]. However, experimental validations are critical for confirming any model or explanation. The need for an accurate numerical simulation that can explain the heat transfer enhancement mechanism is stated in the literature[7].

Another example of advanced complex fluids which is extensively used is particle filled thermal interface material (TIM). Particle laden TIMs are used extensively in electronics components to enhance the heat transfer between heat dissipating components such as chips and the thermal packaging components such as heat spreaders [13]. TIM is placed between the contacting heat transfer surfaces and goes through a squeezing step. The thermal conductivity of the TIM is around 0.1-0.4 W/mK. Adding solid particles with high thermal conductivity will increase the bulk thermal conductivity. Improvements of 5-10 times in effective thermal conductivity have been reported in the literature using particle filled TIM. Effective bulk thermal conductivity of 2-5 W/mK are reported to be common in the industry [14].

Thermal conductivity of thermal interface materials is believed to depend on the particle loading and other physical properties of the particles such as thermal conductivity

and size. Increasing the particle loading will also affect the viscosity of the thermal grease and the minimum bond line thickness (BLT) [15]. Increasing BLT on the other hand will increase the thermal resistance which is not desired. Indeed, it has been shown that above a certain particle volume fraction, the thermal resistance of TIM will increase [16]. Linderman et al. have designed Hierarchical nested surface channels to reduce the BLT at a certain applied pressure [17]. Zhou et al. [18] have derived a model for bond line thickness based on a Newtonian fluid assumption . This type of correlations fail to predict experiments, especially at high particle loading since the particle laden TIM is non-Newtonian. Particle laden TIMs have a strain rate dependent viscosity and also have a yield stress. Prasher et al. [19] have derived a correlation to predict the thermal resistance of TIM based on empirical and analytical models assuming it to be a Herschel-Bulkley fluid. For the effective thermal conductivity they applied the relation presented by Every et al. [20].The results are consistent with the experimental results for higher particle loading up to fifty percent. On the other hand, there are parameters in the correlation that must be determined or assumed.

Water removal from a wet fibrous web is a critical operation in papermaking. For each kilogram of paper produced, typically more than 200 liters of water enters a paper machine. Most of this water is removed by drainage and mechanical pressing. Only a few percent of this water must be removed by evaporation, but doing so uses most of the energy needed for papermaking and requires a vast amount of equipment. There is a strong economic incentive for improved water removal techniques which can save energy and may also lead to better paper properties. Improved paper properties can mean new

markets, or can allow a papermaker to meet specifications by using an alternative source of fibers.

The fiber suspension in the hot press section can be assumed as a multi component flow containing long solid/deformable fibers under squeeze flow. Understanding and characterizing the heat transfer from the hot pressing cylinder through the suspension can lead to improvements in the drying section and increase the overall efficiency.

1.1 Objectives

Considering the above discussion, developing an efficient and accurate numerical model that can predict the thermal properties of multi-component fluids is important and has applications in many areas. It also helps in explaining the mechanism behind the observed thermal properties of this kind of fluids. The objective of this study is to develop a numerical method based on lattice Boltzmann method for modeling heat transfer in suspension flows. The method is used to investigate heat transfer in several systems. Three special cases are considered: suspension flow in microchannels, hot pressing of fiber suspensions, and squeeze flow of thermal interface materials.

In Chapter 2, Lattice Boltzmann method is described. The extensions to the method and development of Thermal Lattice Boltzmann method are outlined. Chapter 3 includes sample problems to validate the method and its accuracy. It also includes the details of parallel computation implementations and benchmark studies on computer clusters. In Chapter 4, heat transfer in suspension flow in microchannels is investigated.

Large domain computation results are presented here. The effect of particle suspensions on thermal enhancement is investigated. Chapter 5 includes study of heat transfer in fiber suspension during hot pressing in paper making process. Comparisons with experimental results and thermal properties of different wood types are investigated. In Chapter 6, numerical simulations are used to predict particle micro structure during squeeze flow of particulate thermal interface materials. The results are used to predict thermal properties of these materials. The general conclusions, unique contributions and recommended future work are covered in Chapter 7.

CHAPTER 2

THERMAL LATTICE BOLTZMANN METHODS

In this chapter, the lattice Boltzmann method is described. The thermal lattice Boltzmann methods and recent improvements in the original methods are discussed. The present method for modeling heat transfer in suspension flows is outlined.

2.1 Lattice Boltzmann Method

The Lattice Boltzmann Method (LBM) is obtained by discretizing the Boltzmann transport equation (BTE):

$$\frac{Df}{Dt} = \left(\frac{\partial f}{\partial t} \right)_{collision} \quad (2.1)$$

The Boltzmann transport equation is based on advanced kinetic theory. The distribution function, $f_{\alpha i}(x, t)$ is defined as the possibility of finding fluid particles at a given location and time. The collision term describes the rate of change in fluid particle distribution due to interaction between fluid particles at each location and at each time step. The discrete Boltzmann equation obtained with the BGK (Bhatnagar-Gross-Krook) approximation for the collision term. It is given as [21]:

$$f_{\alpha i}(x + e_{\alpha i}, t + 1) - f_{\alpha i}(x, t) = -\frac{1}{\tau} \left[f_{\alpha i}(x, t) - f_{\alpha i}^{eq}(x, t) \right] \quad (2.2)$$

Where $f_{\sigma i}^{eq}(x, t)$ is the equilibrium distribution function at x and t , and τ is the relaxation time which controls the rate of approach to the equilibrium. The discrete Boltzmann equation is used to update the distribution function, $f_{\sigma i}(x, t)$ at each time step. In this formulation $dt=1$.

It has been shown that the lattice Boltzmann equation with an appropriate equilibrium distribution function reduces to the full Navier-Stokes equations [22-24]. In Lattice Boltzmann method, the physical domain is discretized as a lattice and the flow field is described defining the distribution function in each lattice node. The distribution function is the population of fluid particles at location $\mathbf{x}=(x_1, x_2, x_3)$ and time t that move in the discrete directions σi with discrete velocities $e_{\sigma i}$. In the present study we use D2Q9 (two dimensional nine velocity) model for two dimensional simulations in which the fluid particle may be at rest or move to the nearest lattice point in the horizontal, vertical or diagonal directions [21]. The 2D discrete velocity vectors are defined as:

$$e_{01} = (0,0)$$

$$e_{1i} = \left(\cos \frac{i-1}{2} \pi, \sin \frac{i-1}{2} \pi \right), \quad i = 1, \dots, 4 \quad (2.3)$$

$$e_{2i} = \sqrt{2} \left(\cos \left(\frac{i-1}{2} \pi + \frac{\pi}{4} \right), \sin \left(\frac{i-1}{2} \pi + \frac{\pi}{4} \right) \right), \quad i = 1, \dots, 4$$

In the three dimensional case, the D3Q19 (three dimensional nineteen velocity) model is used in which the fluid particle may be at rest or move to the nearest lattice

point in any of 18 directions denoted by σ_i [25]. The directions are illustrated in Figure 2.1.

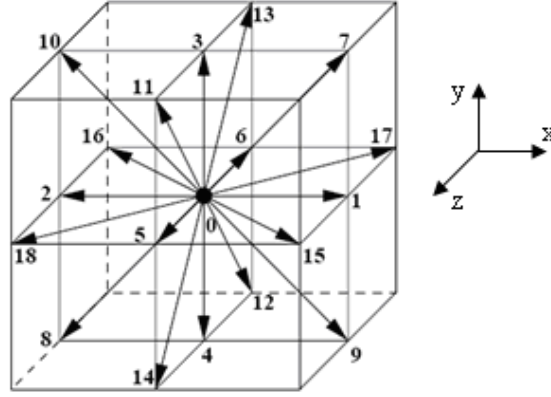


Figure 2.1. Illustration of 18 directions in D3Q19 model

The density, $\rho(x, t)$ and the macroscopic velocity vector, $\mathbf{u}(x, t)$ of the continuum fluid are defined in terms of the fluid distribution function as:

$$\rho(x, t) = \sum_{\sigma, i} f_{\sigma i}(x, t) \quad (2.4)$$

$$\rho(x, t)\mathbf{u}(x, t) = \sum_{\sigma, i} f_{\sigma i}(x, t) \mathbf{e}_{\sigma i} \quad (2.5)$$

The equilibrium distribution function, $f_{\sigma i}^{eq}(x, t)$ is defined as[25]:

$$f_{\sigma i}^{eq}(x, t) = \rho(x, t) [A_{\sigma} + B_{\sigma}(\mathbf{e}_{\sigma i} \cdot \mathbf{u}) + C_{\sigma}(\mathbf{e}_{\sigma i} \cdot \mathbf{u})^2 + D_{\sigma}u^2] \quad (2.6)$$

Considering the conservation laws for mass, momentum and kinetic energy, the coefficients can be determined for (2D and 3D model respectively) as:

$$\begin{aligned}
 A_0 &= \frac{4}{9}, & B_0 &= 0, & C_0 &= 0, & D_0 &= -\frac{2}{3} \\
 A_1 &= \frac{1}{9}, & B_1 &= \frac{1}{3}, & C_1 &= \frac{1}{2}, & D_1 &= -\frac{1}{6} \\
 A_2 &= \frac{1}{36}, & B_2 &= \frac{1}{12}, & C_2 &= \frac{1}{8}, & D_2 &= -\frac{1}{24}
 \end{aligned} \tag{2.7}$$

and,

$$\begin{aligned}
 A_0 &= \frac{1}{4}, & B_0 &= 0, & C_0 &= 0, & D_0 &= 0 \\
 A_1 &= \frac{1}{12}, & B_1 &= \frac{1}{6}, & C_1 &= \frac{1}{4}, & D_1 &= -\frac{1}{4} \\
 A_2 &= \frac{1}{48}, & B_2 &= \frac{1}{12}, & C_2 &= \frac{1}{8}, & D_2 &= 0
 \end{aligned} \tag{2.8}$$

The relaxation time is related to the kinematic viscosity by [21]:

$$\nu = \frac{2\tau - 1}{6} \tag{2.9}$$

2.2 Thermal Lattice Boltzmann Methods

Increasing interest in Lattice Boltzmann simulations has encouraged the efforts to develop a Thermal LBM based on the well developed LB models. Previously, mostly two types of Thermal LBM (TLBM) were used: Multispeed approach and Passive scalar approach.

2.2.1 Multispeed Approach

The multispeed approach can be considered as an extension of the isothermal LB equations. In this method higher order velocity terms are included in the equilibrium distribution function in order to obtain the temperature distribution [26-30]. Alexander et al. introduced a model for flows of monatomic gases that uses a linear and single time relaxation operator [26, 31]. In this approach, the internal energy per unit mass ε is defined through the second-order moment of the distribution function,

$\rho\varepsilon = \sum_{\sigma,i} f_{\sigma,i} (e_{\sigma,i} - \vec{u})^2 / 2$. The equilibrium distribution function includes third-order velocity dependent terms:

$$f_{\sigma}^{eq} = A_{\sigma} + B_{\sigma}(e_{\sigma i} \cdot \vec{u}) + C_{\sigma}(e_{\sigma i} \cdot \vec{u})^2 + D_{\sigma}(\vec{u} \cdot \vec{u}) + E_{\sigma}(e_{\sigma i} \cdot \vec{u})^3 + F_{\sigma}(e_{\sigma i} \cdot \vec{u})u^2 \quad (2.10)$$

The transport coefficients, including viscosity and heat conductivity derived from the Chapman-Enskog expansion, agreed well with numerical simulation.

This approach uses a single distribution function and is straight forward. However, this approach has some disadvantages. Deriving the parameters in the equilibrium function is not simple. The Prandtl number is usually assumed constant and the temperature range is narrow. In addition this approaches suffer from numerical instability; although some efforts has been done to overcome this limitation [28].

2.2.2 Double Distribution Function or Passive Scalar Approach

In this method an additional distribution function is utilized to describe the evolution of temperature. When the viscous and compressive heat generation is negligible, the temperature is passively advected by the fluid flow. Therefore, using this analogy between heat and mass transfer the macroscopic temperature is considered as a passive scalar and the Multi Component LBE model is utilized. It has been shown that this method has a better numerical stability (the energy conservation is not implemented) and is applicable for problems with different Prandtl numbers (diffusivity is independent of the viscosity) [32-34]. Shan has utilized this approach to simulate two and three dimensional Reyleigh-Benard convection [35]. In this method the distribution of component “a” can be determined utilizing the LBE for each component:

$$f_a(x + e_a, t + 1) - f_a(x, t) = -\frac{1}{\tau_a} \left[f_a(x, t) - f_a^{eq}(x, t) \right] \quad (2.11)$$

Here, component 1 represents the motion of the fluid and component 2 represents the passive temperature field. The density and velocity are calculated based on the distribution function for component 1. In the incompressible flow, the temperature field can be simulated by the density field, f_2 which satisfies the diffusion equation:

$$\frac{\partial f_2}{\partial t} + \nabla \cdot (n_2 \vec{u}) = \nabla \cdot (D \nabla f_2) \quad (2.12)$$

2.2.3 Further Developments of TLBM

The above mentioned methods are based on the primary derivation of the Lattice Boltzmann method utilizing single relaxation time collision method (BGK). In that case, the equilibrium distribution function is selected as a small Mach number expansion containing a few coefficients. These coefficients are determined based on the idea that the macroscopic equations derived utilizing Chapman-Enskog expansion should agree with the Navier-Stokes equations.

In 1997, it was shown that the LBE isothermal models can be directly derived by properly discretizing the continuous Boltzmann equation in temporal, spatial, and velocity spaces [36, 37]. He et al. [38] following the same procedure proposed a thermal LBE model in the incompressible limit. This model introduces an internal energy density distribution function to simulate the temperature field by discretizing the continuous evolution equation for the internal energy distribution. Later in 2006, Shan et al. presented in detail the theoretical framework for representing hydrodynamic systems through a systematic discretization of the Boltzmann kinetic equation using Hermite polynomials [39].

In 2004, Shi et al. utilizing the same procedure as He et al. proposed a method for thermal LB simulations in the incompressible limit with only considering viscous heat dissipation and neglecting pressure work [40]. The proposed method is claimed to be more robust and less complex compared to the model presented by He et al. which is rather complicated even in the case when the compression work and the viscous heat dissipation are negligible.

Later, Guo et al. proposed a similar model that includes both viscous heat dissipation and compression work [41]. They considered the evolution of the total energy, h , (instead of the internal energy) as the second distribution function. The evolution of h is obtained from the Boltzmann equation.

In 2007, Gonnella et al. presented a model for non-ideal (van der Waals) fluid [42]. In this model an extra term, I is added to the right hand side of LBE. The extra term I , accounts for the inter particle forces and allows to recover the mass, momentum and energy equations of a van der Waals fluid. In 2008, Nie et al. derived a thermal LBM for gas flows with internal degrees of freedom [43]. This method is useful specially for simulating polyatomic gas flows or for flows with non constant specific heat ratio. Tang et al. described the appropriate thermal boundary conditions for thermal LBE [44].

Several LB models have been developed to simulate multiphase flows under isothermal conditions [45-47]. But, the new TLBMs have led to recent models that can simulate multiphase flows considering the effects of temperature [48-50]. Palmer et al. [50] have proposed a thermal LB model to incorporate temperature effects into LB simulation of two phase flows. The proposed method is a combination of a double distribution function scheme and the work presented by Swift et al. (Ref. [46]) for isothermal two phase flow. The algorithm has been tested for several simple cases such as evaporation of a thin liquid film or an isolated droplet, and condensation of a liquid in a channel. This method can be used for arbitrary values of Prandtl number and non-ideal gases having arbitrary equation of state. Jiaung et al. [51] presented a thermal LBM for the simulation of the phase change problem governed by the heat conduction equation

incorporated with enthalpy formation. Huber et al. [52] utilized the above mentioned method to simulate melting with natural convection.

2.3 Thermal Lattice Boltzmann Model to Simulate Heat Transfer in Suspension Flows

The fluid flow and heat transfer due to a moving body can be simulated by the Navier-Stokes (NS) and Energy (E) equations. The traditional NS & E solvers consider a moving boundary problem and require re-meshing every few time steps. The numerical model used in the current study is based on the solution of the discrete Boltzmann equation over a lattice space for the fluid phase. The lattice Boltzmann method is used, coupled with the Newtonian dynamics and the energy equation to investigate the effect of solid particles on the fluid flow and heat transfer in a complex fluid. This is a robust and efficient computational method for the analysis of solid particles suspended in fluid [25]. An advantage of the lattice Boltzmann method is that the code can be easily implemented on parallel processors because of the local nature of the time evolution operator. Another advantage of this method is that the computational time is independent of the Reynolds number, and only weakly dependent on the number of solid particles, although it is dependent on the size of the computational domain.

Here, the Thermal Lattice-Boltzmann method is based on coupling the LBM with the energy equation [53, 54]. The velocity field and the particle distribution are obtained from the LB calculations and then the temperature field is obtained by solving the energy equation:

$$\rho c_p \left(\frac{\partial T}{\partial t} + \vec{u} \cdot \nabla T \right) = k \nabla^2 T \quad (2.13)$$

using a hybrid differencing scheme for the convective term[55]. This scheme is a combination of central and upwind differencing schemes. The hybrid scheme accounts for flow direction based on local Peclet number which is defined as the ratio of convective to diffusive terms. The central differencing scheme is accurate to second order and is applied to small Peclet numbers ($Pe < 2$). At $Pe \geq 2$, the upwind scheme is applied. The upwind scheme which accounts for transportiveness is accurate to first order.

The dimensionless temperature is defined as:

$$\theta = \frac{T - T_{in}}{T_w - T_{in}} \quad (2.14)$$

Using the lattice units for time, location and velocity, the dimensionless energy equation and the thermal boundary conditions can be written as:

$$\frac{\partial \theta}{\partial t} + \vec{u} \cdot \nabla \theta = \frac{1}{Re \cdot Pr} \nabla^2 \theta \quad (2.15)$$

The results presented here for simulating the movement of suspended solid particles are based on the ALD' method [56]. In this method which combines the Newtonian dynamics of the solid particles with a LB model of the fluid, the movement of the solid particles can be simulated. Furthermore, the interaction between the particles is calculated using the near contact lubrication forces. The LBM presented here is for non-colloidal limit where the effect of Brownian motion is negligible. The motion of each solid particle is found by solving Newton's equations of motion:

$$M \frac{d\vec{U}(t)}{dt} = \vec{F}(t)$$

(2.16)

$$I \frac{d\vec{\Omega}(t)}{dt} + \vec{\Omega}(t) \times [I \cdot \vec{\Omega}(t)] = \vec{T}(t)$$

Where, M, I, U and Ω are particle mass, inertia, linear and angular velocity. T and F are total torque and force on the particle.

The no slip boundary conditions are applied at the solid surfaces. The Knudsen number for liquid flow in microchannels is $\ll 0.01$, so the no slip boundary condition applies. In the present study, the no-slip condition is applied using the bounce-back method. In this method, it is assumed that fluid distributions propagating to the wall boundary are directly bounced back to the fluid domain (Figure 2.2). The effect of Galilean Invariance (GI) error in standard bounce-back method in the lattice-Boltzmann simulations are discussed by Clausen and Aidun, [57], for rigid and deformable particles [58]. The LB operators should be modified at the boundaries to incorporate the boundary conditions. Here, the bounce-back boundary condition is used to calculate the momentum transfer between the fluid and the solid surface. The boundary is always assumed to be located at the middle of the boundary links [25]. When the boundary is at the midpoint of these links, the bounce-back formulation is accurate to second order. The accuracy is first order for more complex boundaries [59].

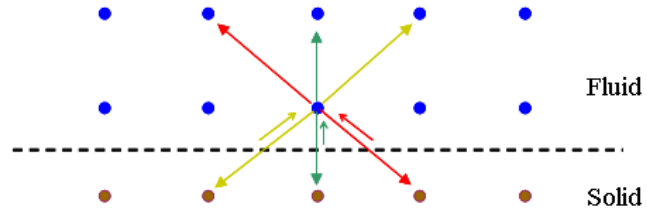


Figure 2.2. Bounce-back boundary condition

The bounce-back boundary condition at stationary solid walls is applied with an appropriate adjustment in distribution function at boundary links:

$$f_{\sigma i}(x, t + 1) = f_{\sigma' i'}(x, t_+) \quad (2.17)$$

Where, $\sigma' i'$ is in the direction opposite to the boundary link σi . At a moving solid boundary with velocity \mathbf{u}_b , the momentum correction is:

$$f_{\sigma i}(x, t + 1) = f_{\sigma' i'}(x, t_+) + 2\rho B_{\sigma} \bar{u}_b \cdot e_{\sigma i} \quad (2.18)$$

CHAPTER 3

MODELING HEAT TRANSFER IN SUSPENSION FLOWS USING LATTICE BOLTZMANN METHOD COUPLED WITH ENERGY EQUATION

In this chapter, sample problems are considered to validate the numerical method and the choice of grid size. The common parameters which will be use in future chapters are also defined here. In section 3.2, the method used for parallel computations is described and the infrastructure used in the large domain simulations is introduced.

3.1 Sample Problem and Validation

In this section sample problems are considered for method validation. To find the appropriate grid size, the effect of a stationary solid particle on heat transfer in channel flow is considered. The numerical results are then validated by comparison with prior results available in the literature for heat transfer from a hot particle in cross flow in a channel. A schematic of the domain and the relevant parameters is shown in Figure 4.1.

The Reynolds number is defined based on the channel height and the mean inlet velocity, u_m .

$$\text{Re} = \frac{u_m H}{\nu} \quad (3.1)$$

Where the mean velocity is given by:

$$u_m = \frac{1}{H} \int_0^H u dy \quad (3.2)$$

In order to compare the thermal performance, the local Nusselt number is defined as:

$$Nu_x = \frac{2H}{\theta_w - \theta_{mx}} \left(- \frac{\partial \theta}{\partial y} \Big|_{y=0,H} \right) \quad (3.3)$$

Where θ_w is the non-dimensional temperature at the wall and θ_{mx} is the non-dimensional form of the mean fluid temperature at location x , defined as:

$$T_{mx} = \frac{1}{u_m H} \int_0^H u T dy \quad (3.4)$$

The average Nusselt number between two locations x_1 and x_2 is defined as:

$$\overline{Nu} = \frac{1}{x_2 - x_1} \int_{x_1}^{x_2} Nu_x dx \quad (3.5)$$

Where x_1 can be selected anywhere in the channel. In the results presented in Chapter 4 the average Nu has been computed between $x_1=25$ and x_2 located at the end of the channel. Eccentricity is defined as a measure of the distance between the vertical position of the particle with respect to the centerline of the channel, given by

$$e = \frac{|2y_0 - H|}{H} \quad (3.6)$$

Blockage ratio, b , is defined as a measure of the size of particle

$$b = \frac{d}{H} \quad (3.7)$$

The appropriate grid size for a grid-independent solution is determined for this sample problem. Three mesh sizes of 256 x 64, 128 x 32 and 64 x 16 corresponding to 16065, 3937 and 945 lattice units are considered. Figure 3.1 compares the effect of lattice units on the horizontal and vertical velocity and the temperature distribution along a line parallel to the y axis and through the center of the solid particle. The difference between the results for grid sizes of 256 x 64 and 128 x 32 is less than 5 percent in the worse case. Therefore, the lattice size of 256 x 64 is selected for two dimensional computations. The selected grid size for particle diameter is 20. This value will be used as minimum particle size in future simulations.

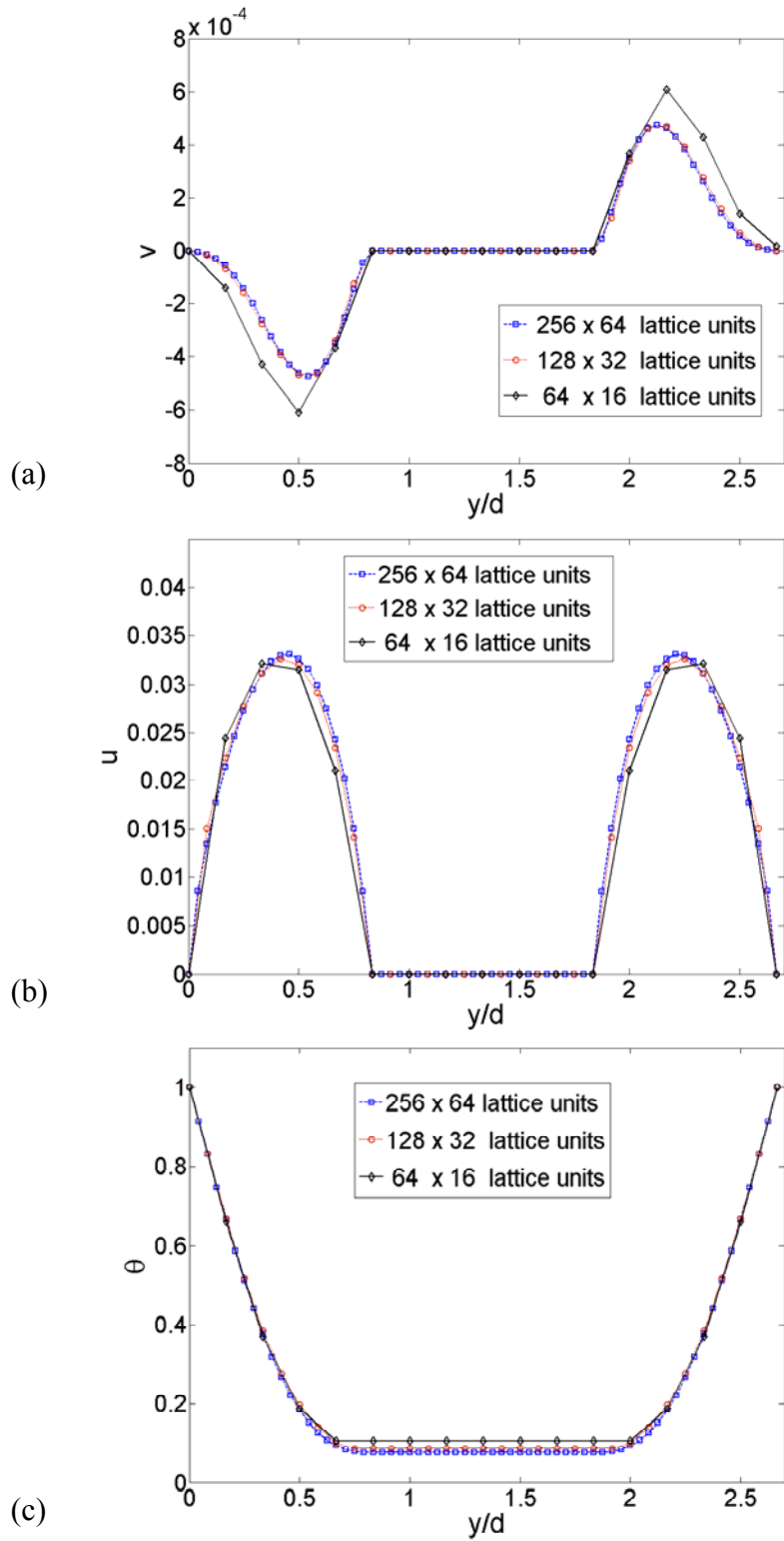
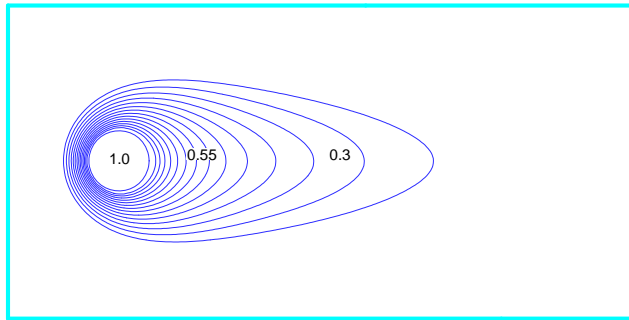
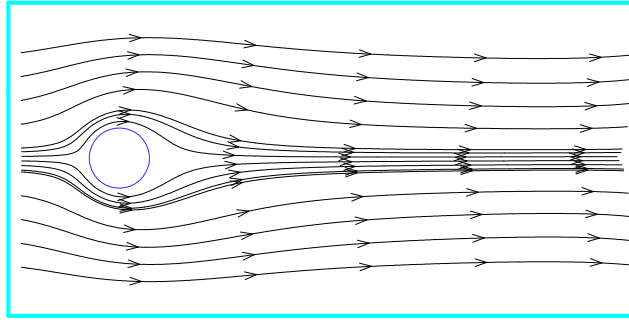


Figure 3.1. Comparing a) horizontal and b) vertical velocity and c) temperature profile for different lattice units

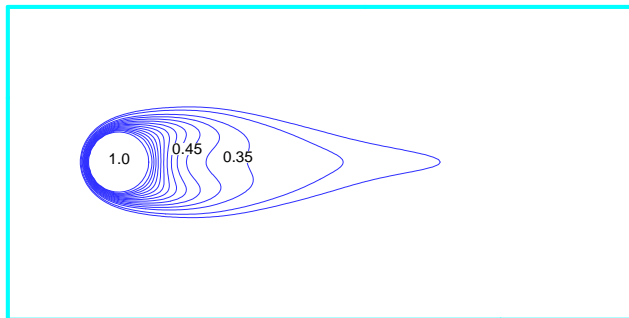
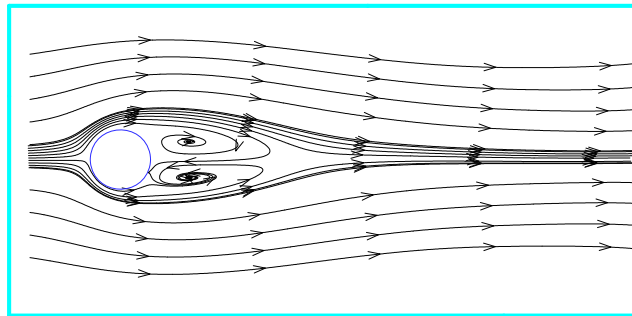
Next, to investigate the accuracy of the computational method, heat transfer from a circular cylinder confined in a channel is considered. In this problem heat is removed from a two dimensional cylinder with constant surface temperature confined in a channel. The flow is from left to right. Here, Re is calculated based on the cylinder diameter and the channel flow rate over the cylinder. Where, the average velocity is defined as:

$$u_c = \frac{1}{d} \int_{y_0-d/2}^{y_0+d/2} u(0, y) dy \quad (3.8)$$

Figure 3.2 shows the streamlines and isotherms for a flow with $Pr=0.74$ and $Re = 5$ and 50 . For $Re=5$, the streamlines and isotherms are attached and symmetric. At $Re=50$, a pair of symmetric and counter-rotating vortices appear. Figure 3.3 shows the snapshots of the streamlines and isotherms at $Re=110$ where periodic vortex shedding occurs in the cylinder wake. The snapshots are at four equally spaced time intervals through the periodic vortex shedding cycle.



(a)



(b)

Figure 3.2. Streamlines and isotherms around a hot particle at a) $Re=5$, and b)

$Re=50$

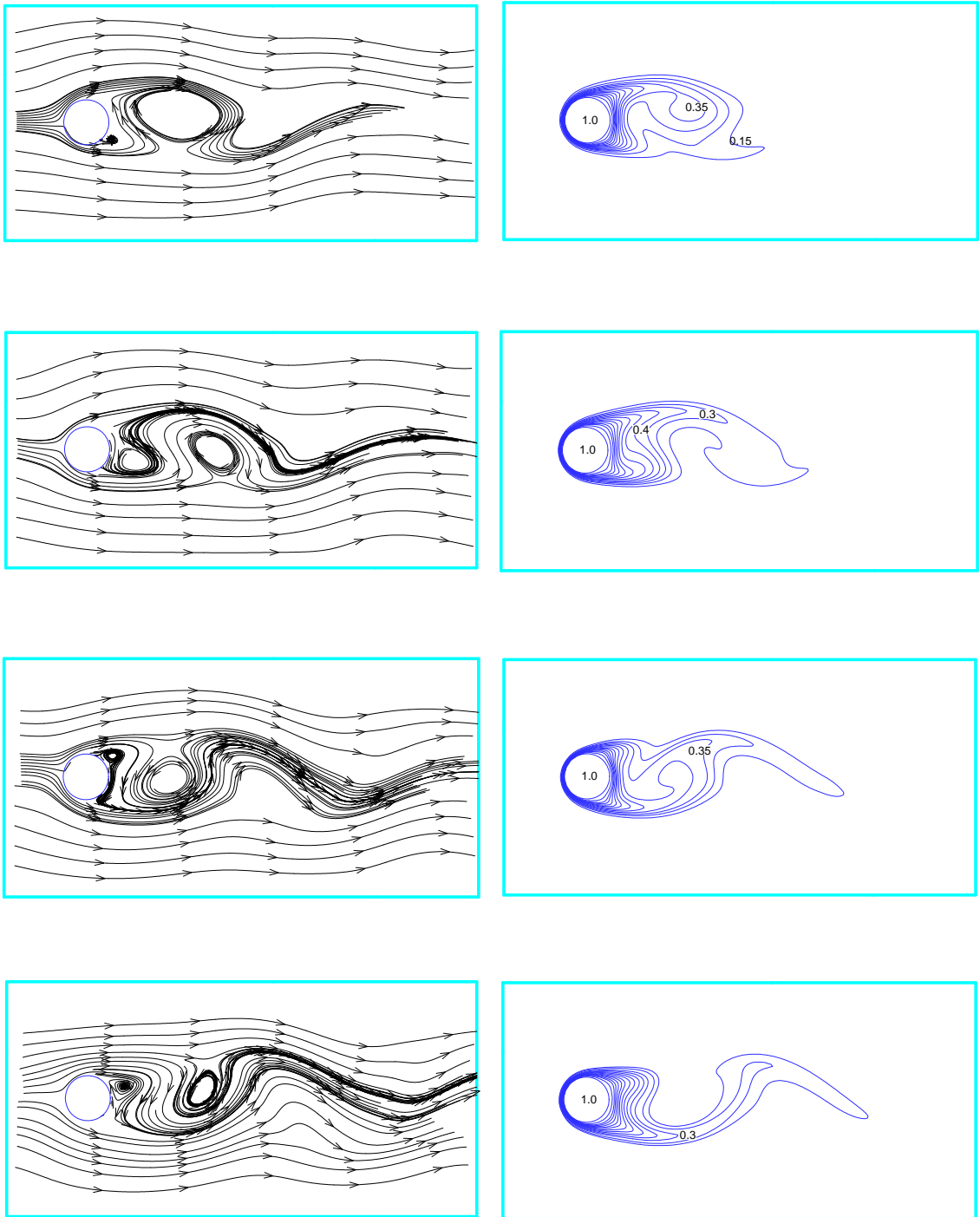


Figure 3.3. Snapshots of streamlines and isotherms around a hot particle at $Re=110$

The variation of average cylinder Nu with Re from the present computations is compared to the experimental results of Hilpert [60], numerical results of Mettu et al. [61], and the analytical results of Khan et al. [62] for $b=0.2$ in Figure 3.4. The current results are in close agreement with the previous experimental and computational results.

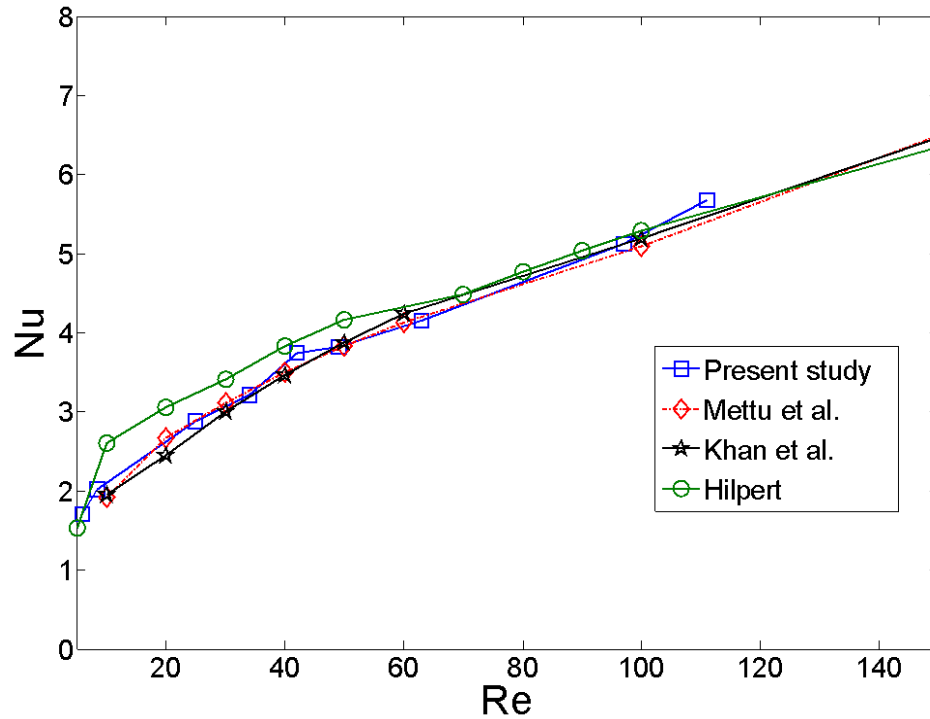


Figure 3.4. Variation of average Nu with Re

3.2 Parallel Computation Implementation

There are two main computing hardware architectures in which each CPU has its own control and computation unit. In shared memory architecture, all of the computing units use a common memory which is shared between them. The processors and memory

are interconnected by some type of network. Figure 3.5 Presents a schematic of shared memory architecture.

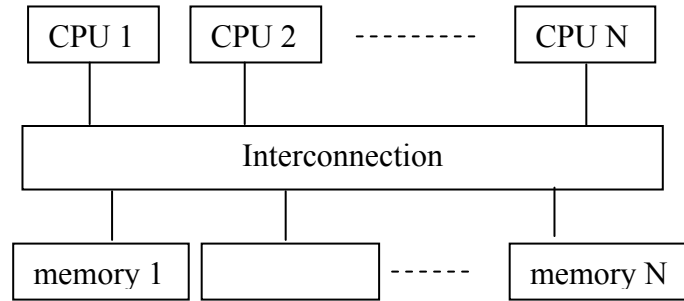


Figure 3.5. Schematic of shared memory architecture

In distributed memory architecture each processor has its own private memory. A schematic of this architecture is shown in Figure 3.6.

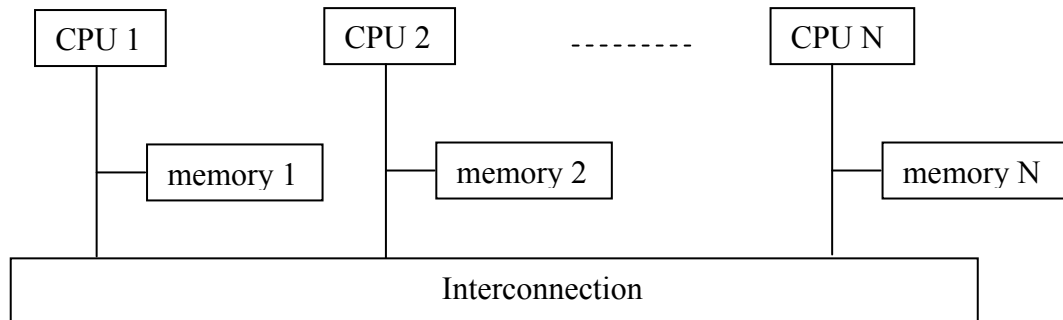


Figure 3.6. Schematic of distributed memory architecture

Two methods for parallel computations are used in the current study: OpenMp and MPI. OpenMP is a standard directives based data parallel model which is used on shared memory architectures. MPI (Message Passing Interface) is the standard application programming interface for message passing model.

3.2.1 Programming Style and Code Performance

The thermal LB code is written in C programming language. Both OpenMP and MPI methods have been used in parallel computations. In MPI implementation, the Cartesian topology is used to discretize the computational domain. The MPI standard Cartesian topology functions (e.g. `MPI_Cart_create`) are utilized. Ghost cells are used in communication of data at boundaries between neighboring sub-domains. The data are communicated between sub-domains in each time step using `MPI_Sendrecv` function. In Figure 3.7 a schematic of the sub-domains and ghost cells is presented.

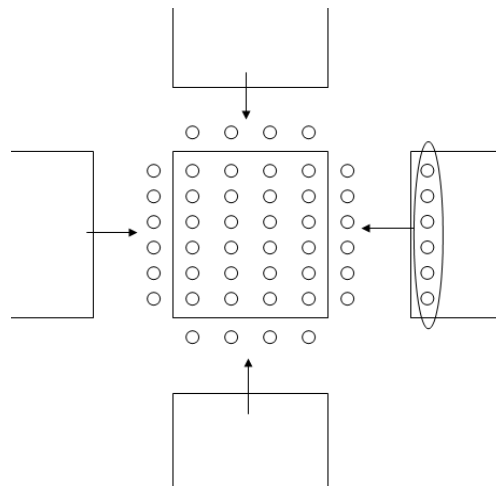


Figure 3.7. Schematic of Cartesian sub-domains and ghost cells

Benchmark studies are performed on Mercury cluster at NCSA and Steele cluster at Purdue University [63, 64]. Mercury (IBM IA-64) cluster consists of 887 IBM cluster nodes. 256 nodes with dual 1.3 GHz Intel Itanium 2 processors Peak performance 5.2 Gflops (Phase 1) and 631 nodes with dual 1.5 GHz Intel Itanium 2 processors Peak performance 6 Gigaflops (Phase 2). The nodes on Phase 1 have 4GB or 12 GB of memory. The nodes on Phase 2 have 4GB of memory.

The Steele cluster consists of 902 dual quad-core Dell 1950 compute nodes. Each node thus has 8 64-bit Intel 2.33 GHz CPUs and either 16 GB or 32 GB of RAM. They are interconnected with either Gigabit Ethernet or InfiniBand. Steele's overall peak performance is 66.59 Teraflops.

In benchmark studies of high performance computing, strong scaling is defined as the ratio of the solution time on one processor to the solution time on N number of processors for a fixed domain size:

$$Speedup = \frac{t_1}{t_N} \quad (3.9)$$

The efficiency is defined as:

$$\eta = \frac{1}{N} \times Speedup \times 100 \quad (3.10)$$

The weak scaling is defined as how the solution time varies with the number of processors for a fixed sub-domain size per processor.

In the benchmark studies, the sample problem is 3D simulation of heat transfer in a forced driven microchannel flow. On Mercury the problem was run for pure fluid and for 10^5 time steps. The domain size is 128^3 cube. Figure 3.8 shows the strong scaling. Figure 3.9 presents the efficiency. It is observed that the efficiency is more than 50 percent until 128 CPUs. The simulation run time is presented in Figure 3.10 and Table 3.1 . The strong scaling study on Steele was done for suspension flow with 5 percent volume fraction. The Strong scaling and efficiency are presented in Figure 3.11 and Figure 3.12. Table 3.2 presents the run time for each LB time step for different number of CPUs on Steele.

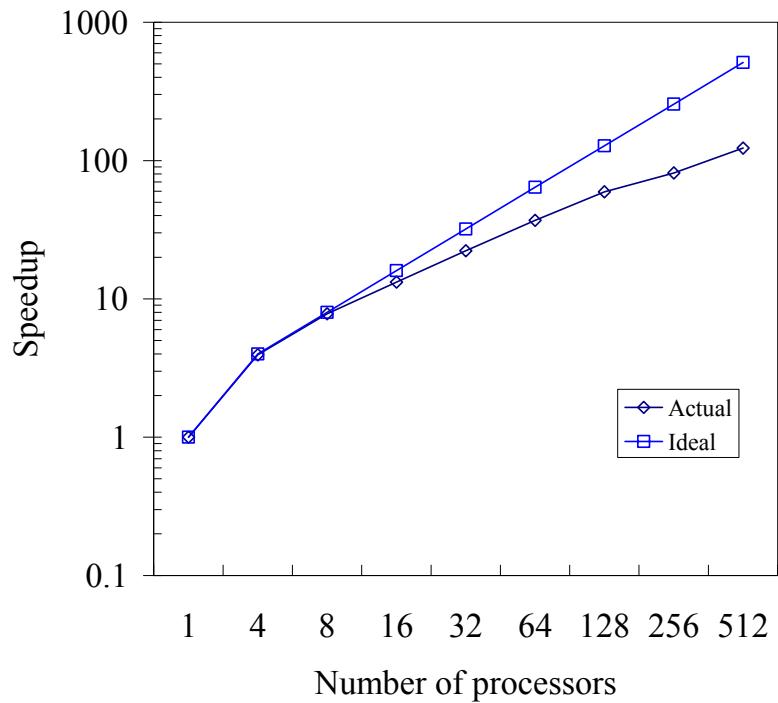


Figure 3.8. Strong scaling on Mercury. The domain size is 128^3 cube.

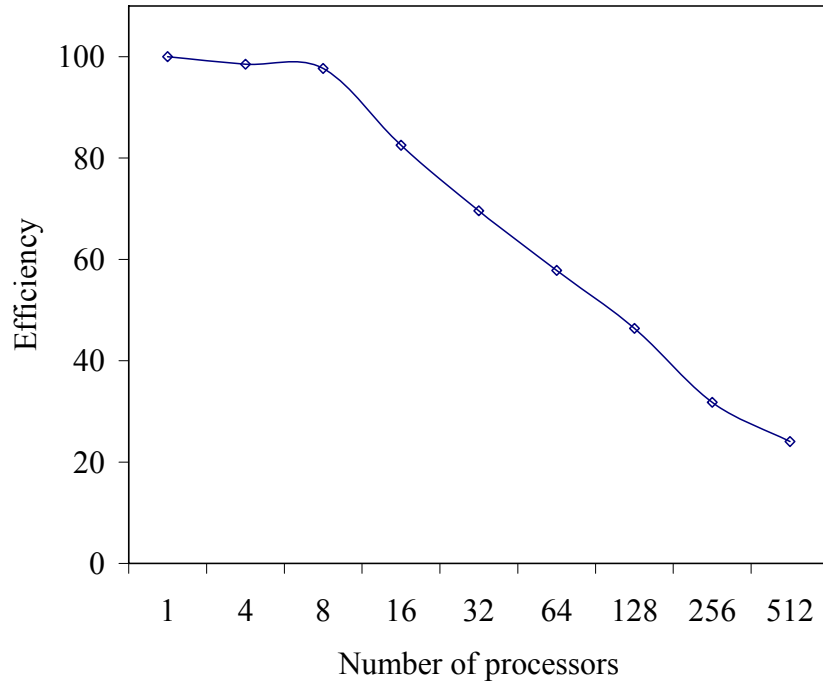


Figure 3.9. Efficiency of strong scaling on Mercury. The domain size is 128^3 cube.

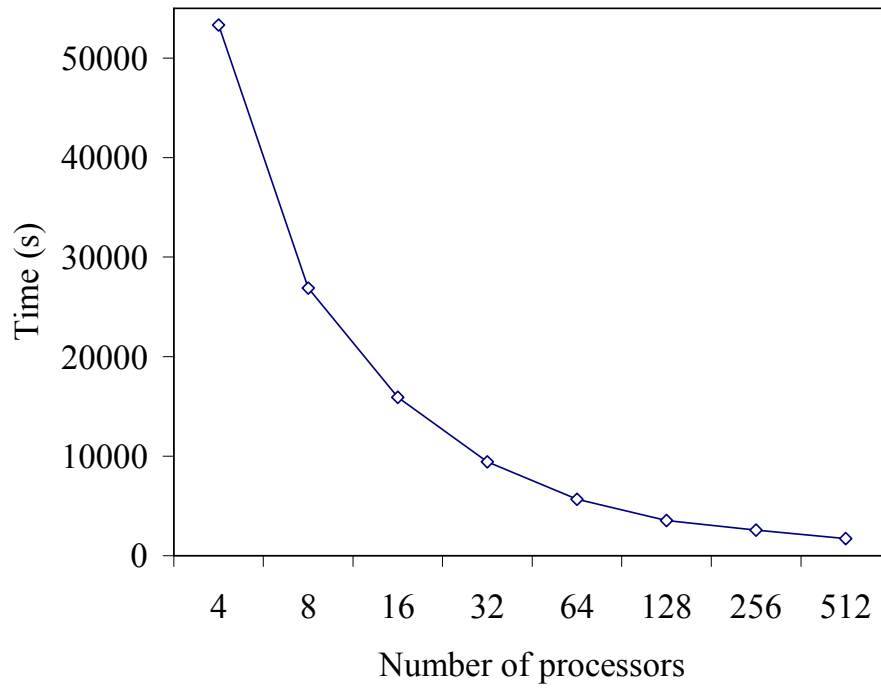


Figure 3.10. Simulation run-time on Mercury. The domain size is 128^3 cube.

Table 3.1. Strong scaling results on Mercury. The domain size is 128^3 cube.

CPU's	Sub-domain size	LB time steps / second
1	$128 \times 128 \times 128$	0.476
4	$64 \times 64 \times 128$	1.875
8	$64 \times 64 \times 64$	3.719
16	$32 \times 64 \times 64$	6.283
32	$32 \times 32 \times 64$	10.598
64	$32 \times 32 \times 32$	17.615
128	$16 \times 32 \times 32$	28.257
256	$16 \times 16 \times 32$	38.745
512	$16 \times 16 \times 16$	58.548

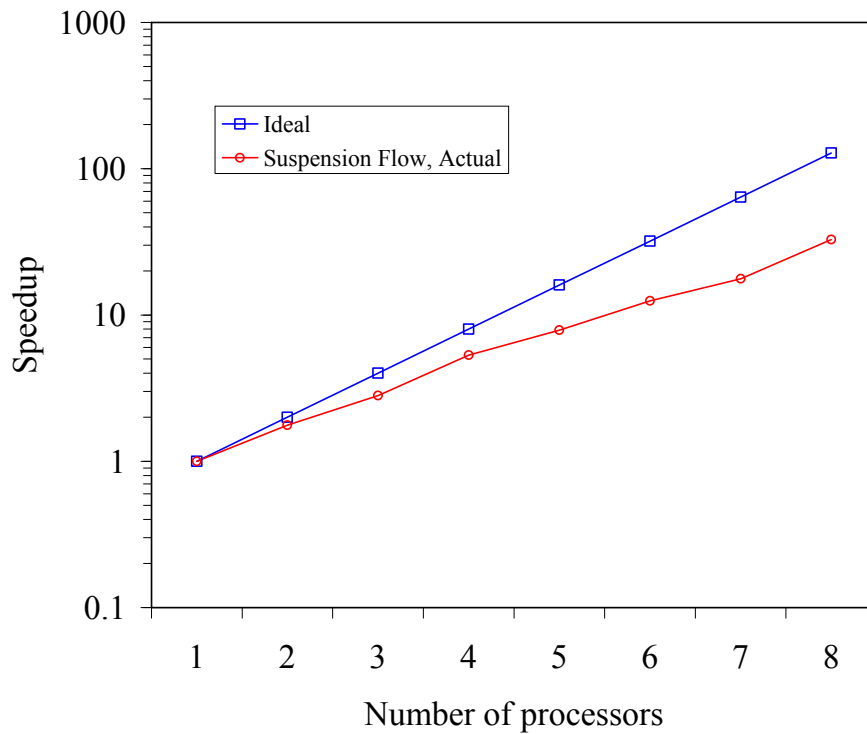


Figure 3.11. Strong scaling on Steele. The domain size is 128^3 cube. ($\phi=5\%$)

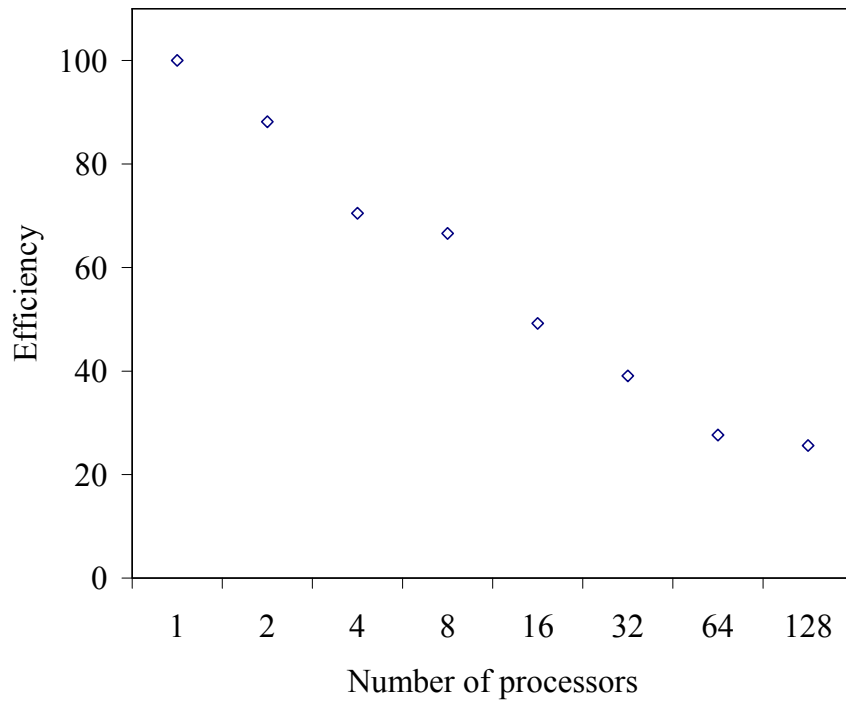


Figure 3.12. Efficiency of strong scaling on Steele. The domain size is 128^3 cube.
 $(\phi=5\%)$

Table 3.2. Strong scaling results on Steele. The domain size is 128^3 cube. $(\phi=5\%)$

CPUs	Sub-domain size	LB time steps / second
1	$128 \times 128 \times 128$	0.424
2	$64 \times 128 \times 128$	0.747
4	$64 \times 64 \times 128$	1.194
8	$64 \times 64 \times 64$	2.256
16	$32 \times 64 \times 64$	3.333
32	$32 \times 32 \times 64$	5.295
64	$32 \times 32 \times 32$	7.494
128	$16 \times 32 \times 32$	13.891

CHAPTER 4

HEAT TRANSFER IN SUSPENSION FLOW IN MICROCHANNELS

In this chapter, convective heat transfer in suspension flow in microchannels is studied numerically. The numerical method described in the previous chapter is utilized. In section 4.1, the motivation and an overview of previous studies is presented. The computational domain and boundary conditions are described in section 4.2. The effects of single or multiple particles on channel flow heat transfer are presented in section 4.3. These simulations provide the details of the phenomena which happen in large domain simulations with large number of particles. Section 4.4 presents the results of large domain simulations.

4.1 Convective Heat Transfer in Suspensions

There are several applications in thermal systems such as heat exchangers, turbine blade cooling, and electronics thermal management in which forced convective heat transfer in microchannels is important. Increasing use of microchannel heat exchangers in high performance thermal systems motivates exploration of techniques to further improve the channel heat transfer rate. The possibility to enhance the rate of heat transfer through interaction between a stationary or moving solid particle and the fluid flow confined within a channel is of significant interest. These interactions cause variations in the flow

field and temperature distribution and consequently change the thermal performance of the system.

Analytical solutions for laminar forced convection heat transfer in ducts are summarized by Shah and London [65]. Furthermore, many numerical and experimental studies consider different channel flow geometries [66-70]. Khan et al. reported an integral approach to study the heat transfer from a cylinder confined between parallel plates [62]. Mettu et al. [61] and Dennis et al. [71] have reported numerical results for heat transfer from an isothermal cylinder in a channel flow. An experimental investigation has been done by Nakagawa et al. for heat transfer in a channel flow around a rectangular cylinder [72]. They have shown that the heat transfer is enhanced compared to a channel with no blockage. Sharma et al. have studied the effect of channel confinement on the natural convection from a rectangular body using a finite volume method [73]. Wu et al. have studied numerically the transient mixed heat convection around three heated cylinders in a horizontal channel and the effect of cylinder spacing on it [74].

Several studies consider the effect of a moving solid particle in a channel. Fu et al. adopted an arbitrary Lagrangian-Eulerian method to simulate the heat transfer induced by an isothermal rectangular body moving in the streamwise direction in an adiabatic channel [75, 76]. The heat transfer around a heated oscillating cylinder is studied experimentally by Gau et al. [77]. Patnaik et al. have done finite element simulations of heat transfer in internal flows employing a velocity correction algorithm, with a Galerkin weighted residual formulation [78]. Most of the previous works outlined above are

focused on heat transfer from the solid particle. The fluid flow and heat transfer due to a moving body is studied in some special conditions by finite element methods. These methods consider a moving boundary problem and require re-meshing in each (/few) time step(s).

4.2 Problem Description

The physical domain with the coordinate system and the relevant parameters are presented in Figure 4.1. Cylindrical or spherical solid particles with diameter d are considered for the cases of (i) fixed, (ii) moving with constant velocity, and (iii) freely suspended inside a microchannel with dimensions $L \times H$. The channel walls (top and bottom surfaces) are considered at constant temperature, T_w . Periodic boundary conditions for the forced flow are used at the inlet and outlet boundaries at $x=0$ and $x=L$, respectively. The inlet temperature, T_{in} , of the fluid is assumed constant and the temperature gradient normal to the outlet boundary ($x=L$) is set to zero. The temperature field and heat flux are assumed to be continuous at the interface of the fiber and water. As mentioned in section 2.3, the LBM presented here is for non-colloidal limit where the effect of Brownian motion is negligible. The effect of Brownian motion can be evaluated using the dimensionless Peclet number [79, 80]:

$$Pe = \frac{6\pi\mu\dot{\gamma}d^3}{k_B T} \quad (4.1)$$

Where, $\dot{\gamma}$ is the shear strain rate, T is temperature, d is particle diameter and $k_B=1.381 \times 10^{-23}$ is the Boltzmann constant. The Pe number is defined as the ratio of the

time required for the Brownian motion to move a particle to the time required for the shear flow to move it a distance equal to its size. At large Pe number regime ($Pe > 100$), the effect of Brownian motion can be neglected [80, 81]. For water suspension flow in a microchannel at room temperature, $T=300\text{K}$ with channel height, $H=50\mu\text{m}$ and particle diameter, $d=200\text{ nm}$, the Pe is equal to 500 and 5000 at $Re=10$ and 100, respectively. Therefore, the present results for suspension flow simulations are valid for particle size larger than 200 nm in diameter. In the following simulations, properties of base fluid and solid particles are selected based on properties of water ($Pr=5.8$, $k=0.613\text{ W/m.K}$ at 300K) and Al_2O_3 ($k=50\text{ W/m.K}$) which are common materials in such applications.

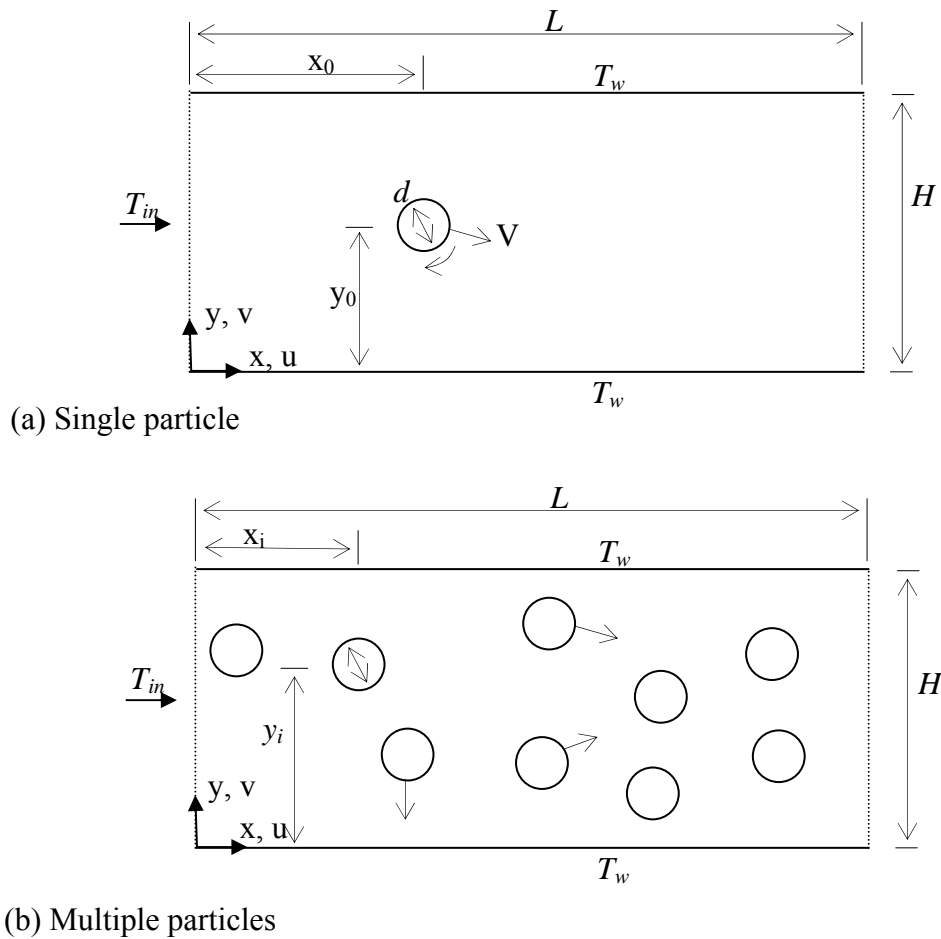


Figure 4.1. Schematic of the physical domain

4.3 Detail Study of Effect of Individual Particles on Heat Transfer from Channel Walls

In this section, the effect of solid cylindrical particles within the channel on the heat transfer from the channel walls is studied. Three cases are considered, (i) stationary, (ii) moving with a constant velocity, and (iii) freely suspended in the flow.

4.3.1 Effect of a single particle

Figure 4.2 and Figure 4.3 show the streamlines and isotherms in a channel with and without a solid particle with different conditions. Comparing Figure 4.2-a and b it is seen that interaction of the fluid with the particle results in deviations in the streamlines. This effect results in a faster fluid motion and larger heat transfer rate near the wall. The constant velocity particle and freely suspended particle cases (Figure 4.3), will be discussed in the following sections.

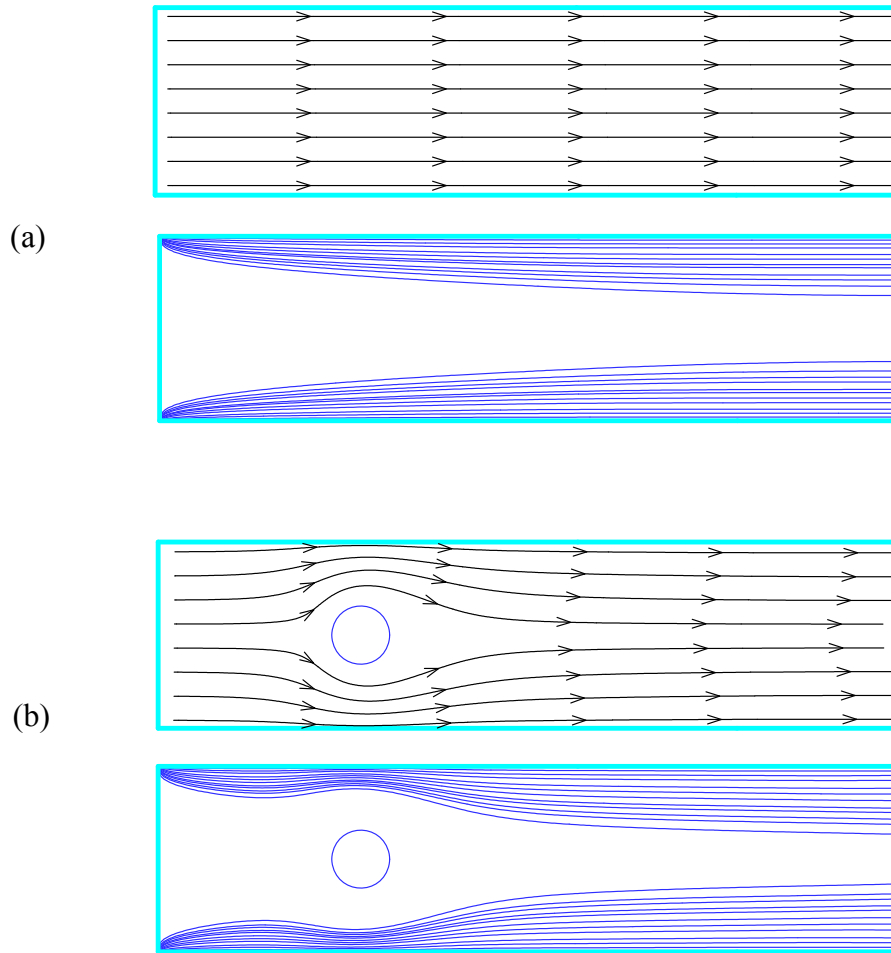


Figure 4.2. Streamlines and isotherms in a) an unblocked channel, and b) a channel containing a stationary particle

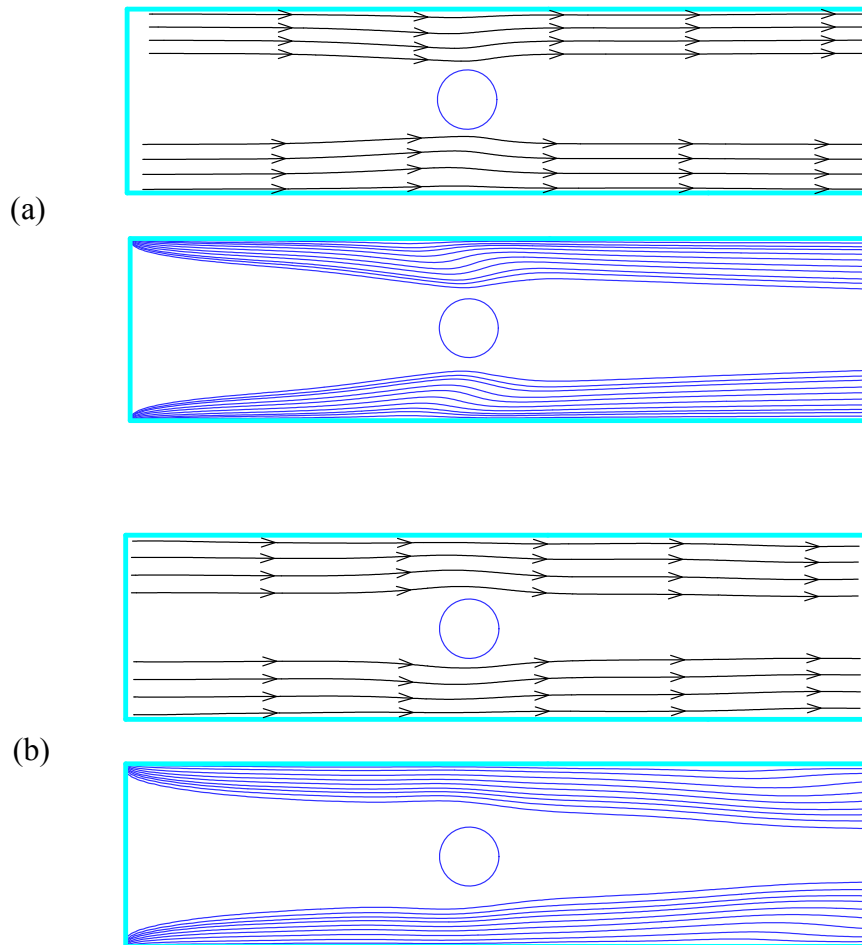


Figure 4.3. Streamlines and isotherms in a channel containing a particle a) moving with constant velocity, and b) freely suspended

Figure 4.4 shows Nu distribution along the channel walls for pure fluid as well as a case with stationary solid particle. Prior analytical [65] and numerical [76] results are also presented in this figure showing good agreement with the current results. It is seen that the wall Nusselt number is larger near the particle with a local peak in Nu due to the higher fluid speed in this region. In this case, the local Nu is 90% higher near the particle

and the average Nu for the channel containing a solid particle is 7.6% higher than the average Nu for an unblocked channel. Results show that heat transfer can be enhanced with solid particles inside the channel suggesting a method to provide cooling in the presence of non-uniform heat dissipation, for example, when there are hot spots in the channel walls that require locally more effective heat transfer. In that case, an obstacle could be placed in the channel behind the hot spot to locally increase the heat transfer rate.

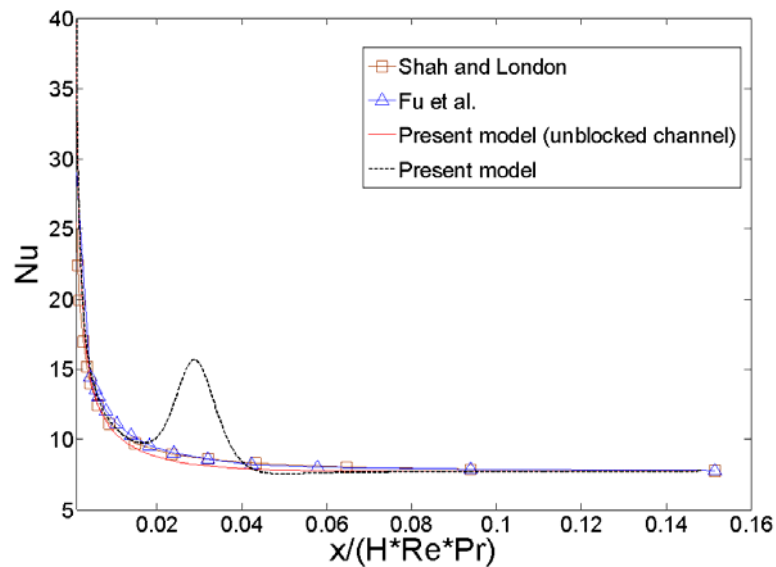


Figure 4.4. Local Nu distribution along the channel wall; b=35%

Figure 4.5 shows Nu distribution along the channel wall containing a solid particle for different Re. It is seen that with increasing Re the local peak in Nu increases. The local Nu at the location of particle for Re=70 and 30 is 67% and 50% higher compared to the local Nu for Re=15, resulting in a relatively higher average Nu.

Therefore, the average Nu for Re=70 and 30 is 55% and 23% respectively higher than the average Nu for Re=15.

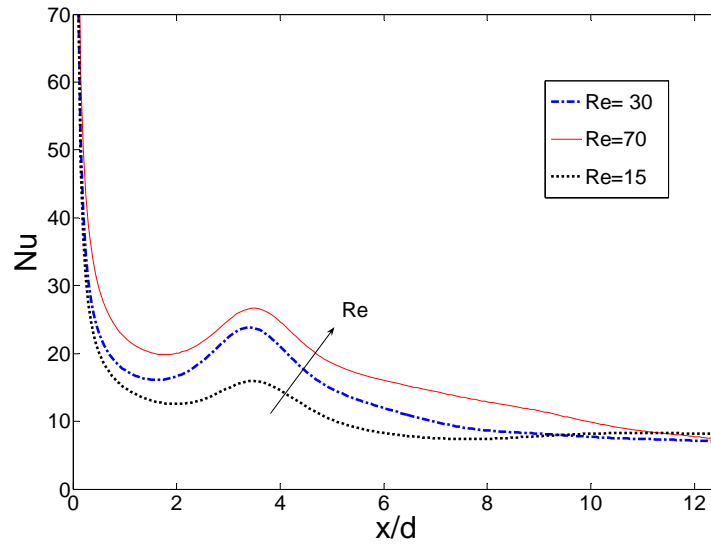


Figure 4.5. Effect of Re on Nu (stationary particle); b=35%

The size of particle can affect the flow field and therefore thermal performance. Figure 4.6 shows the distribution of Nu for particles with different sizes. As the size of the particle increases, the streamlines become denser near the wall above and under the particle, causing a higher fluid velocity in the vicinity of the hot walls and therefore a better heat transfer rate. For b=0.35 and 0.25 the average Nu numbers are 7% and 3% higher than b=0.15 at Re=40.

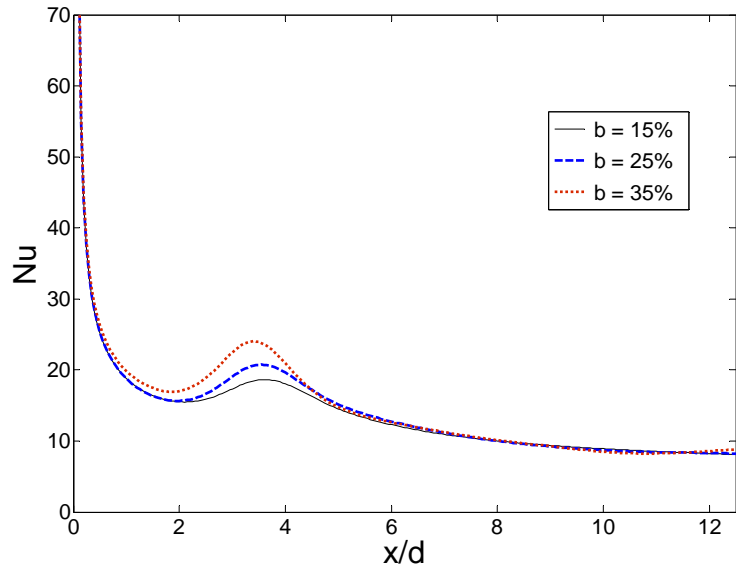


Figure 4.6. Effect of blockage ratio on Nu (stationary particle); Re=40

The effect of vertical position or eccentricity of the solid particle on the Nu variation is shown in Figure 4.7. When the particle is located closer to the lower wall, there is a higher peak in the Nu distribution at the lower wall compared to the upper wall. For example, for 22% eccentricity the local peak in the lower wall is 14% higher than the local peak when the particle is at the center. In this case, the streamlines are denser near the lower wall and the fluid velocity is higher, resulting in a better heat removal and a higher Nu. Therefore, the local peak in Nu increases, as the eccentricity increases. On the other hand, the fluid velocity is slower near the upper wall. Therefore, the local peak at the upper wall is smaller relative to the local peak at the lower wall. It is also smaller than the local peak when the particle is located at the center of the channel. The fluid trends to move toward the center of the channel after the particle. The movement is more effective near the lower wall because of the higher fluid velocity. It causes Nu to decline more at

the lower wall compared to the upper wall. Therefore, the overall heat transfer enhancement is more effective in the upper wall and the average Nu is 8% larger in this case. Thus, moving the particle toward a wall in the channel locally enhances the heat transfer at that wall but the overall heat transfer becomes worse at that wall.

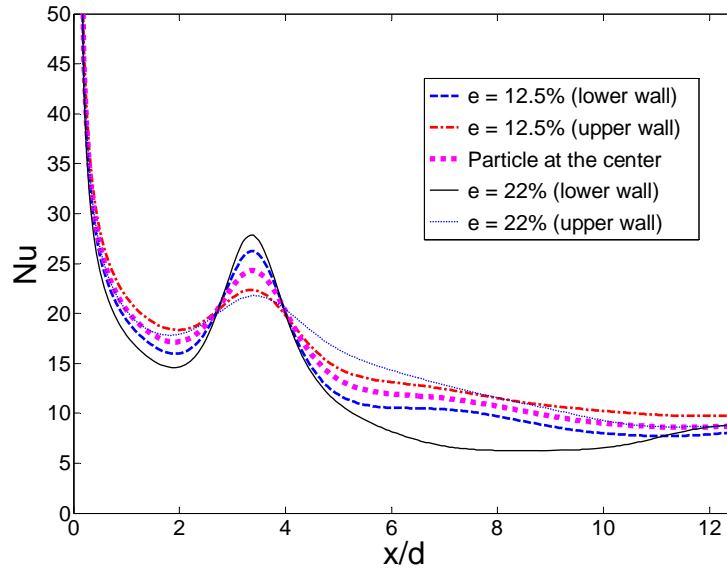


Figure 4.7. Effect of Eccentricity on Nu (stationary particle); $Re=40$ and $b=35\%$

4.3.2 Effects of multiple particles

When there is more than one particle inside the channel, the Nu variation along the channel walls is more complex. Figure 4.8 presents the Nu distribution for a channel containing one, two or three stationary solid particles at different locations at $Re=40$. The disturbance in the flow field is more while there are multiple particles inside the channel. Therefore, the heat transfer is enhanced more, and the average Nu is higher. In fact, each particle can locally increase the heat transfer rate due to flow modification near the wall.

If the particles are close to each other, the upstream particle affects the flow downstream. If the particles are far enough, for example at $x=70$ and 150 , the shape and the magnitude of Nu around the particle may be approximated from the results for a channel containing one particle at that location.

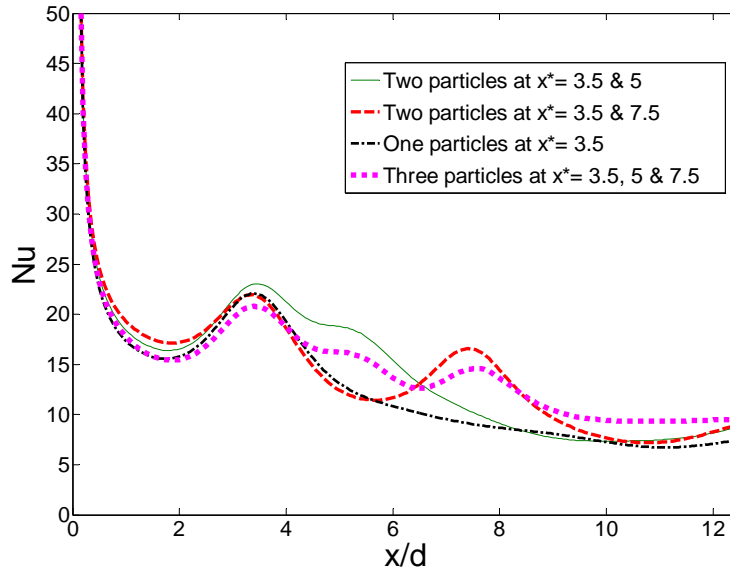


Figure 4.8. Nu distribution (multiple stationary particles); $Re=40$

4.3.3 Effect of a particle moving with a constant velocity

Figure 4.3-a shows the streamline and isotherms for a particle which is moving to the right with a constant velocity equal to 0.03 for $Re=50$. Compared to a stationary particle, when a particle moves with a constant velocity, there is a sudden vacant space behind it which is occupied by the surrounding fluid. It causes the fluid to move toward the center right before the particle. This results in a drop in Nu . The flow then passes the particle and therefore the streamlines become somehow deflected towards the wall. In

front of the particle, there is no obstacle in the flow, so the fluid trends to move toward the center of the channel. The isotherms also behave in a similar manner. Therefore, it is expected that Nu will decrease in front of the particle. Figure 4.9 shows the Nu distribution at different Re. The sudden drop right before the particle is because of the earlier mentioned movement of the adjacent fluid to the vacant space before the particle. At higher Re the mean fluid velocity is higher than the particle velocity; therefore it is observed that as the Re increases the local Nu increases as well.

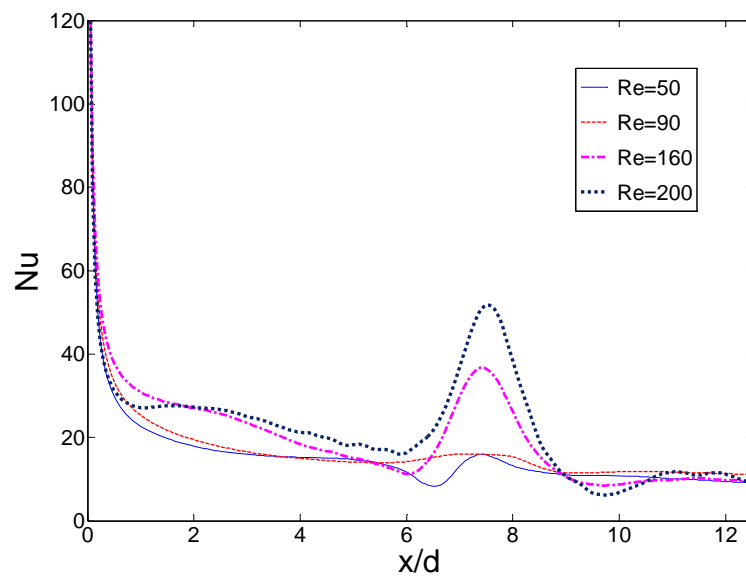


Figure 4.9. Nu distribution for particle moving with const. velocity; $b=35\%$

4.3.4 Effect of freely suspended particles

When a particle is freely suspended in the main flow, the flow conditions are different relative to when a particle moves with constant velocity: For this case, the streamlines and isotherms are shown in Figure 4.3-b for $Re=50$. The streamlines behind

the particle are deflected to the wall. On the other hand, the streamlines smoothly go toward the center of the channel in front of the particle. These effects are also observed in the isotherms, which are denser and smoother behind the particle causing the local Nu to be relatively constant in the region upstream proximity of the particle. Furthermore, a sudden drop of Nu, such as in Figure 4.9, is not observed in this case. The isotherms decline toward the center in front of the particle and finally approach those in a channel containing no particles. Therefore, Nu decreases in front of the particle. Figure 4.10 shows the Nu distribution during the flow as the particle is moving through the channel.

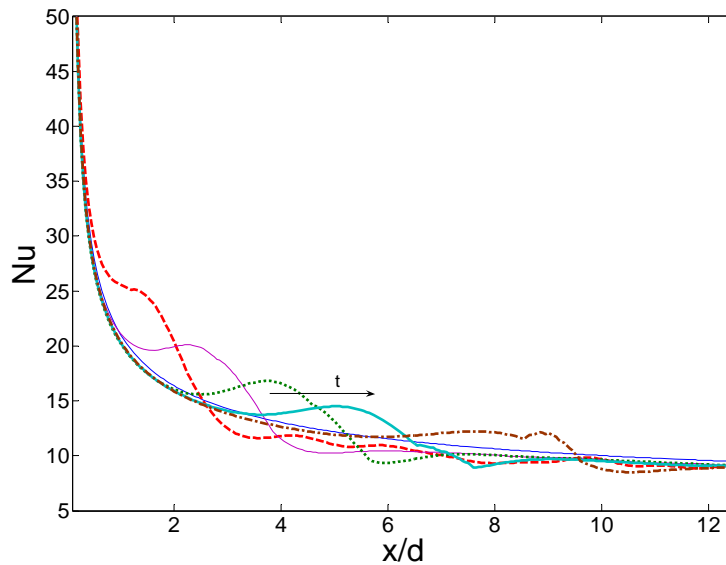


Figure 4.10. Nu distribution at different times (freely suspended particle); $Re=45$
and $b=35\%$

Nu distribution along the channel wall containing a feely suspended solid particle for different Re is shown in Figure 4.11. For the same number of time steps, the

displacement of a particle suspended in a flow with lower Re is smaller. It is seen that with increasing Re the local Nu in the entry region increases. The effect of suspended particle on the Nu distribution is similar for different Re. Nu is nearly constant behind the particle and there is a sudden drop in Nu in front of the particle.

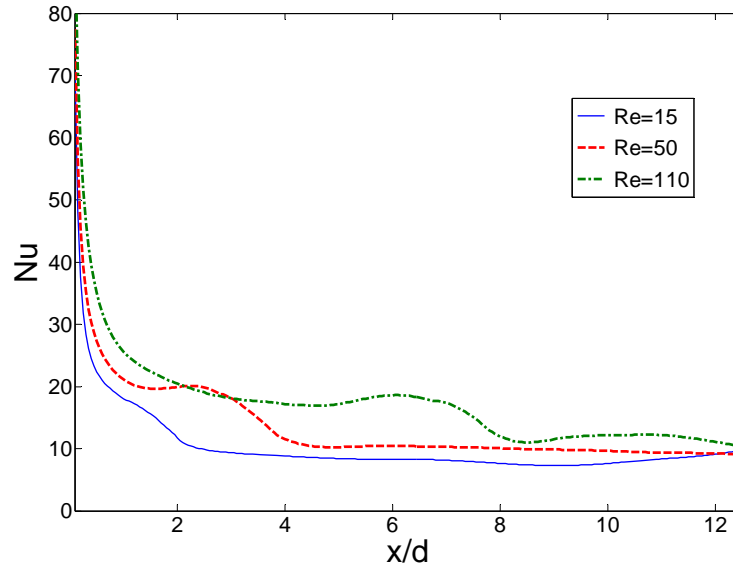


Figure 4.11. Effect of Re on Nu distribution; b=35%

Figure 4.12 shows the distribution of Nu for suspended particles with different sizes. It is seen that the blockage ratio does not have an important effect on the Nu distribution.

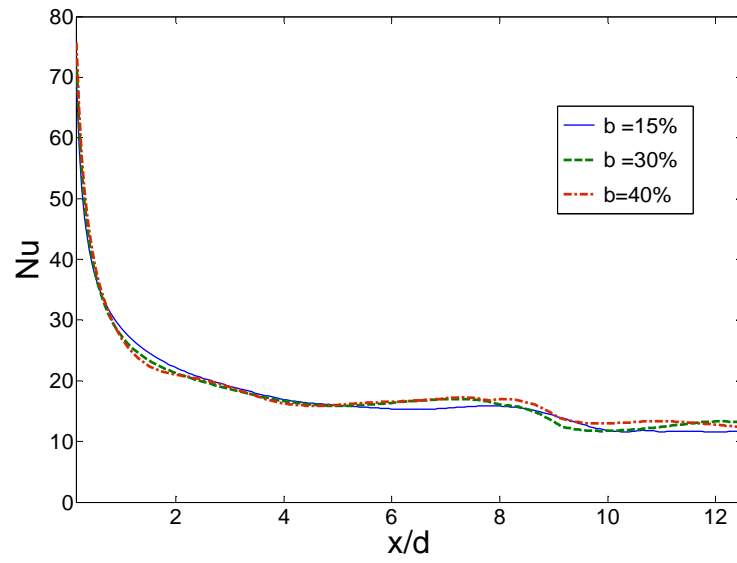


Figure 4.12. Effect of blockage ratio on Nu (suspended particle); Re=110

In real life applications such as in micro/nanofluids there are multiple solid particles freely suspended in the cooling medium (Figure 4.1-b). Figure 4.13 presents the Nu distributions for channel flow in which 48 solid particles are suspended in the fluid. The suspension flow is non-homogeneous, so the Nu distribution in the upper and the lower channel walls are not similar. It is observed that the Nu distribution is similar to that in a channel containing no particles with some local fluctuations. The location and the amount of variation in the Nu depend on many factors such as the position of the particle and the Re. The heat transfer is enhanced when the particles are closer to the wall, or when a particle is located close to another particle. Furthermore, when there is more than one particle inside the channel, the Nu variation along the channel walls is more complex. Therefore, different thermal effects are expected when the particles are in different locations. In a sample where many particles are homogeneously distributed in

the fluid and we expect to observe similar effects on heat transfer. Simulations with larger domains considering are performed in the next section to investigate these effects.

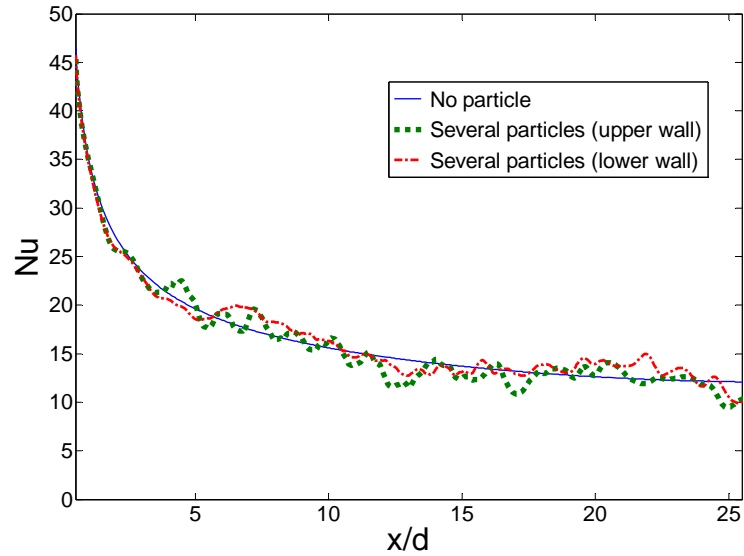


Figure 4.13. Nu distributions for a fluid containing several suspended particles;
 $Re=220$ and $b=6\%$

4.4 Large Domain Simulation Results

In this section, large domain transient three dimensional simulation results are presented. The results of the small scale simulations from section 4.3 are used to describe the current observations. The simulations are performed on Purdue Steele cluster applying MPI method for parallel computing as outlined in the previous chapter. A sample of domain decomposition (128 sub-domains) for a channel flow containing spherical particles is presented in Figure 4.14. The boundary conditions are similar to the conditions described in section 4.2. In the z direction, periodic conditions are applied.

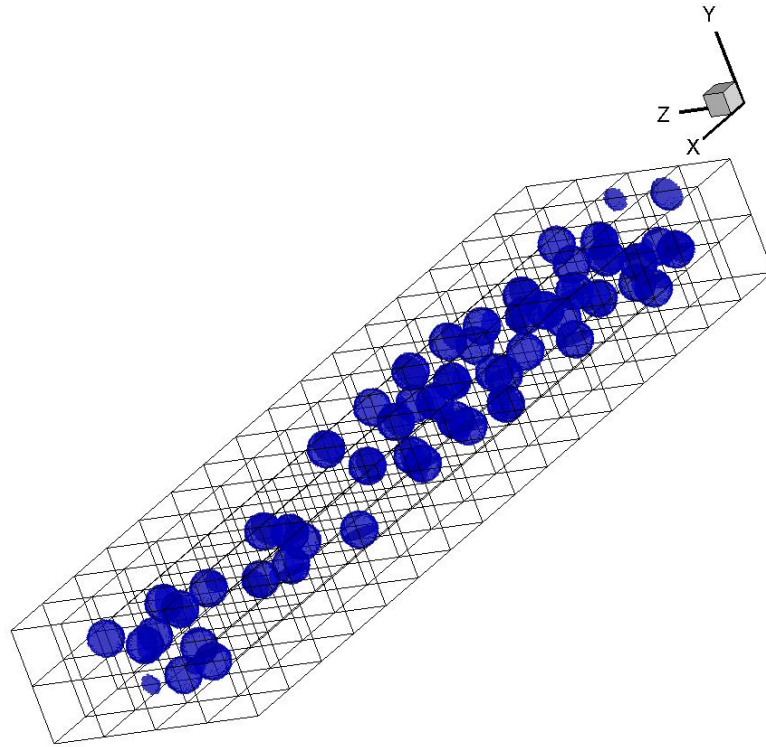


Figure 4.14. Computational domain decomposition

Figure 4.15 presents particle distributions in a sample sub-domain at three different times at 1percent volume fraction. It is observed that the number of particles in each section is random and time dependent. Therefore, different streamline and isotherms are observed at different times. As discussed in the previous section, the effect of particles suspended in flow is to disturb the flow near the walls. This affects the temperature gradient near the channel wall and enhances heat transfer. The temperature field in the sub-domain is presented in Figure 4.16. In Figure 4.16-a, no particle is observed near the wall. In this case, the temperature gradient is not affected by the particles and it is not expected to have enhanced heat transfer in that section. The temperature field in a pure fluid channel

flow is presented in Figure 4.17. Comparing these two figures shows the effect of particle on temperature field disturbance near the wall. Particle distribution and temperature field for 5 percent volume fraction are shown in Figure 4.18 and Figure 4.19. The temperature field in a vertical plane of this sub-domain at similar times and for different volume fractions is presented in Figure 4.20. The transient wall Nusselt number along channel length is presented in Figure 4.21 and Figure 4.22 for zero and five percent volume fractions, respectively. The non-dimensional time is defined based on mean velocity and particle diameter. As outlined in the previous section (4.3.4), the suspended particles cause local disturbance in wall Nu. The disturbance domain is affected by particle size, volume fraction and mean flow Reynolds number.

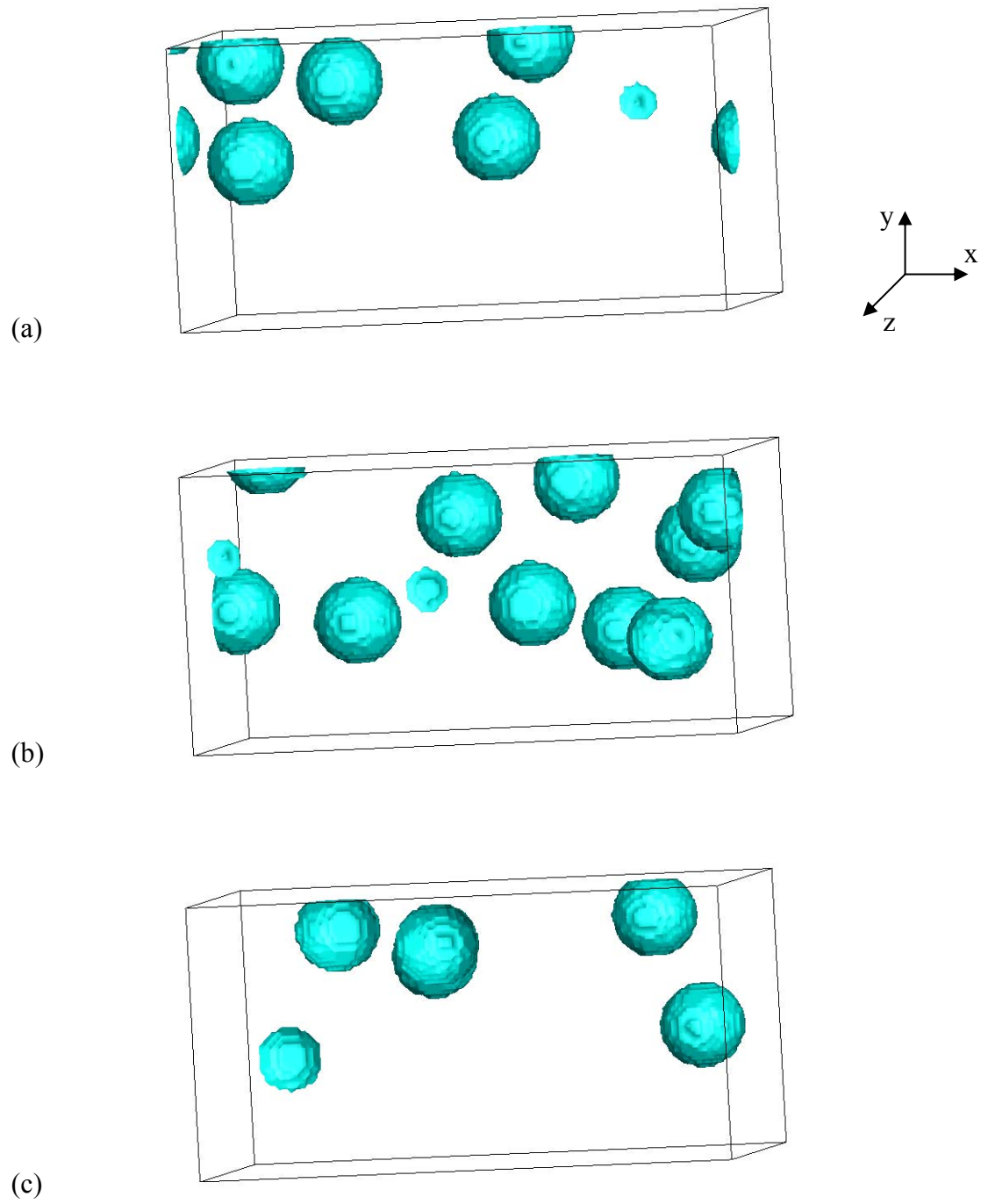


Figure 4.15. Particle distribution in a sample sub-domain at different times

($\phi=1\%$)

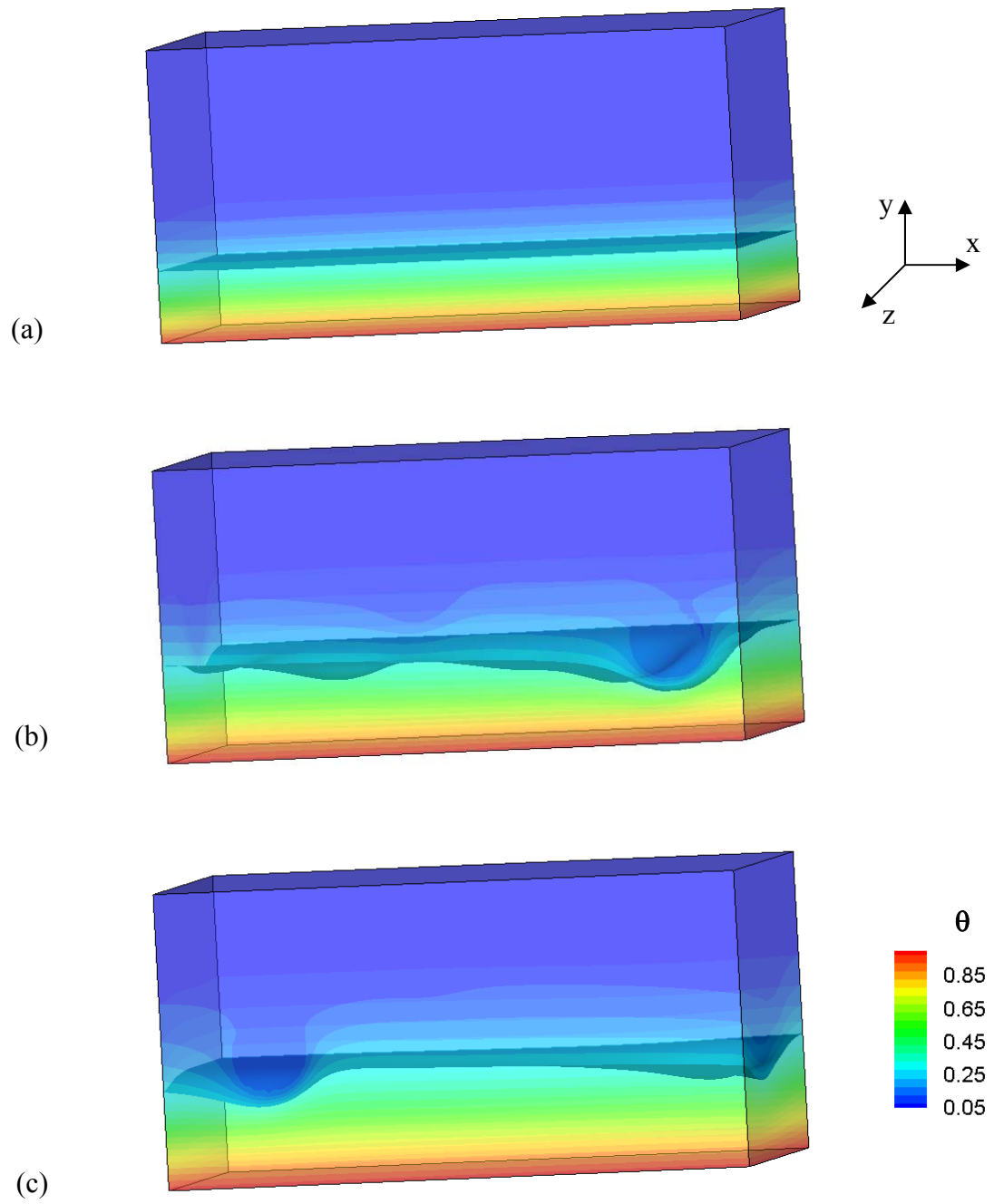


Figure 4.16. The effect of flow disturbance caused by moving particles on the temperature field in a sample sub-domain at different times ($\phi=1\%$)

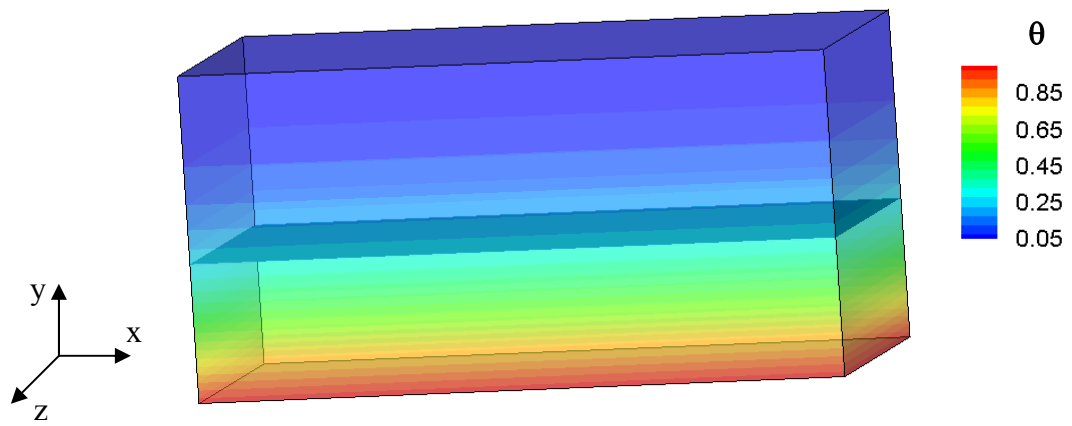


Figure 4.17. Temperature field in a sample sub-domain (no solid particles)

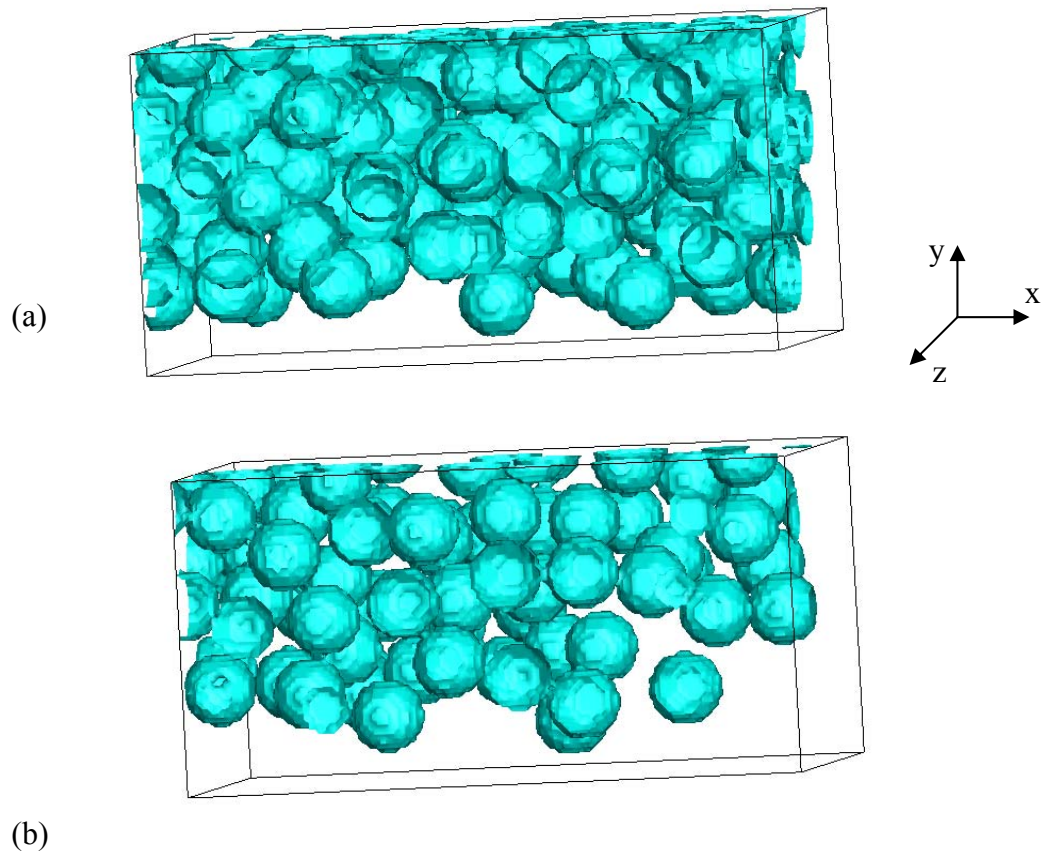


Figure 4.18. Particle distribution in a sample sub-domain at different times

($\phi=5\%$)

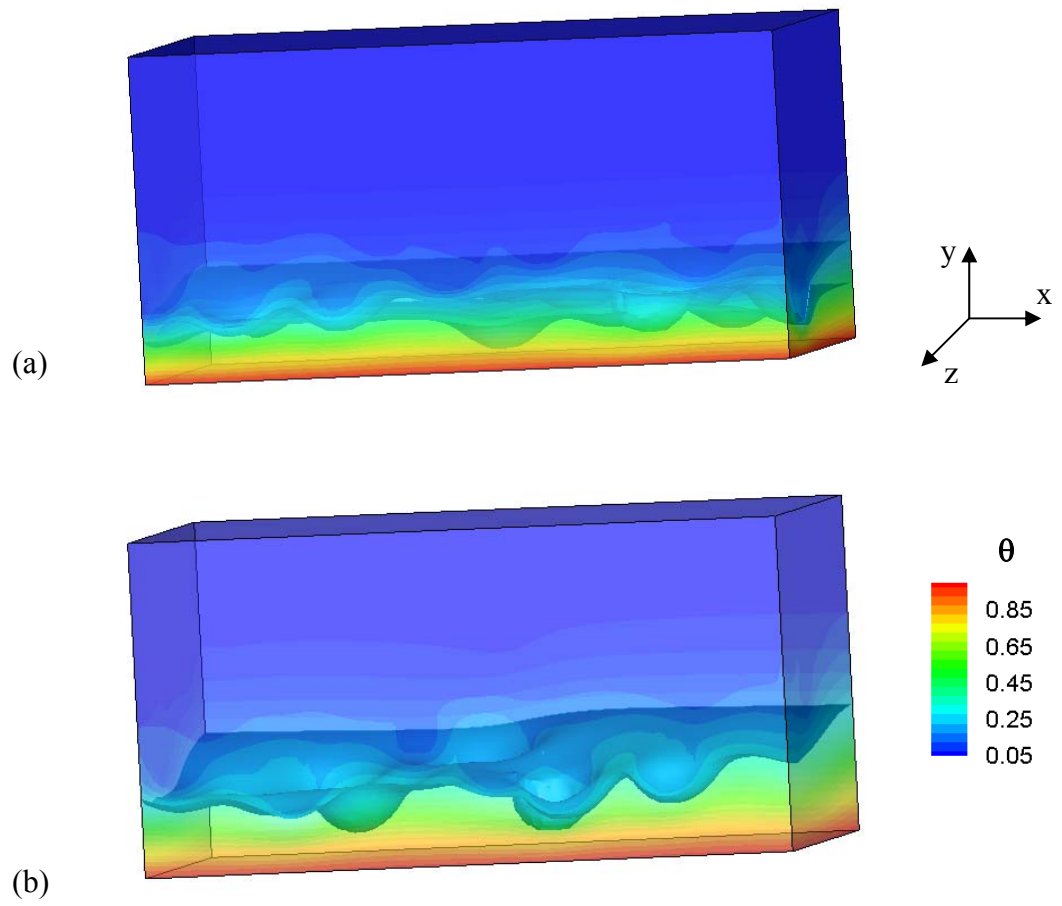


Figure 4.19. The effect of flow disturbance caused by moving particles on the temperature field in a sample sub-domain at different times ($\phi=5\%$)

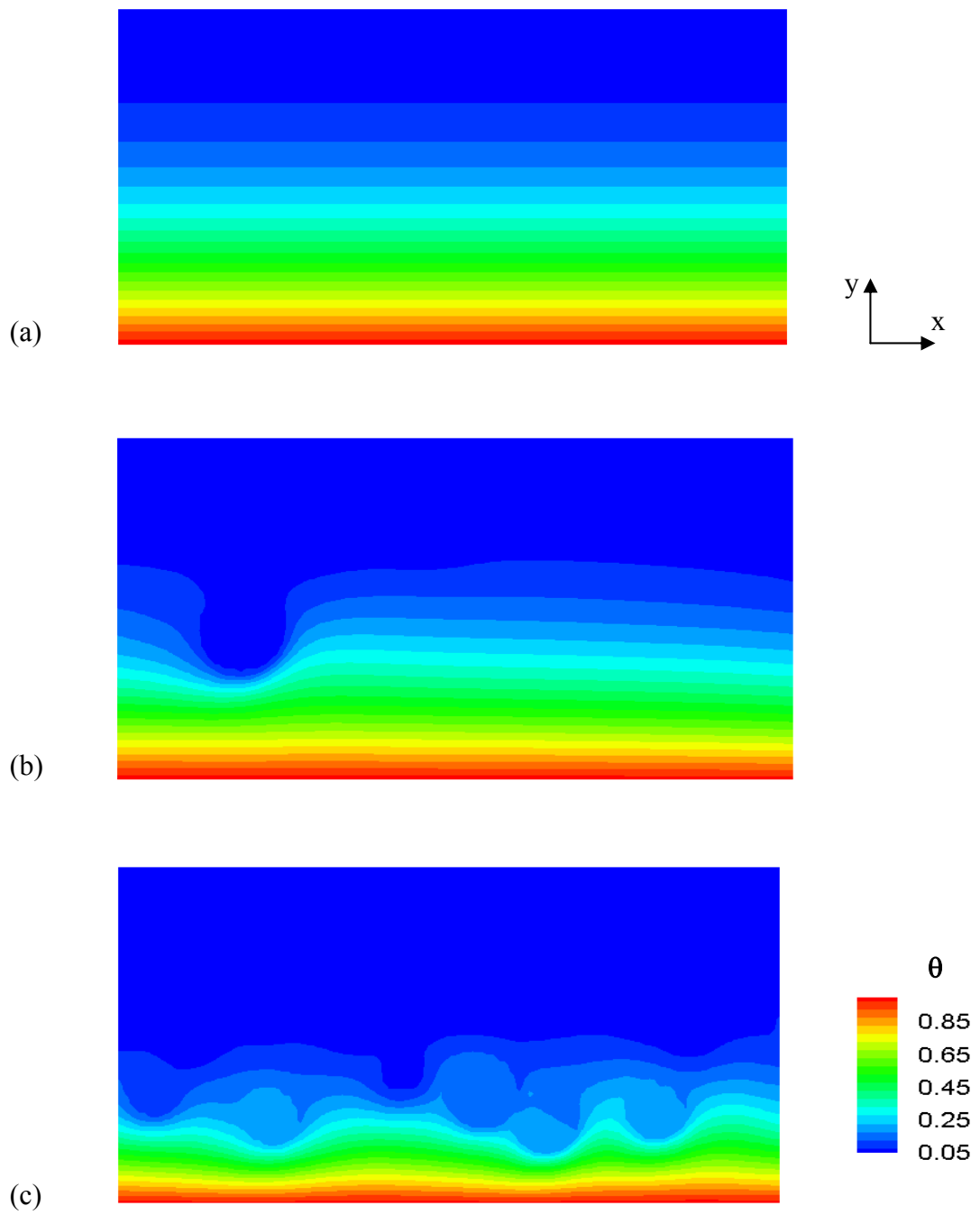


Figure 4.20. Comparing temperature field in a vertical plane in flow with 0, 1 and 5% solid particles

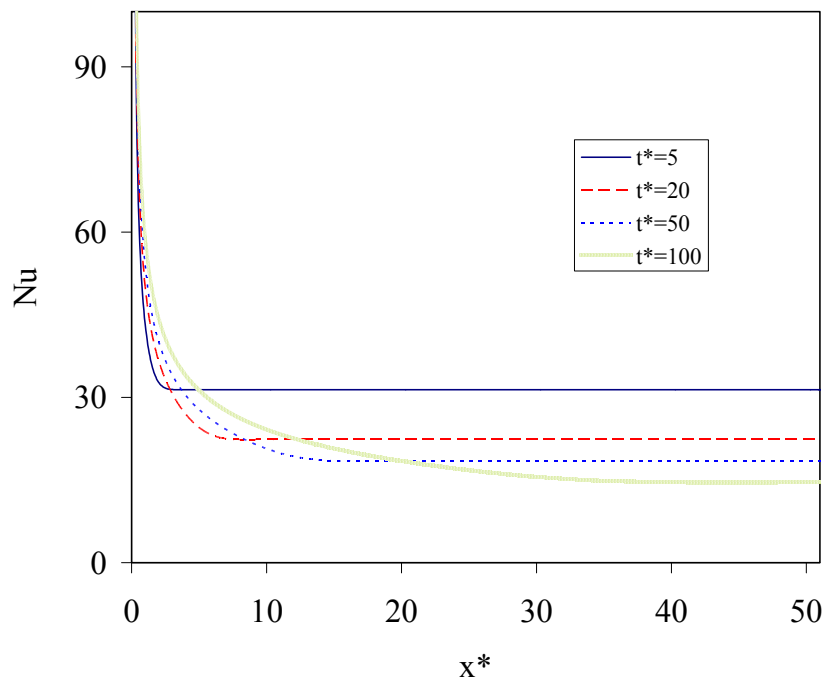


Figure 4.21. Wall Nusselt number at different times (no suspensions)

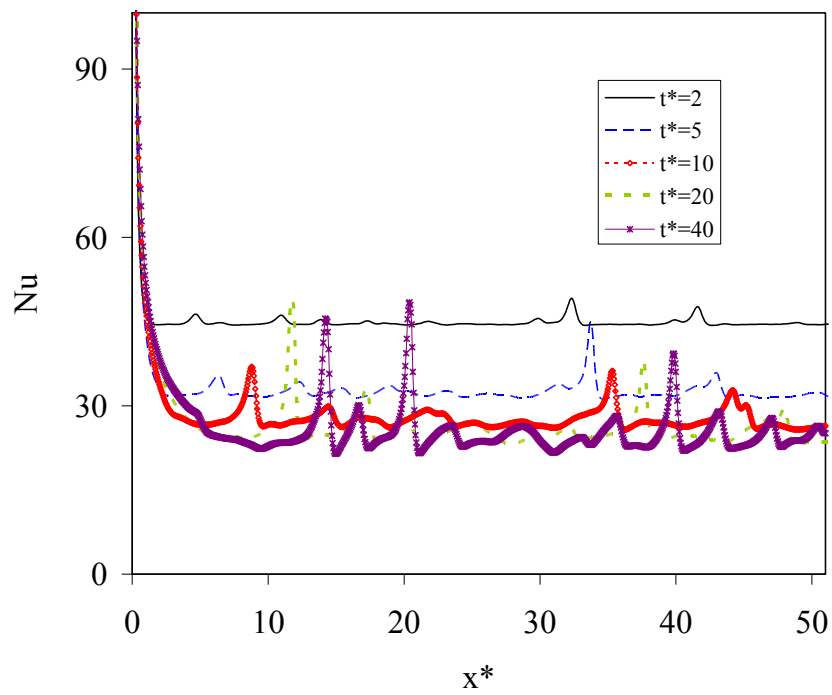


Figure 4.22. Wall Nusselt number at different times ($\phi=5\%$)

4.4.1 Effect of Particle Volume Fraction

Figure 4.23 compares the wall Nu at different time for zero and five percent volume fraction at $Re=40$. The local disturbances in Nu number are due to existence of particle in the vicinity of wall. It is observed that the average Nu is higher for a suspension flow. Figure 4.24 shows wall Nu for three different volume fractions. Here, Nu is normalized based on average Nu of a pure fluid. It is seen that the average Nu increases with increasing the volume fraction. However, the local jumps in Nu are much higher at 5 percent volume fraction compared to 1 and 2 percent. In that case particles are closer to each other and as is discussed in section 4.3.2, the upstream particle affects the flow downstream and this causes the local jumps to be higher.

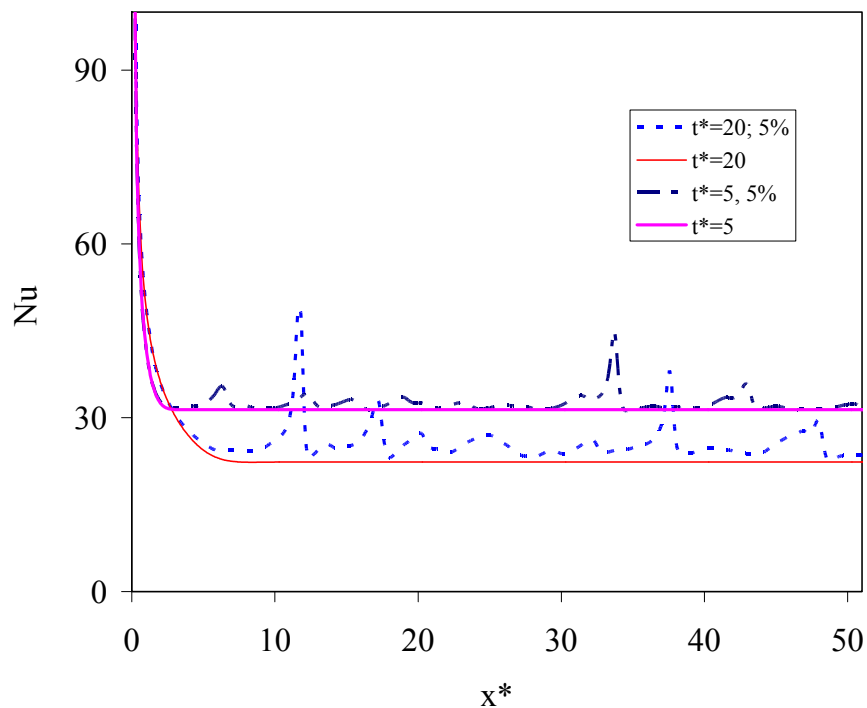


Figure 4.23. Comparing wall Nusselt number at different times

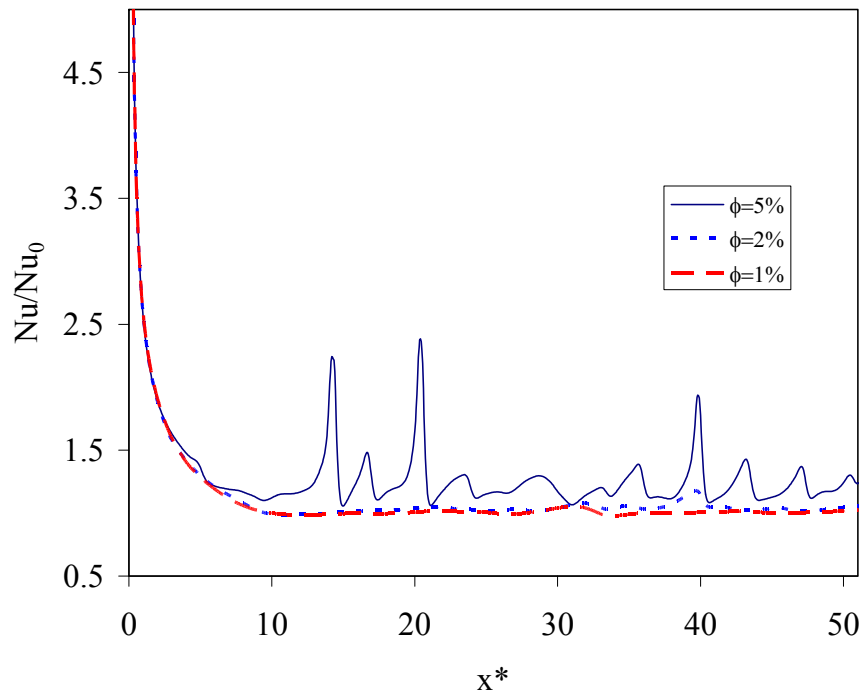


Figure 4.24. Effect of volume fraction on wall Nu

4.4.2 Effect of Reynolds Number

It was shown in the previous section that increasing Re increases the local jumps in wall Nu. Figure 4.25 shows the affect of Re on Nu along the channel wall. Nu is normalized based on average Nu of a pure fluid. It is observed that the local disturbances are higher at higher Re. It causes the average Nu to be higher at higher Re. The effect of Re is especially important at higher volume fraction as is shown in Figure 4.26.

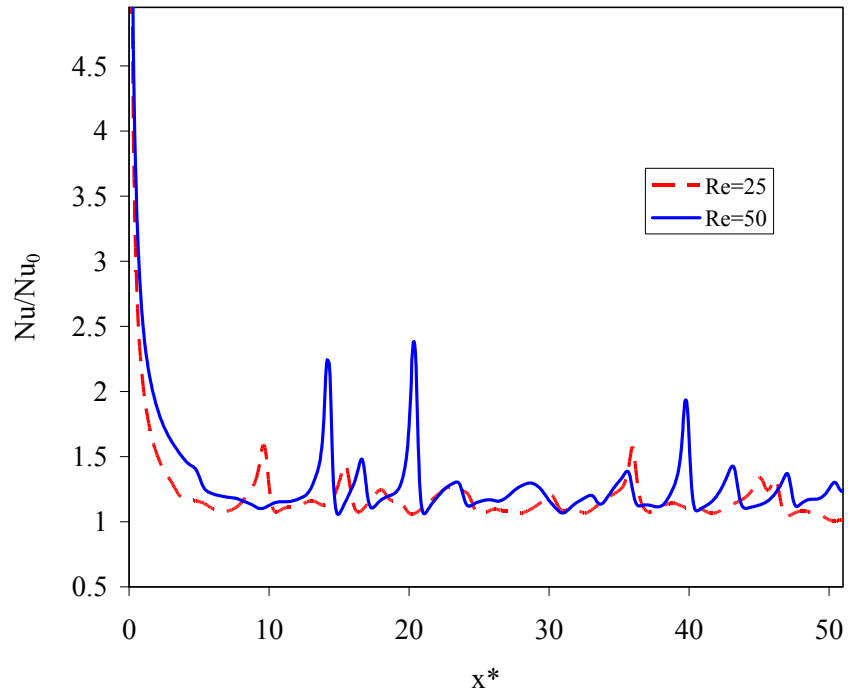


Figure 4.25. Effect of Re on wall Nu

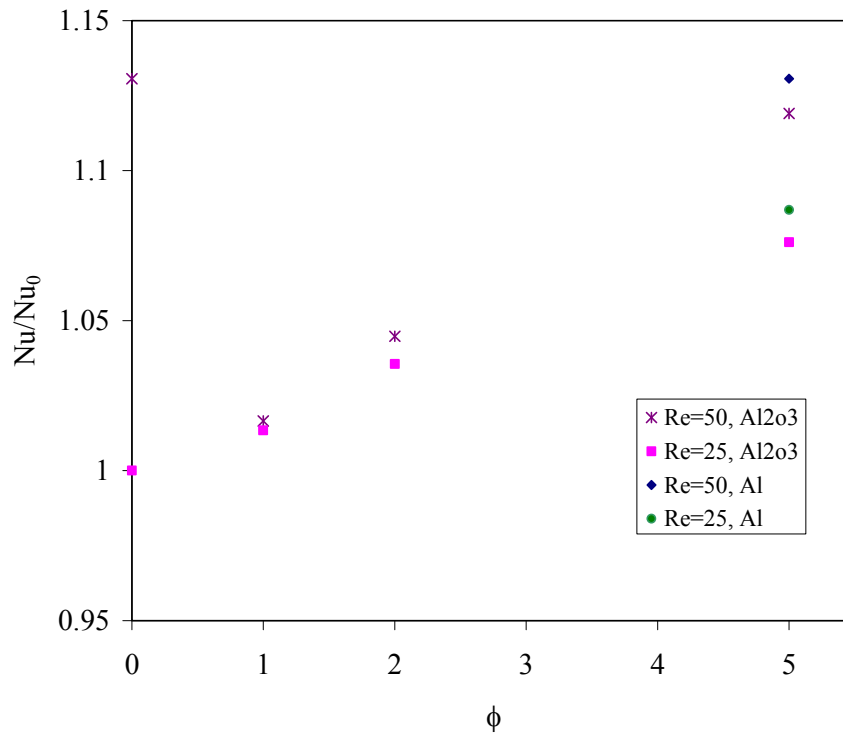


Figure 4.26. Effect of volume fraction and Re on wall Nu

4.4.3 Effect of Particle Thermal Conductivity

Solid suspensions have higher conductivity compared to the base fluid. Therefore the heat transfer is expected to be enhanced by increasing particle thermal conductivity. In Figure 4.26 compares Nu for Al₂O₃ and Al suspensions with thermal conductivity equal to 50 and 200, respectively. It is observed that using Al particles, the Nu is enhanced about one percent.

4.4.4 Effect of Particle Size

It was discussed in the previous section that the blockage ratio (or particle size) does not have an important effect on the amount of local Nu jump when particles are suspended freely in the flow. Figure 4.27 presents wall Nu along channel length for two different particle sizes. Nu is normalized based on average Nu of a pure fluid. It is observed that the average Nu is enhanced about 1 percent with 30 percent increasing particle size.

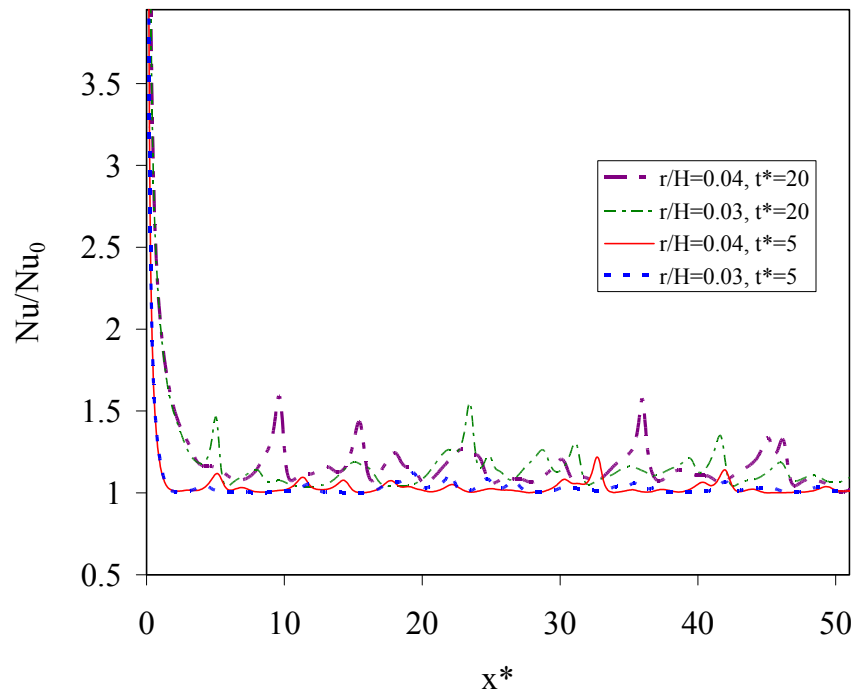


Figure 4.27. Effect of particle size on Nu

CHAPTER 5

HEAT TRANSFER IN HOT PRESS SECTION OF A PAPER

MAKING MACHINE

Paper is a complex material which consists of wood fibers. Paper making process includes several steps from fiber preparation to drying the final product. The fibers enter a paper making machine in dilute water suspensions. The fiber suspension or pulp moves through several sections in a paper machine. In Figure 5.1 a schematic of different sections in a paper making machine are shown.

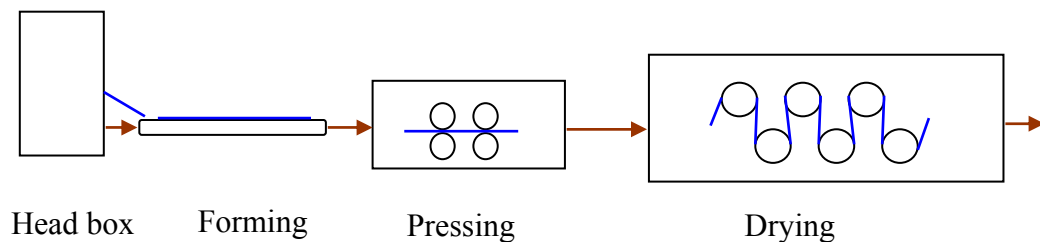


Figure 5.1. Different sections in paper making machine

There are three main sections in a typical paper making machine: Forming, Pressing and Drying. In the forming section, dilute fiber suspension move on a screen and some of its water is removed due to drainage caused by gravitational force. The consistency of the suspension which is defined as mass fraction of fibers is less than one

percent. The next section is the press section. In this section, the paper web moves through pressing rolls. This action removes most of the water from the fiber suspension. In fact, less than 0.5 percent of the initial water remains in the paper sheet after the press section. The remaining water is removed by evaporation in the drying section.

In a wood fiber suspension, water can exist in a bound or unbound form. The unbound or free water exists in spaces between fibers, or in large pores (diameter > 25 μm) within the fibers. The unbound water can be removed during pressing or drying sections. Bound water exists in small fiber pores with diameter less than 25 micrometers and is chemically adhered to the fibers. The bound water can only be removed by evaporation in the drying section [82].

5.1 Energy Consumption in Drying and the Effect of Hot Pressing

Paper making is an expensive and energy intensive process. Most of the energy is used in the dewatering sections. For each kilogram of paper produced, typically more than 200 liters of water enters a paper machine. Considering the large paper production around the world, it is evident that efficient dewatering is an important factor in determining the operational costs. Most of the water is removed in the forming and pressing sections. Less than 0.5 percent of the original water entering the paper machine remains to be removed by evaporation in drying section. However, the drying section uses the most amount of energy in the paper making process. The demands for energy efficiency and environmentally friendly production require more efficient methods for dewatering that use less energy. One of the technologies used to increase energy efficiency is hot pressing. The idea is to increase the pulp temperature before entering the

press section. This leads to higher mechanical water removal in the press section. Therefore, less amount of water is required to be removed by evaporation returning reduced energy consumption. Hot pressing is performed by moving the paper sheet through heated metal rolls. In hot pressing typically the surface temperature of rolls is less than 100 °C. Another similar technology is impulse drying in which the surface temperature is around 300 °C.

Increasing the temperature of paper sheet before the press section has several advantages [83-85]. It reduces the water viscosity, resulting in easier water removal. It reduces water surface tension resulting in reduction in rewet from capillary effects when the paper exits the press nip. It also results in more softened fiber networks which enhances paper compression. The disadvantages of elevated temperature during pressing are sticking of paper to the hot surface and delamination. Delamination is splitting of paper into separate layers [86, 87].

Figure 5.2 shows the effect of temperature on the dynamic viscosity of water. Viscosity decreases considerably with increasing temperature. The water flow through a porous medium (such as fiber network or felt) is related to viscosity. The relationship can be explained by Darcy's law:

$$u = -\frac{K}{\mu} \nabla p \quad (5.1)$$

Where μ is dynamic viscosity, K is permeability which depends on geometry, p is pressure and u is velocity. From equation (5.1), velocity is inversely proportional to the viscosity. This explains higher dewatering rates in press section while the paper sheet is

preheated. Efficient dewatering is very important, considering the small (about 10-50 ms) residence time in press nip. Experiments of Patterson et al. and Busker and Cronin show that any 10 °C increase in temperature increases the outgoing solids by 1 percent [88, 89].

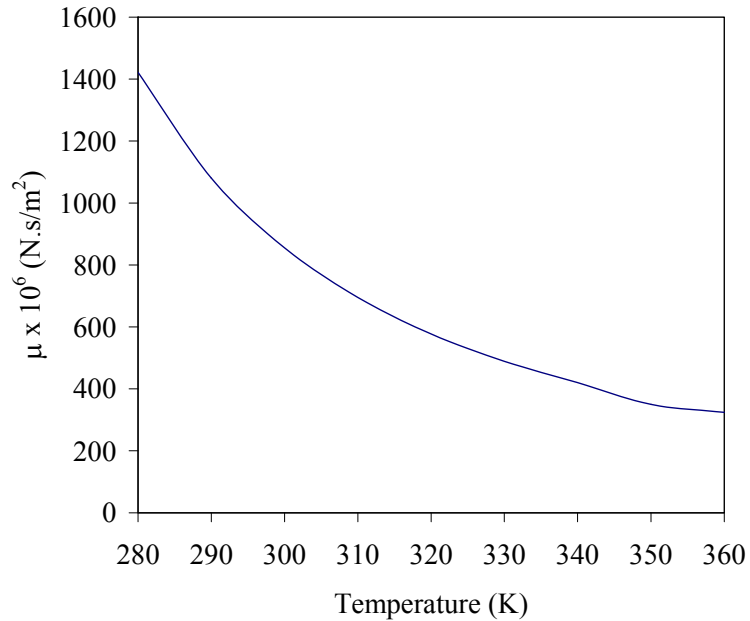


Figure 5.2. Effect of temperature on dynamic viscosity of water

It should be noted that increase in the consistency of the fiber suspension leaving the press section means less moisture content entering the dryer section. It leads to lower energy consumption for evaporation in the drying section. Table 5.1 shows that one percent increase in solids leaving the press section results in about 3-4 percent energy saving in drying section.

Consistency or solids is mass fraction of wood fibers in paper sheet and is defined

as:

$$S = \frac{m_f}{m_f + m_w}$$
$$S = \phi \frac{\rho_f}{\rho_{eff}} \quad (5.2)$$

Where, f, m, w, ρ and ϕ stand for fiber, mass, water, density and volume fraction respectively. Moisture ratio is defined as:

$$MR = \frac{m_w}{m_f}$$
$$MR = \frac{1}{S} - 1 \quad (5.3)$$

Table 5.1. Effect of consistency on energy usage

sheet temperature (°C)	20		
evaporation temperature (°C)	100		
heat of evaporation (kJ/kg)	2333		
steam temperature in dryer can (°C)	120		
heat of condensation (kJ/kg)	2203		
specific heat of water (kJ/kg/K)	4.18		
specific heat of fiber (kJ/kg/K)	1.34		
	<i>Case 1</i>	<i>Case 2</i>	<i>Case 3</i>
solids content of entering sheet	0.4	0.45	0.5
moisture ratio of entering sheet	1.5	1.22	1.00
energy to heat water (kJ/kg fiber)	500	410	330
energy to heat fiber (kJ/kg fiber)	110	110	110
energy to evaporate water (kJ/kg fiber)	3400	2700	2200
total energy (kJ/kg fiber)	4000	3200	2700
steam needed (kg / kg evaporated water)	1.8	1.5	1.2
<i>energy usage reduction (compared to case 1)</i>		<i>18%</i>	<i>35%</i>

5.2 Modeling Hot Pressing of Fiber Suspension

Considering the effect of heat transfer in fiber suspension in paper making it is important to have a good understanding of its heat transfer properties. Finding the temperature field inside the paper and required heat flow during hot pressing is important in the design of the press rolls and heat generating components. Several modeling studies have been conducted to predict thermal behavior in hot pressing and other drying

sections. In section 6.2.1, a review of the previous studies on hot pressing is presented. In section 5.2.2, the thermal properties of fiber suspensions are investigated using numerical simulations.

5.2.1 Previous Experimental and Numerical Studies

The properties of wood fibers vary with wood type and environmental conditions. The variety of fiber types and other parameters such as density and temperature make it difficult to rely only on experiments. Accurate models can be used to better understand the physical phenomena and predict the effect of design parameters. Several researchers have studied heat transfer in wood fiber based composites both experimentally and numerically [90-92]. They cover different heating sections in paper making, such as preheating and hot pressing, impulse drying and evaporative drying [93-96].

Busker and Cronin studied the effect of pulp temperature on pressing performance [88]. Patterson et al. designed and tested an apparatus for web preheating [89]. Walker has investigated different hot pressing technologies [85]. Lindsay et al. have experimentally studied heat transfer in linerboard [84, 97]. The surface temperature range in their experiments is from 125 to 300 °C. They have shown that increasing the mechanical pressure in press heating at low surface temperature does not have an important effect on heat transfer. They have also tried to model paper sheet as a semi-infinite body. However, their experimental results over estimate heat flux compared to industrial scale tests. Krook and Stenstrom performed experiments on Swedish softwood pulp heating at 100 to 300 °C surface temperature [87]. They used several thermocouples to measure temperature at different vertical positions along the paper thickness. Later,

Nilsson and Stenstrom analyzed these experiments using a simple model [98]. Zombori et al. applied a two dimensional numerical approach to simulate the structure of oriented strand board and predict its thermal conductivity [99]. In this model no free water is simulated and only wood fiber and air are considered. Dai et al. presented a mathematical formulation to model heat transfer in wood composites during hot pressing as a porous structure [100, 101]. They assumed a simplified porous structure for the wood panel and used semi-empirical predictions for effective values of parameters such as thermal conductivity. Thoemen and Humphrey presented numerical simulations to model heat transfer in pressing of relatively thick medium density fiberboard (MDF) [102]. They assumed no free water is present in the composite. Later, Thoemen et al. used x-ray tomography to determine the structure of MDF and obtained semi-empirical formulations for parameters such as thermal conductivity and permeability [103].

5.2.2 Problem Description

Figure 5.3 presents a schematic of the problem. The paper sheet moves through a heated roll. The upper cylinder is heated by saturated steam and its surface temperature is held constant. Due to the high speed of the paper sheet and small contact area, the residence time is small, typically around 50 ms. Here, the transient heat transfer phenomenon is studied using the domain shown in Figure 5.3. The initial and boundary conditions are selected as follows. The upper plate is assumed to be at constant temperature. The other boundaries have zero temperature gradient due to small residence time and small length scales. The temperature field and heat flux are assumed to be continuous at the interface of the fiber and water. The initial temperature is the ambient

temperature. Since the temperature range in hot pressing is below 100 °C, no phase change occurs. In fact, as discussed by Krook and Stenstrom [87], when the hot surface temperature is below 150 °C no phase change is observed, considering the minimum pressure applied in pressing. They have also shown that in this temperature range the applied pressure only has a minor effect on heat transfer.

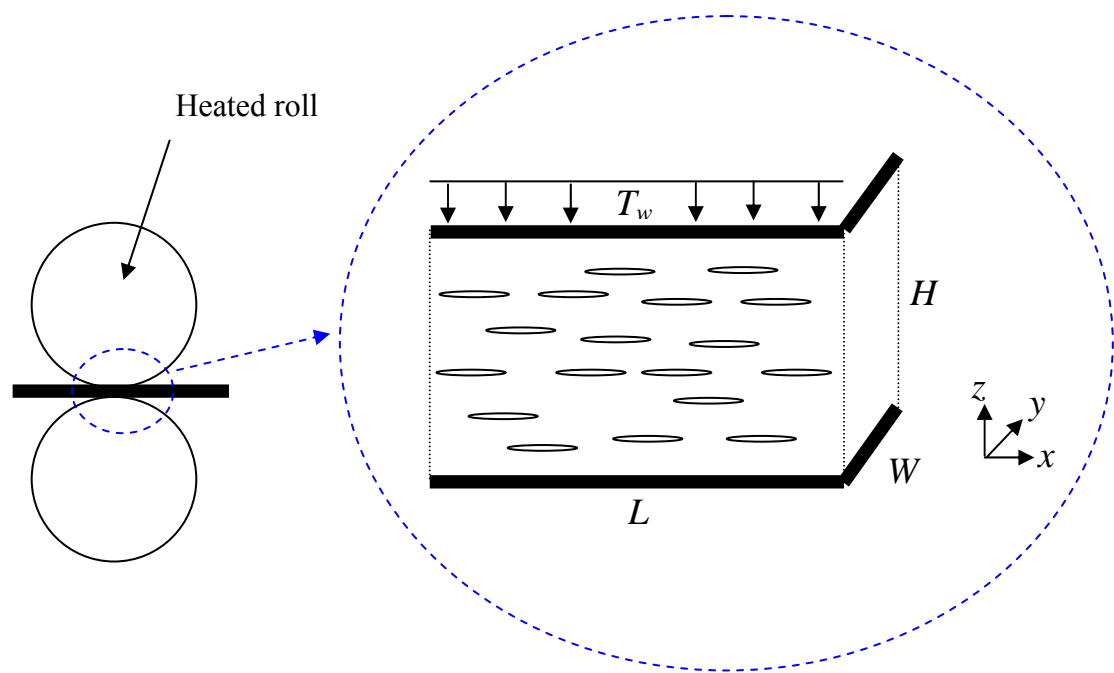


Figure 5.3. Schematic of hot pressing of fiber suspension

The properties of water depend on temperature. Figure 5.4 and Figure 5.5 show the variation of wood thermal conductivity and Prandtl number with temperature. The properties of fibers depend on wood type and environmental conditions [90, 104]. The

properties of hardwoods and softwoods are different. Three types of wood fibers are investigated here. Their properties are listed in Table 5.2.

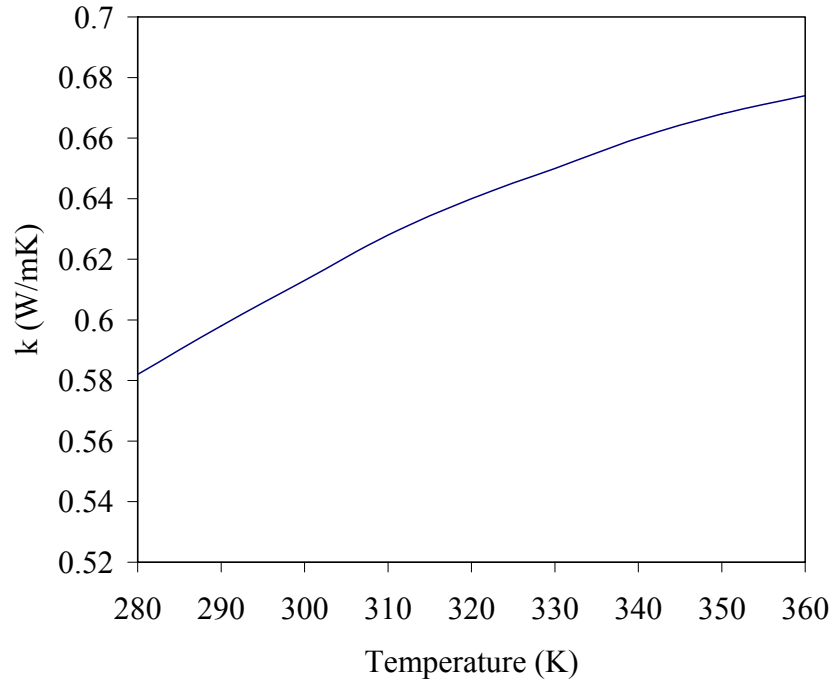


Figure 5.4. Effect of temperature on water thermal conductivity

Table 5.2. Properties of wood fibers

wood	k (W/m.K)	c_p (J/kg.K)	ρ (kg/m ³)
Southern pine	0.15	2500	600
Oak	0.17	2000	900
Swedish softwood [98]	0.335	1340	1550

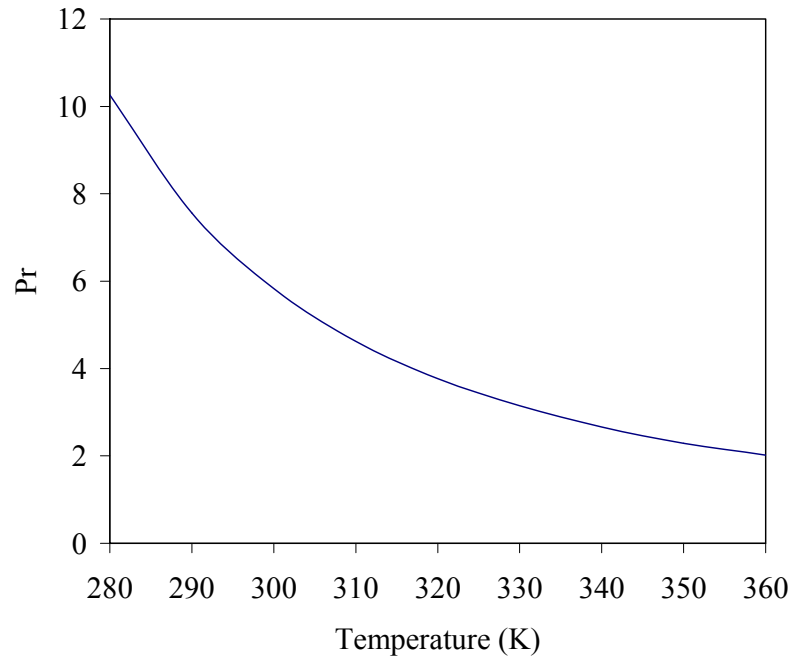


Figure 5.5. Effect of temperature on water Prandtl number

5.2.3 Method Validation and Results

Figure 5.6 to Figure 5.8 present the temperature variation with time in a paper sheet while in contact with a hot surface. The current numerical results are compared with the experimental results reported by Krook and Stenstrom [87] who performed experiments using Swedish softwood pulp on a test hot pressing setup. The basis weight (BW) of the sample paper is 60 g/m^2 . The BW is the mass of the paper sheet per unit area and is defined as:

$$\begin{aligned}
 BW &= \frac{m_f + m_w}{W \times L} \\
 BW &= S \cdot \rho_{eff} \cdot c
 \end{aligned}
 \tag{5.4}$$

Where, c stands for paper thickness or caliper. The over dried BW is defined as:

$$OD.BW = \frac{m_f}{W \times L} \quad (5.5)$$

The consistency is 30 percent. Therefore, the paper sheet thickness (caliper) is 180 μm . The press residence time is about 50 ms. The surface temperatures are 100 $^{\circ}\text{C}$ and 150 $^{\circ}\text{C}$. They measured the temperature at three vertical positions. Figure 5.6 and Figure 5.7 show the temperature at $z=2/3H$ for $T_w=100^{\circ}\text{C}$ and 150 $^{\circ}\text{C}$, respectively. Figure 5.8 shows the temperature at $z=1/3H$ for $T_w=150^{\circ}\text{C}$. It is observed that there is a good agreement between the present simulations and the results of Krook and Stenstrom.

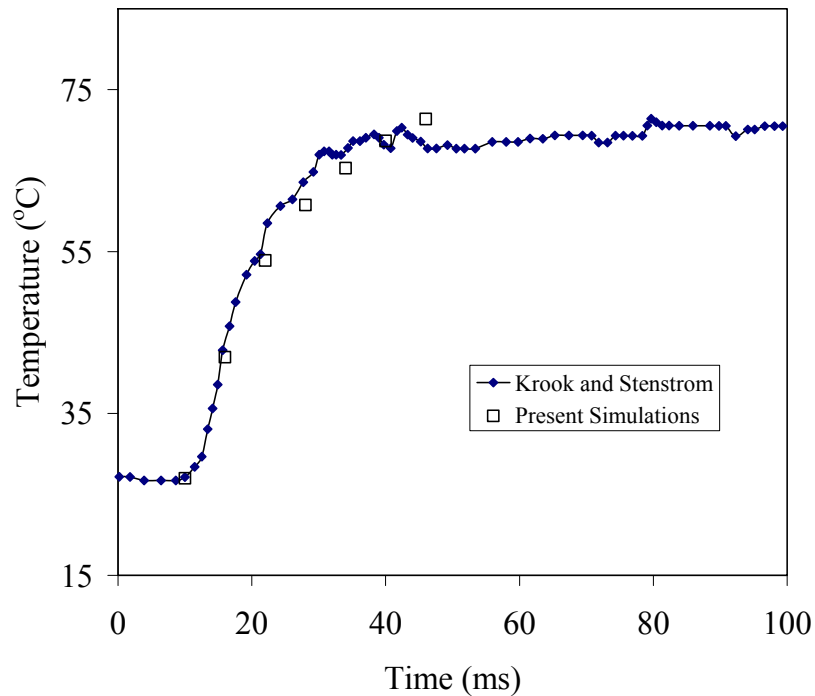


Figure 5.6. Temperature in paper sheet at 2/3 of caliper; $T_w=100^{\circ}\text{C}$

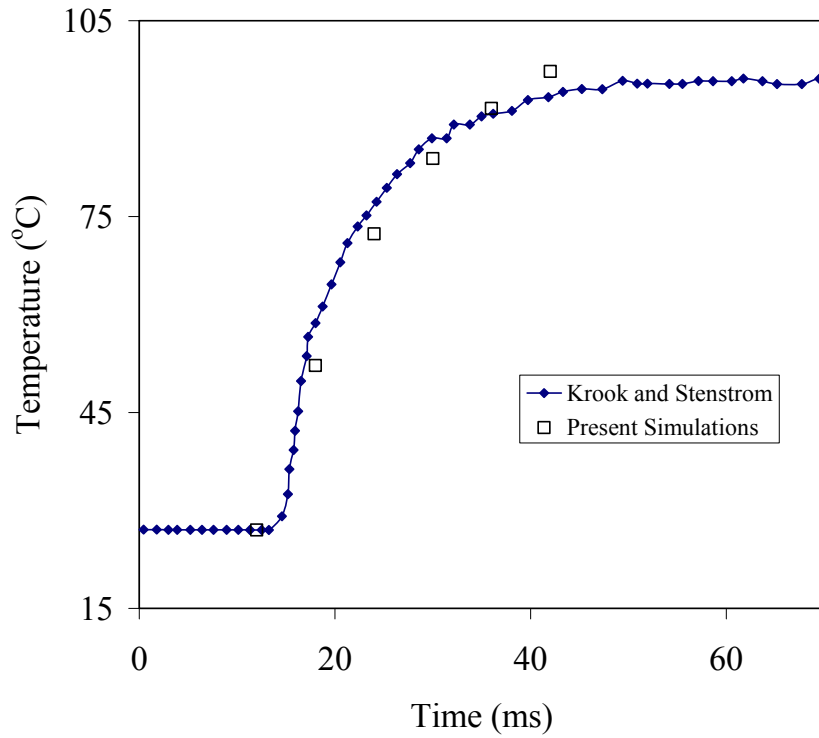


Figure 5.7. Temperature in paper sheet at 2/3 of caliper; $T_w=150\text{ }^\circ\text{C}$

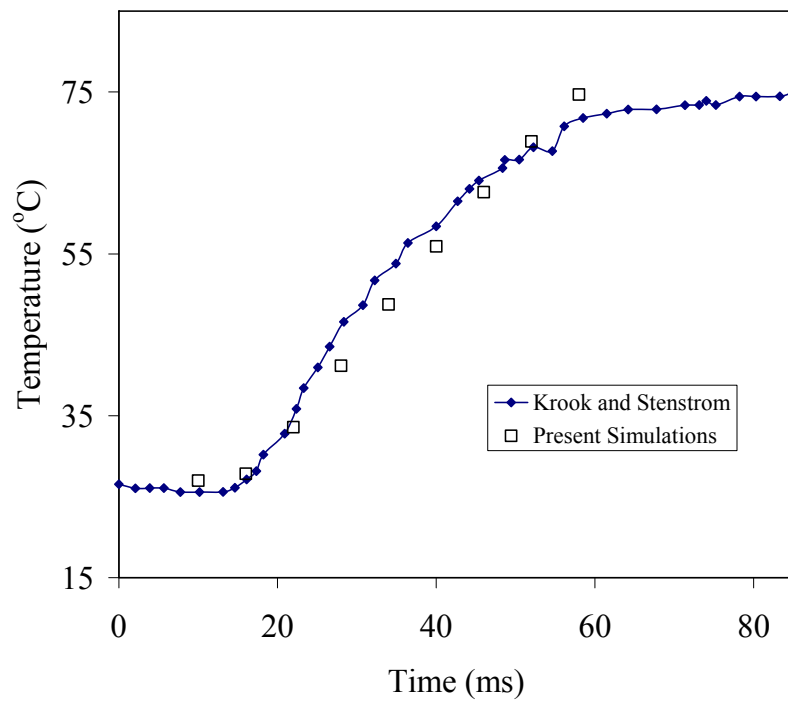


Figure 5.8. Temperature in paper sheet at 1/3 of caliper; $T_w=150\text{ }^\circ\text{C}$

Figure 5.9 presents the transient temperature in hot pressing of a paper sheet made of Swedish softwood pulp. The fiber volume fraction in the simulated sample is 20 percent ($S=0.3$), and the caliper is $180\ \mu\text{m}$. The hot surface temperature is $100\ ^\circ\text{C}$. The results presented in Figure 5.10 are at $T_w=150\ ^\circ\text{C}$. It is seen that the rate of temperature increase decreases with time. This happens since the temperature difference between the hot surface and the paper sheet decreases. However, the thermal conductivity of the paper is expected to increase with temperature. It shows that the effective thermal conductivity is not enhanced at higher temperatures. The effect of temperature on effective conductivity is discussed in the next sections.

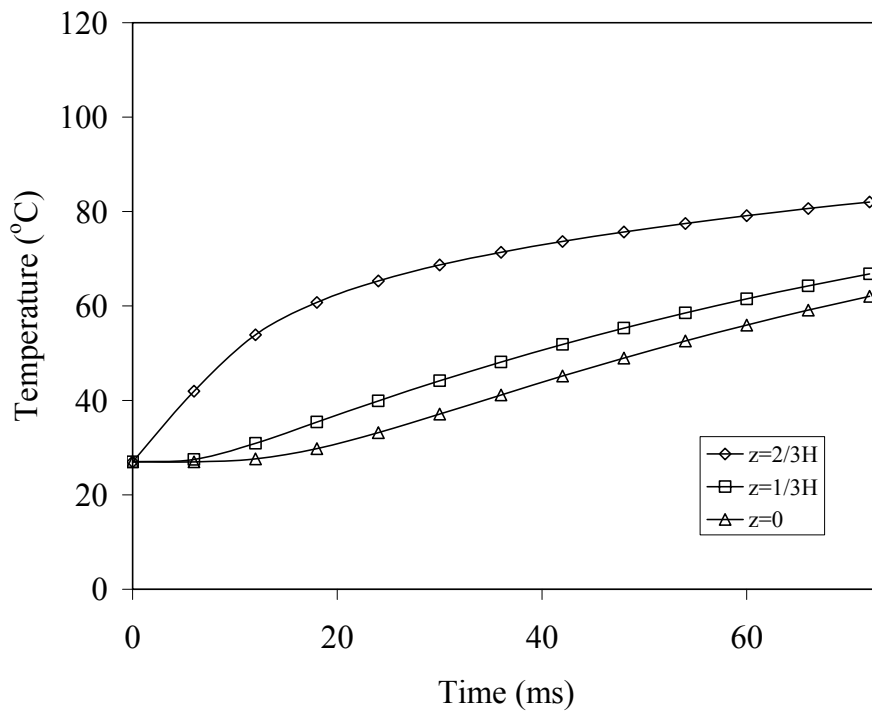


Figure 5.9. Temperature in Swedish softwood pulp paper sheet; $T_w=100\ ^\circ\text{C}$

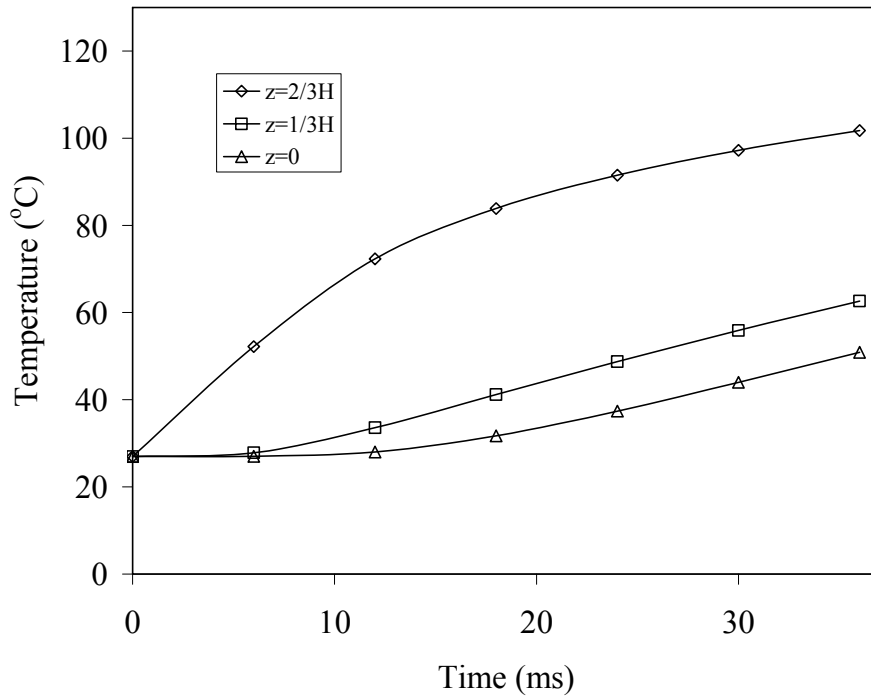


Figure 5.10. Temperature in Swedish softwood pulp paper sheet; $T_w=150\text{ }^\circ\text{C}$

Figure 5.11 and Figure 5.12 present the transient temperature for a paper sheet made of southern pine fibers with $\phi=0.2$ and $c=180\text{ }\mu\text{m}$. The hot surface temperature is $100\text{ }^\circ\text{C}$ and $150\text{ }^\circ\text{C}$, respectively. The temperature inside paper sheets made of Swedish softwood pulp is higher compared to paper sheets made of southern pine pulp at similar contact times. This suggests that the effective conductivity is higher in the first case.

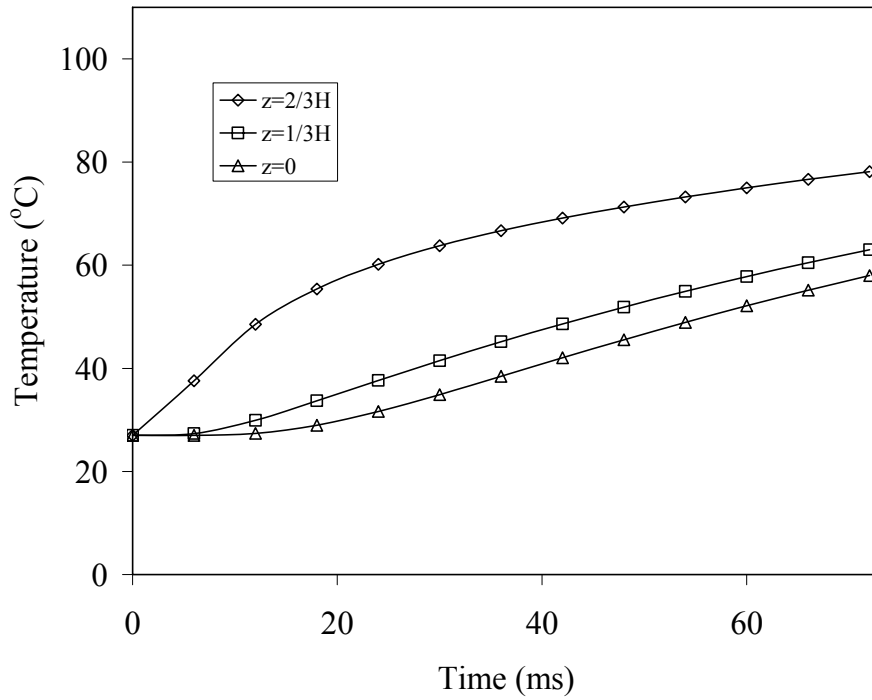


Figure 5.11. Temperature in southern pine paper sheet; $T_w=100\text{ }^\circ\text{C}$

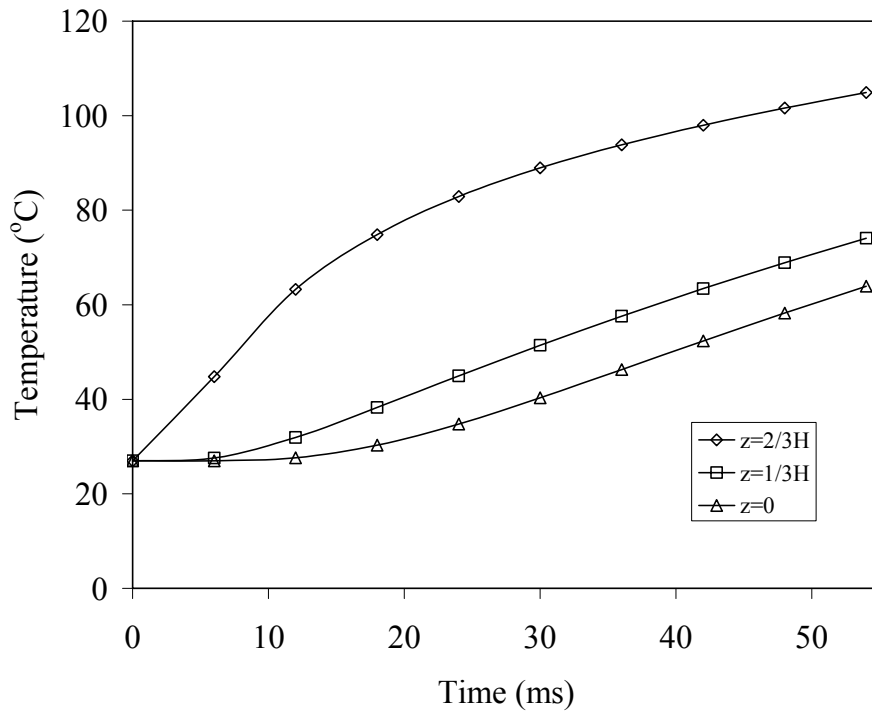


Figure 5.12. Temperature in southern pine paper sheet; $T_w=150\text{ }^\circ\text{C}$

5.2.4 Effect of Temperature and Solid content on Effective Thermal Conductivity

In this section, the effective thermal conductivity of a fiber suspension is calculated numerically. In the previous studies, the effective conductivity is usually calculated based on averaging or is estimated based on experimental results. The present method can be used to predict thermal properties based on different parameters such as fiber type, consistency or temperature.

5.2.4.1 Effect of Moisture Ratio on k_{eff}

Figure 5.13 presents the effect of moisture content on the effective conductivity of a paper sheet. The samples are made of for southern pipe, oak and Swedish softwood pulp. As seen in this figure, k_{eff} increases with increasing MR. This is because water has higher thermal conductivity compared to wood fibers.

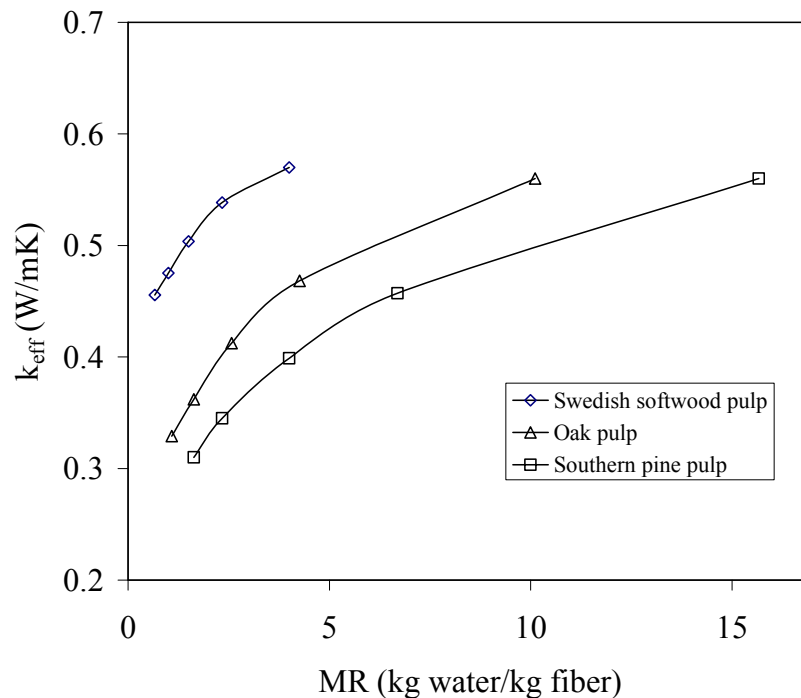


Figure 5.13. Effect of MR on k_{eff}

Figure 5.14 presents the effective conductivity for three fiber types with respect to solid content. It should be mentioned that because of the difference in densities of different wood fibers, the consistencies are equivalent to different volume fractions in each case. For example $\phi=0.4$ corresponds to $S=0.5$ in southern pine pulp, 0.4 in oak pulp and 0.3 in Swedish softwood pulp. Therefore, although the thermal conductivities of oak and southern pine fibers are close, they have different effective pulp thermal conductivities at the same consistency because of the difference in density.

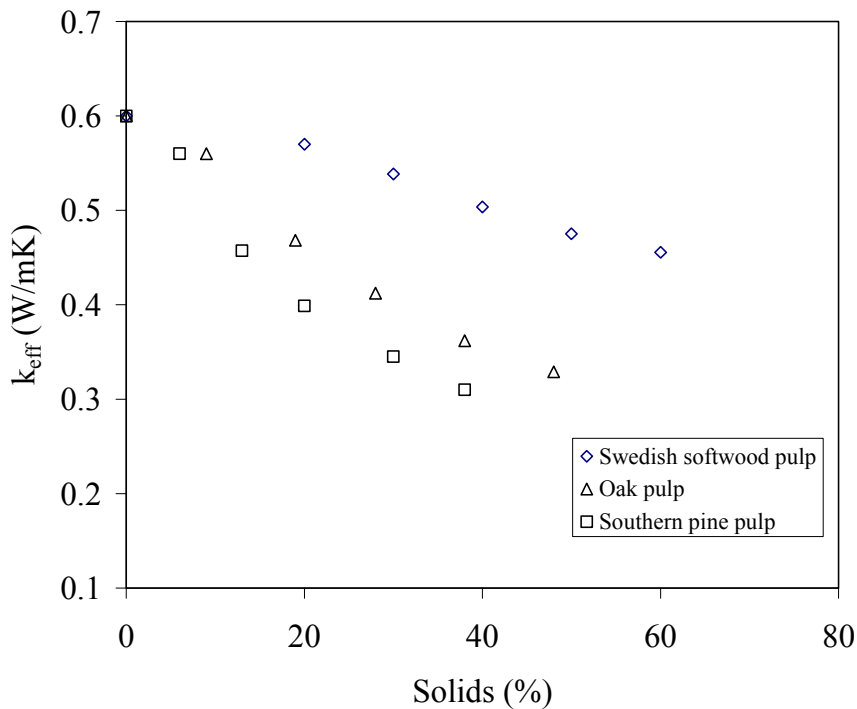


Figure 5.14. Effect of solids on k_{eff}

5.2.4.2 Effect of Temperature on k_{eff}

The effect of temperature on k_{eff} for three wood fiber types at $\phi=50\%$ is presented in Figure 5.15. Considering Figure 5.4, it is seen that water conductivity increases with

temperature in the temperature range studied here. On the other hand, fiber conductivity does not change significantly in this temperature range [104]. It is observed that the increase in effective conductivity of pulp is less than 5 percent. Figure 5.16 shows the effect of temperature on k_{eff} for Swedish softwood pulp at different consistencies. It is seen that the effect of temperature is higher at lower consistency. This is due to higher dependency of water conductivity on temperature compared to fiber.

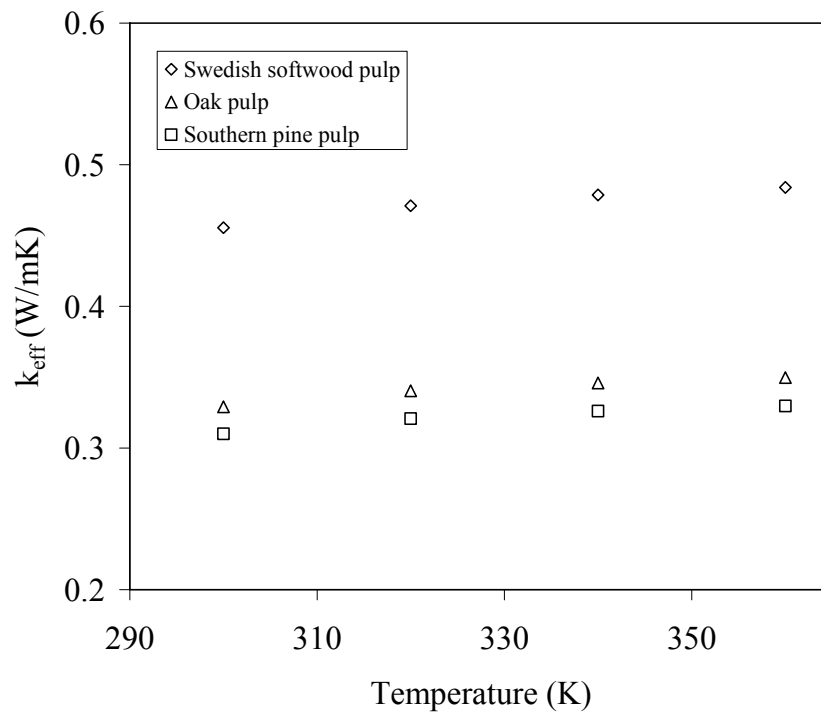


Figure 5.15. Effect of temperature on k_{eff}

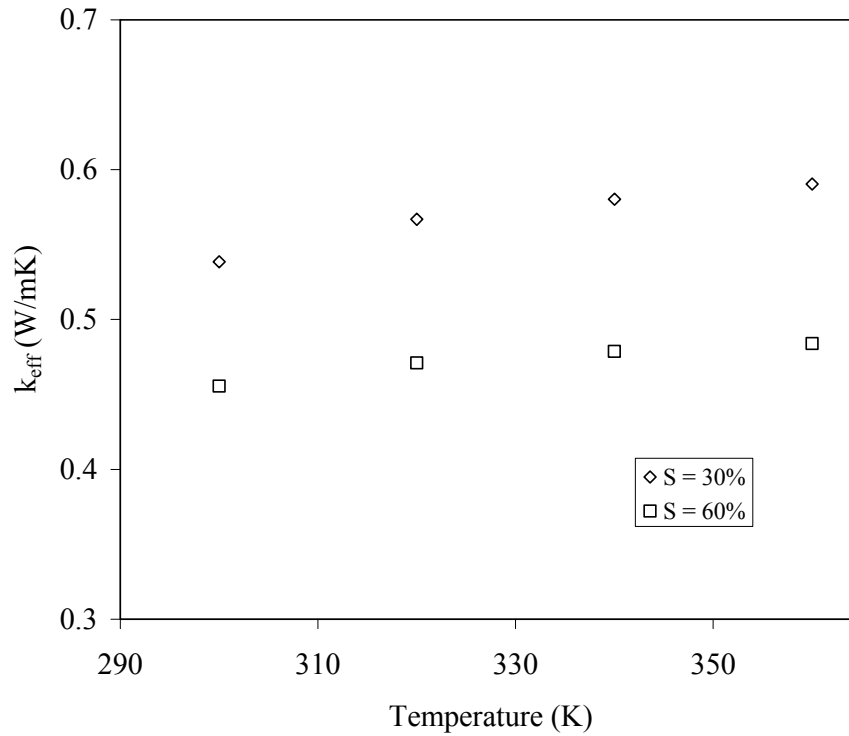


Figure 5.16. Effect of Swedish softwood pulp consistency and temperature on k_{eff}

5.2.5 Modeling Paper Sheet as a Semi-Infinite Body

Some researches have tried to model heat transfer in paper sheet during hot pressing as heat transfer in a semi-infinite body [97, 98]. In this section, the validity of this assumption is investigated. Transient heat transfer near a surface subjected to specified thermal condition in a medium can be modeled as heat transfer in a semi-infinite body as long as no boundaries near the surface impact the transport. The temperature profile in a semi-infinite body with constant surface temperature can be obtained by [105]:

$$\frac{T(z,t)-T_w}{T_i-T_w} = \text{erf}\left(\frac{z}{2\sqrt{\alpha t}}\right) \quad (5.6)$$

Where, T_i is the initial temperature, t is time, z is the distance from the hot surface and α is thermal diffusivity. The non-dimensional temperature can be defined as:

$$\theta = \frac{T(z,t)-T_i}{T_w-T_i} \quad (5.7)$$

It is reasonable to apply this model for transient heat transfer in paper as long as the temperature change in the unheated surface of paper is less than 5 percent ($\theta_c < 0.05$). Figure 5.17 shows the non dimensional temperature distribution in a paper sheet obtained based on equation (5.6). The assumption of semi-infinite body is valid for $t < 5$ ms if the caliper is larger than 100 μm . Figure 5.18 shows the non dimensional temperature at the unheated surface of paper sheet with different BW. The sample is Swedish softwood pulp with $S=0.3$ and $T_i=300$ K. The heating time is 50 ms. Based on this figure, in this condition the semi-infinite body model can be used with less than 5 percent error if the basis weight of the sample is higher than 100 g/m^2 . Figure 5.19 compares the present simulation results with equation (5.6). The sample is a paper sheet at $\text{BW}=120$ g/m^2 made of Swedish softwood pulp. It is observed that above 50 ms the relative error is large. The minimum paper basis weight in which the model is valid for $t < 50$ ms heating is presented in Table 5.3 and Table 5.4 for Swedish softwood pulp and southern pine pulp.

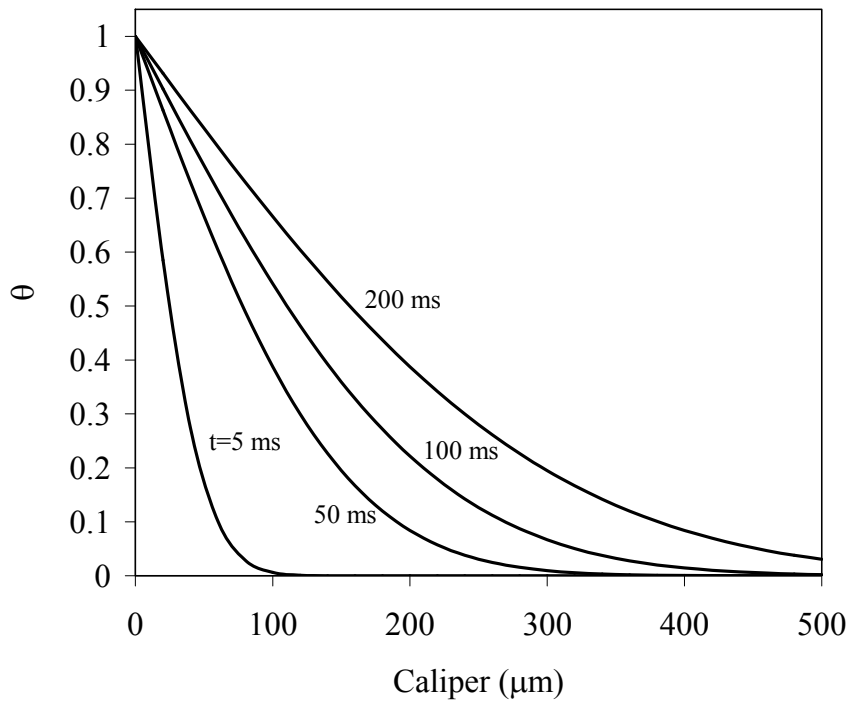


Figure 5.17. Non-dimensional temperature in a paper with $c=180 \mu\text{m}$

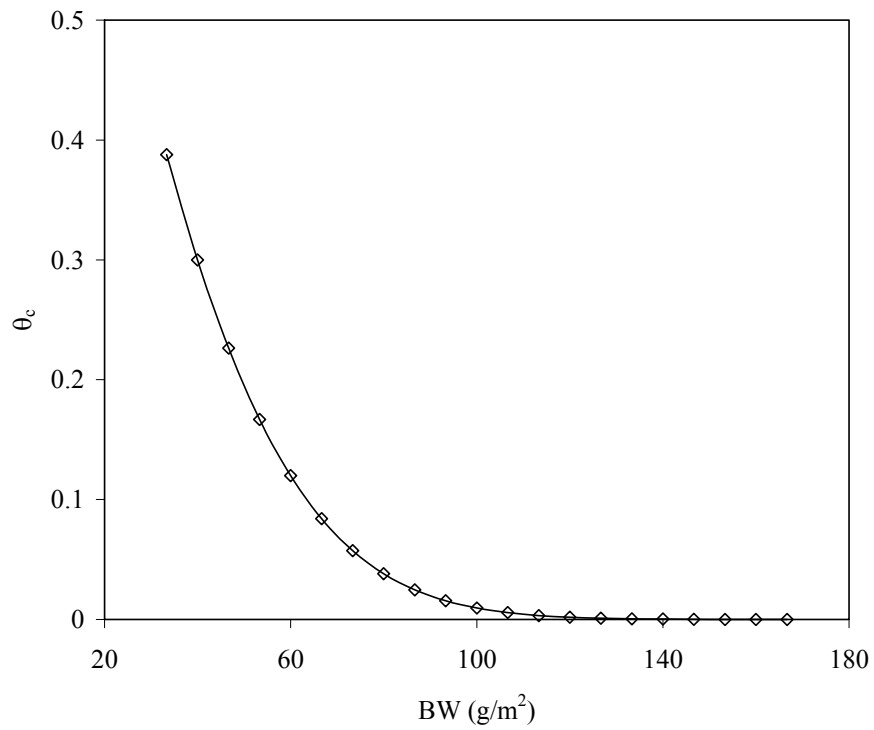


Figure 5.18. Non-dimensional temperature at unheated surface

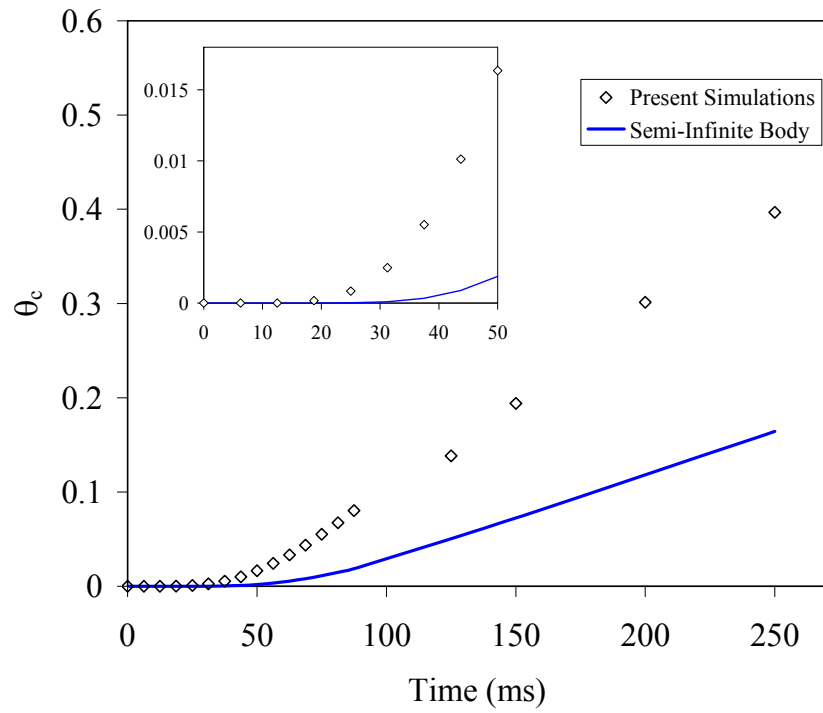


Figure 5.19. Non-dimensional temperature at unheated surface for Swedish softwood pulp at $BW=120 \text{ g/m}^2$

Table 5.3. Minimum BW for validity of semi-infinite body modeling for Swedish softwood pulp ($t < 50 \text{ ms}$)

S	ϕ	BW (g/m^2)
0.05	0.03	12
0.1	0.07	24
0.2	0.14	49
0.3	0.22	76
0.4	0.30	105
0.5	0.39	137
0.6	0.49	171
0.7	0.60	210
0.8	0.72	255

Table 5.4. Minimum BW for validity of semi-infinite body modeling for southern pine pulp ($t < 50$ ms)

S	ϕ	BW (g/m^2)
0.05	0.08	11
0.1	0.16	22
0.2	0.29	41
0.3	0.42	58
0.4	0.53	73
0.5	0.63	85
0.6	0.71	96
0.7	0.80	104
0.8	0.87	110

CHAPTER 6

THERMAL PROPERTIES OF PARTICLE LADEN MIXTURES IN SQUEEZE FLOW

The increase in the heat generation rate of electronic components and the importance of compactness of electronic systems requires more efficient thermal packaging. Therefore, there has been extensive research on minimizing the overall thermal resistances in such systems. In this chapter we investigate the thermal properties of thermal interface material which is a key element in thermal packaging.

6.1 Thermal Interface Materials

Thermal Interface Materials (TIM) are used in electronics packaging to enhance heat transfer between heat dissipating components such as electronic chips, and thermal packaging components such as heat spreaders [13]. A common type of TIM is thermal grease. In an effort to improve thermal performance of thermal greases, particulate TIMs which are mixtures of thermal grease and highly conductive solid particles are extensively used. The effective thermal conductivity of the TIM grease is around 0.1-0.4 W/mK [13, 14]. Adding micro size solid particles with high thermal conductivity can increase the effective thermal conductivity 5-10 times, with values of 2-5 W/mK reported [14]. Effective thermal conductivity of these TIMs depends on the loading fraction and physical properties of the particles, such as thermal conductivity and size. Increasing the particle loading affects both the viscosity of the TIM and the minimum bond line

thickness (BLT) [15]. Increasing BLT increases thermal resistance which is not desired [16].

Particle laden TIM is an example of a multi-component fluid. The thermo-physical properties of these complex fluids are often very different from the base fluid. In fact, complex fluids are non-Newtonian and have a strain rate dependent viscosity with yield stress. Due to the various applications of such mixtures, it is important to determine their transport properties. During the package assembly process, TIM is dispensed between the two surfaces that are to be in contact, and then the surfaces are pushed together [17]. Therefore, the TIM goes through a squeezing step which needs to be considered in modeling of its thermal characteristics.

The experimental methods for measuring thermal characteristics of TIMs are usually based on the ASTM D5470 tester [15]. Such measurements are not easy to perform for $BLT < 100 \mu\text{m}$ for solids, and in general for greases. Also, for non-homogeneous TIMs such as particulate filled greases, they do not determine the structure of the TIM mixture, or the BLT. Once the package has been assembled it is difficult, if not impossible, to disassemble it and measure the BLT or study the structure. A review of experimental methods for TIM thermal conductivity measurements is provided by Goel et al. [106].

There has been much effort in the literature to develop models to predict thermo-physical properties of particle laden TIMs. The classical methods consider a disperse suspension of solid particle in the base matrix for vanishing interfacial thermal resistance, such as the well known Maxwell type formulations which are valid for volume fractions

less than percolation threshold [107, 108]. The Hashin-Shtrikman (H-S) bounds are obtained based on the effective medium theory and suggest lower and upper limits for thermal conductivity of composites [107, 108]. Nielsen has presented a formulation for two phase composites [109], which overestimates the effective conductivity, especially at higher particle volume fractions. There have been several modifications or extensions to formulations based on effective medium theories, to consider the interfacial resistances at higher particle volume fractions. Every et al. presented a modified Bruggeman model that includes an empirically specified Biot number to account for the interfacial thermal resistance between the solid particles and the base grease [20]. Using this model, Prasher et al. have derived a correlation to predict the thermal resistance of particulate TIM assuming it to be a Herschel-Bulkley fluid [19].

Phelan and Niemann have used thermal resistance network calculations to predict the effective thermal conductivity of randomly oriented composites [110]. McPhedran et al. have presented analytical solutions for the effective conductivity of lattices of spheres in certain cubical arrangements [111, 112]. Their work is an extension to the previous work by Rayleigh [113]. Torquato has derived an expression for the effective thermal conductivity of dispersions which is sensitive to the microstructure [114]. This approximate expression is valid while the disperse solids are not close to each other. Pham and Torquato have extended this approach to isotropic multiphase composites [115].

Kim and Torquato have applied a Brownian motion technique to simulate the effective thermal conductivity of particulate suspensions in regular and random

arrangements [116-118]. In this method, they have used first-passage-time analysis to compute the appropriate mean times. A random-walk of a Brownian particle which represents diffusing species is used to calculate the average transport behavior of the suspension. Kanuparthi et al. have used a meshless computational procedure based on formalism of hierarchical partition of unity field compositions to simulate heat transfer in microstructures [119]. They have utilized this method to develop several random distributions of particles and then calculated the average thermal conductivity of the mixture. Their method is based on constructing complex behavioral fields through Boolean compositions of primitive fields. Figure 6.1 compares a number of above-mentioned models. The differences between the predicted values of different methods is due to differences in models employed, such as effect of particle size, shape, thermal conductivity, volume fraction, and particle distribution.

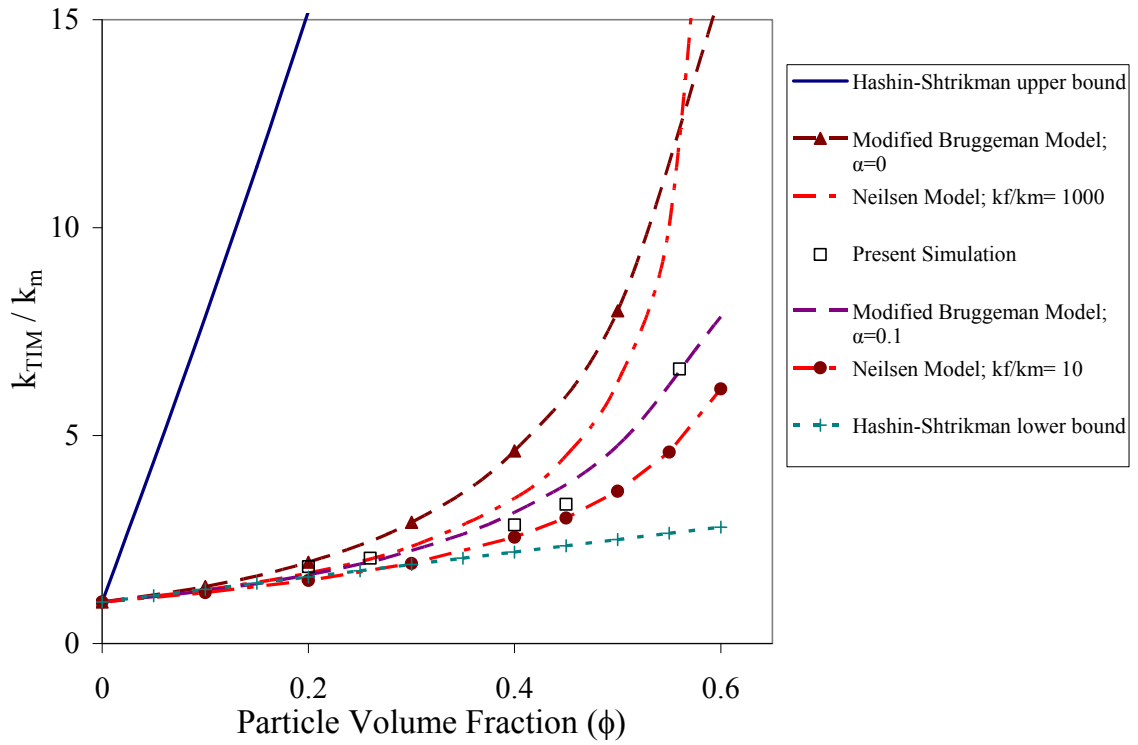


Figure 6.1. Different models for the effective thermal conductivity of a particle laden TIM

In the present study, numerical simulations are utilized to investigate the effect of key factors on the effective thermal conductivity of particulate TIMs. The present approach is not limited to a specific particle distribution, particle shape, or size. By simulating the squeezing process, we obtain the actual particle distribution in realistic working conditions. Therefore, there is no need to assume pre-defined random distributions. Here, we develop an efficient and accurate model based on numerical simulations of suspended particles are used to predict the thermal properties of particle laden TIMs. Based on the simulations, the effects of particle parameters such as loading,

thermal conductivity and size on the thermal conductivity of TIM are predicted. The predicted results are compared with existing experimental data and semi-analytical models.

6.2 Problem Description

Figure 6.2 presents a schematic of the physical domain and the relevant parameters. Thermal grease mixed with highly conductive metallic particles is placed between two flat plates. The lower plate has a uniform heat flux, q_w'' , and simulates a heat generating component and the upper plate is held at a constant temperature, T_{cold} , simulating a heat sink. Solid particles are assumed to be uniformly distributed initially in the matrix (assuming that the particles are well dispersed in the mixture) with volume fraction ϕ , but after the squeezing step the distribution of particles evolves with flow. A constant pressure is applied on the upper plate to simulate the squeezing pressure during component packaging. The particles are assumed to be freely suspended in the base matrix, which is assumed to be a Newtonian fluid such as silicone oil ($k=0.2$ W/m.K). However, the non-Newtonian effects are captured via direct simulation of particle movements and their interactions with the base fluid.

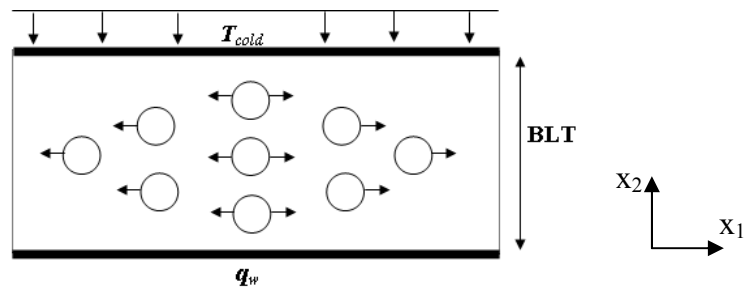
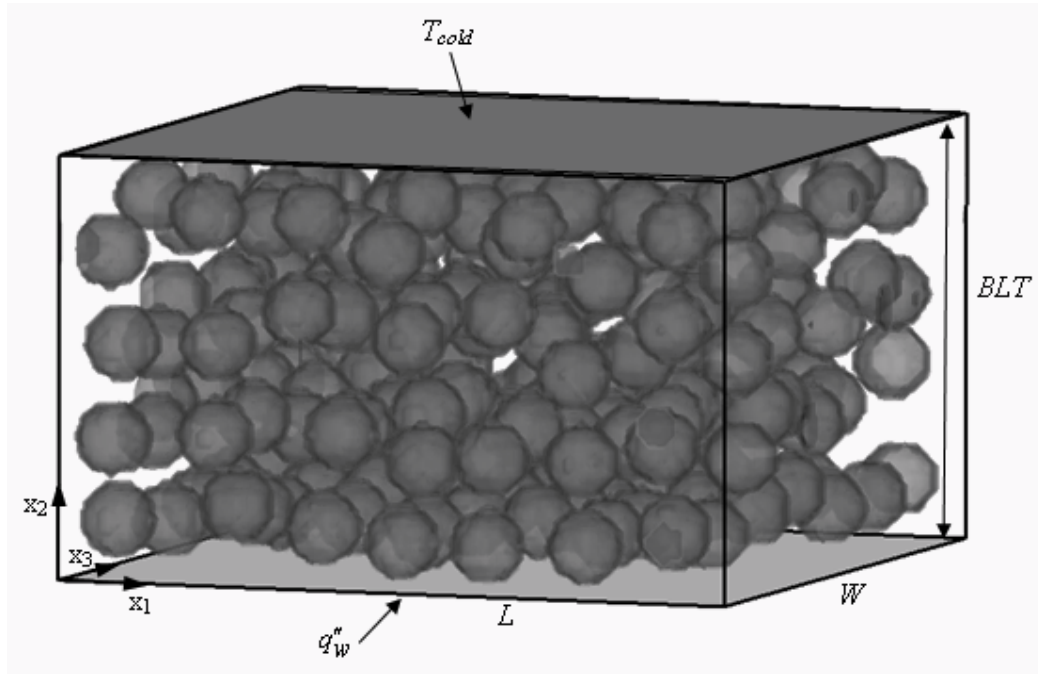


Figure 6.2. Schematic of the physical domain

Stress free and zero temperature gradient (adiabatic) boundary conditions are applied at the outlet boundaries at $x_1=0, L$ and $x_3=0, W$. Since the components are usually square, we assume $L=W$ in the simulations. After the squeezing step, the particle distribution is obtained. Figure 6.3 shows particle distribution after squeezing for a two dimensional simulation.

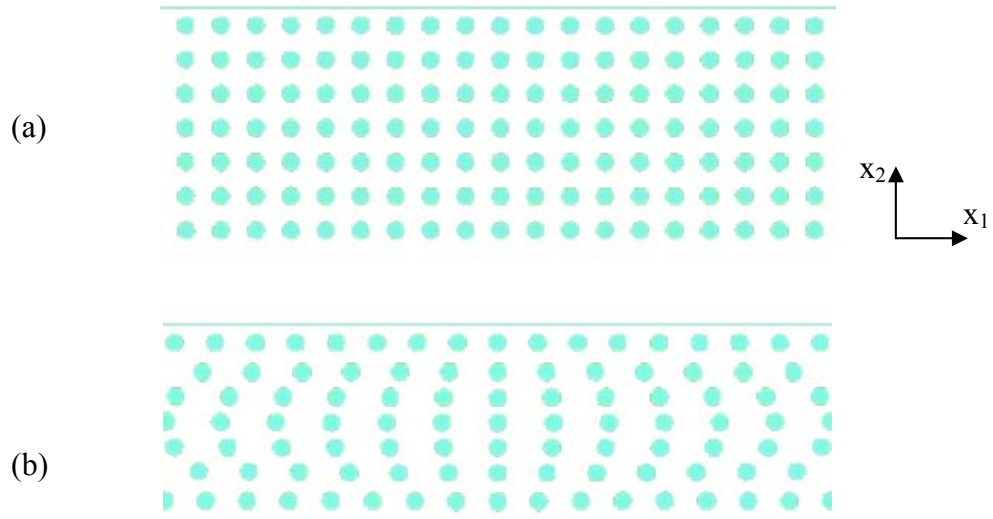


Figure 6.3. Particle distribution before (a), and after (b), squeezing

The thermal calculations are performed to obtain the steady state temperature distribution in the domain. Then, having the applied heat flux and calculating the temperature gradient, the effective thermal conductivity is obtained.

Thermal resistance of a TIM sample is defined as:

$$R = R_{th} + R_c \quad (6.1)$$

Where, R_c is the contact thermal resistance between TIM and the plates and $R_{th} = \frac{BLT}{k_{TIM}}$ is the bulk thermal resistance of TIM. k_{TIM} is the effective thermal conductivity of TIM and BLT (bond line thickness) is the thickness of the TIM.

The non dimensional temperature is defined as:

$$\theta = \frac{T - T_{cold}}{\frac{q_w'' \cdot BLT}{k_m}} \quad (6.2)$$

6.3 Simple Cubic Arrangement

To verify the computational method, we have calculated the effective thermal conductivity for simple cubic arrangement of solid spheres for two different thermal conductivity ratios. The results are presented in Figure 6.4 and Figure 6.5. The results have been compared with the existing literature. Bonnecaze and Brady have performed a numerical study for this arrangement [120, 121]. The particle configurations have been generated based on a Monte Carlo method. The results of the Brownian motion simulations of Kim and Torquato [117], and the analytical solution of McPhedran and McKenzie [111], are also presented. As observed from the results, the current predictions match well with the previous studies.

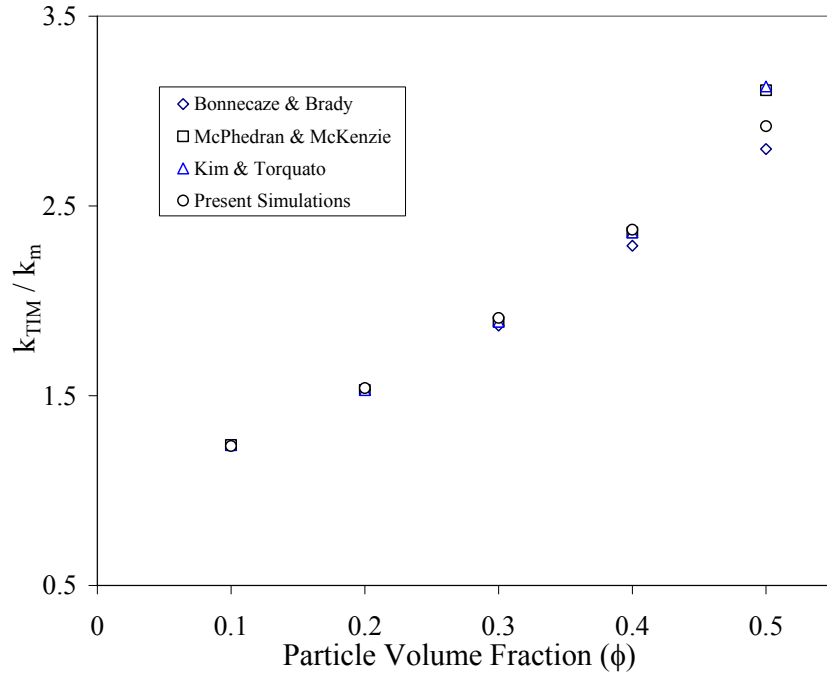


Figure 6.4. Effective thermal conductivity for simple cubic arrangement; $\frac{k_f}{k_m} = 10$

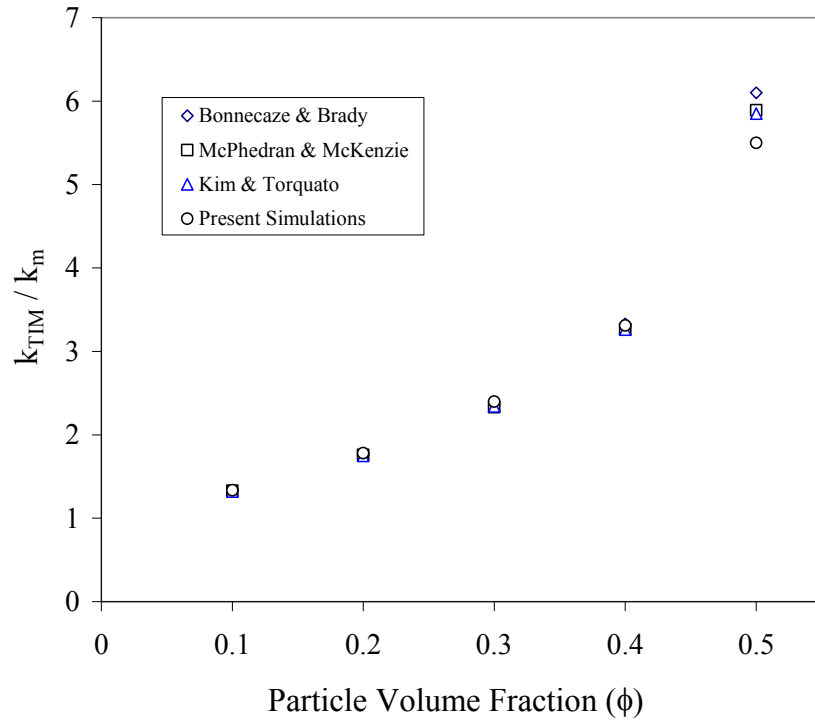


Figure 6.5. Effective thermal conductivity for simple cubic arrangement; $\frac{k_f}{k_m} \gg 1$

6.4 Microstructure and Particle Distribution

As mentioned earlier, the particle distribution is an important factor in determining the thermal properties of solid suspensions. The previous studies have examined different arrangements such as simple cubic, body centered, face centered, or random. Here, utilizing squeeze flow simulations, we are able to generate the actual particle distribution resulting from the assembly process. Figure 6.6 shows particle distribution in a sample simulation ($\phi=30\%$) before and after squeezing. The projections of the particle distribution onto the horizontal (at $x_2=0$) and vertical ($x_3=w/2$) planes show that although the particle-to-particle distance is decreased in the vertical direction, it is increased in the horizontal directions. It is observed that the particle distribution is not uniform or random after the squeezing step, which should be considered while evaluating the thermal performance of TIMs. Figure 6.6-d presents the local effect of each particle and the overall effect of particle configuration on the temperature profile in a vertical plane.

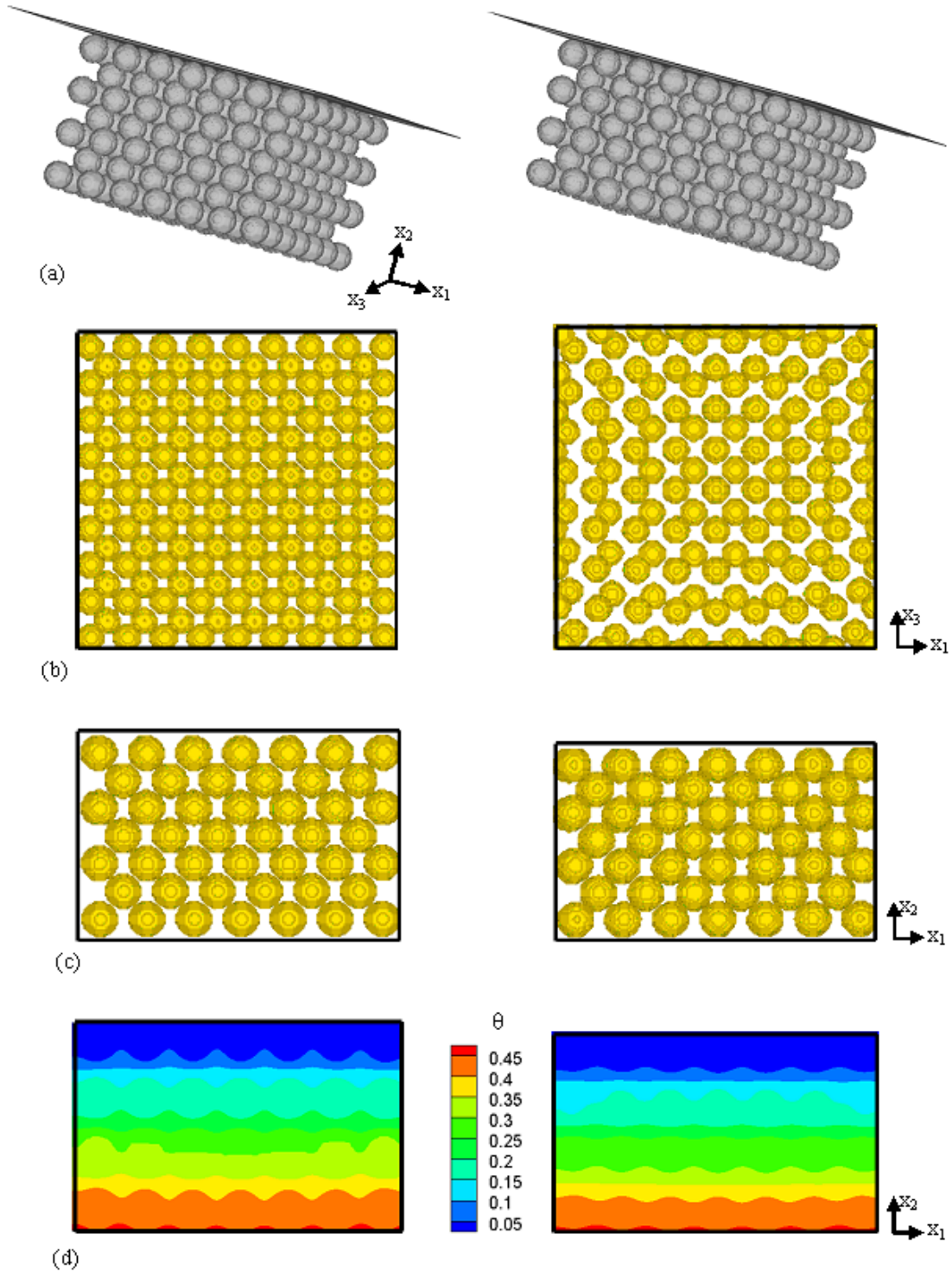


Figure 6.6. Particle distribution before (left) and after (right) 10% squeezing. a) three dimensional particle distribution, b) particle distribution projection at the horizontal plane ($x_2=0$), c) particle distribution , and d) temperature profile at the vertical (x_1-x_2) center plane

When the TIM is squeezed between two flat plates, two particle stack lines form in the diagonal directions. This effect has been observed in earlier experiments by Linderman et al. [14, 17] and is due to the symmetry of the squeeze flow between the two square plates. Figure 6.7 presents the velocity vectors and temperature distribution (deviations from the mean planar value) in the x_1 - x_3 mid-plane. The stacking lines are observed in Figure 6.7-a and b. It is seen that, because of the stacking of particles there is relatively lower temperature and higher heat flux in the diagonal directions. During the squeezing, the TIM mixture tends to move to the sides, away from the diagonals. Therefore, as is shown, the particles along the diagonal symmetry lines move with less velocity and are more likely to stack on each other. Linderman et al. (Figure 6.7-a) have presented a picture that shows this effect using a mixture of silver particles and PDMS using a glass chip for visual access. Based on these observations, Linderman et al. designed hierarchical nested surface channels to reduce the BLT at a certain applied pressure [14, 17].

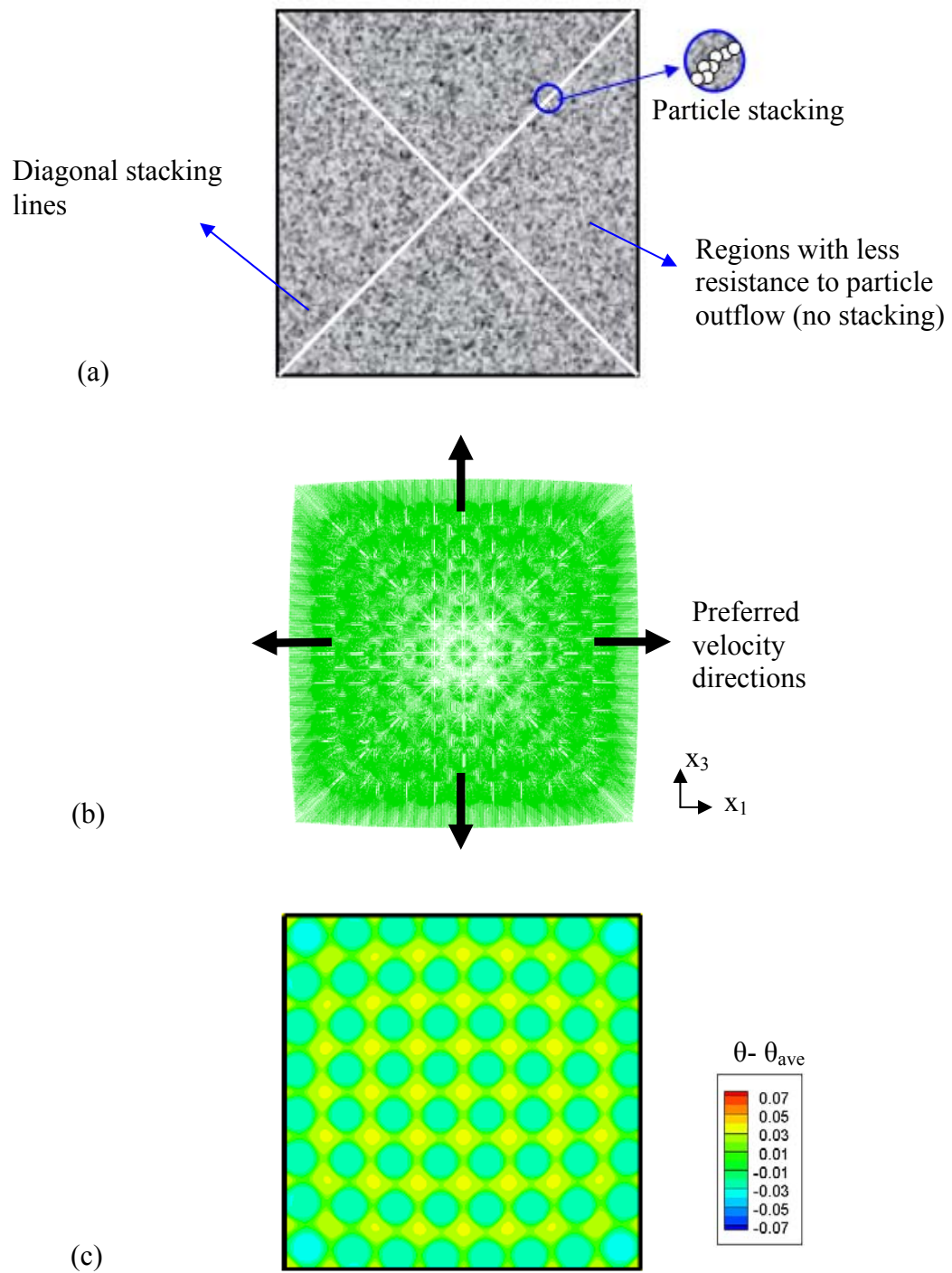


Figure 6.7. (a) particle stacking lines in the diagonal directions (adapted from Linderman et al. [14, 17]), (b) velocity vectors, and (c) temperature distribution in x_1 - x_3 mid-plane

6.5 Effective Thermal Conductivity of TIM

Based on the simulations, the effect of parameters such as particle loading, particle thermal conductivity and particle size on the thermal conductivity of the TIM can be predicted. Figure 6.8 presents the effect of volume fraction of solid particles on the effective thermal conductivity of TIM.

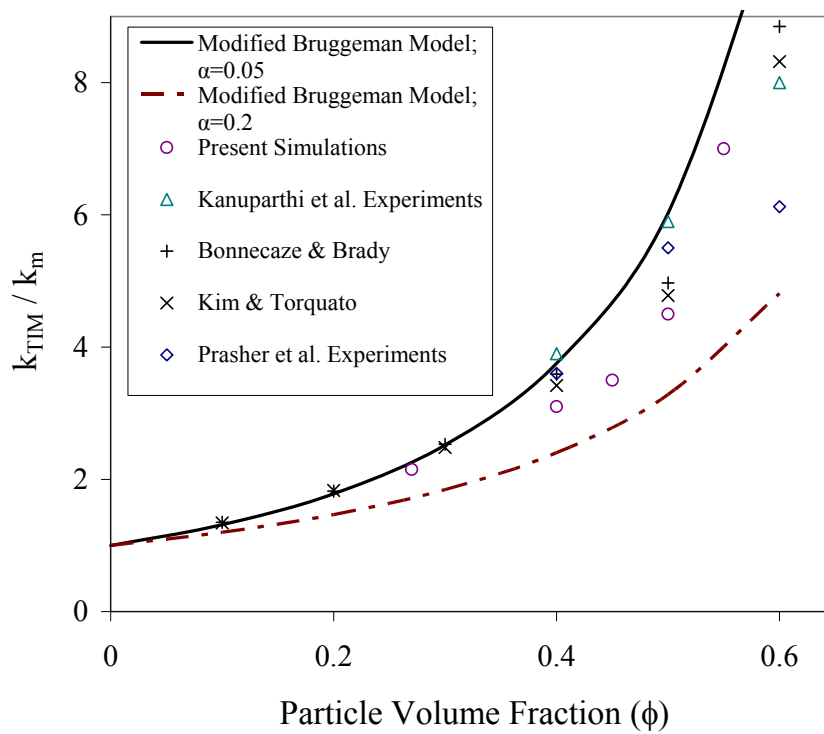


Figure 6.8. Effect of particle volume fraction on TIM effective thermal conductivity

It can be seen that the effective thermal conductivity increases with increasing particle loading due to the formation of highly conductive paths by filler particles. The

experimental results presented by Prasher et al. [19] and Kanuparthi et al. [119] are presented in this figure. In both experiments aluminum particle fillers have been used at $d=7.9$ and $8 \mu\text{m}$, respectively. Prasher et al. utilized a standard ASTM D5470 setup for thermal measurements. Kanuparthi et al. have used the laser flash diffusivity method (ASTM E-1461). The measured thermal resistances in these studies are the total value, which includes both the bulk resistance of the TIM layer, as well as interfacial contact resistances. The TIM to plate interfacial contact resistance is estimated by plotting thermal resistance versus BLT, and calculating the vertical intercept.

The results for random particle distributions presented by Kim and Torquato [117], and Bonnecaze and Brady [121], are also given. It is observed that the different approaches predict similar trends that indicate the thermal conductivity increases rapidly at volume fractions above 40%. These results are in good agreement with the experimental results by Prasher et al. [19] for the medium volume fraction. At sixty percent volume fraction the experimental k_{TIM} is about 40 percent less than the expected value based on the analytical relations, possibly due to the imperfect wetting of particles during mixing, or the experimental uncertainty. The results have been compared with the modified Bruggeman model [20]. In this model, assuming that the thermal conductivity of filler is much larger than the thermal conductivity of the matrix, the effective thermal conductivity of TIM is given by:

$$\frac{k_{TIM}}{k_m} = (1 - \phi)^{-3(1-\alpha)(1+2\alpha)} \quad (6.3)$$

Where, $\alpha = \frac{R_b k_m}{d}$ is the Biot number, d is the particle diameter and R_b denotes

the thermal resistance at the interface of filler particles and the matrix. R_b increases when the wetting of filler particles is not perfect. This may happen when the particle loading is high, or when the mixing is not perfect. In this model, the Biot number is an unknown parameter that needs to be estimated. Therefore, this kind of formulation can be used in qualitative studies of the performance of such mixtures in low to medium particle loading. Equation (6.3) shows that for a given Biot number, the effective thermal conductivity depends only on the particle volume fraction and not on particle distribution. The comparison between the simulation results and the presented model is based on using the volume fraction as the independent parameter.

6.5.1 Effect of Particle Size on TIM conductivity

The effect of particle size is investigated in Figure 6.9. The particle size is not effective in low and medium volume fractions. However, it is observed that at higher volume fractions mixtures containing larger particles have a higher effective thermal conductivity. On the other hand, the effect of particle size on the *BLT* needs to be considered in calculating thermal resistance. Considering the modified Bruggeman model, larger particle size is equivalent to smaller Biot number, which leads to higher thermal conductivity, assuming that the contact resistance is unchanged. The results are best estimated by the analytical model by choosing $\alpha=0.1$. The results given based on Nielsen model do not match well with the current predictions, especially at high particle loading.

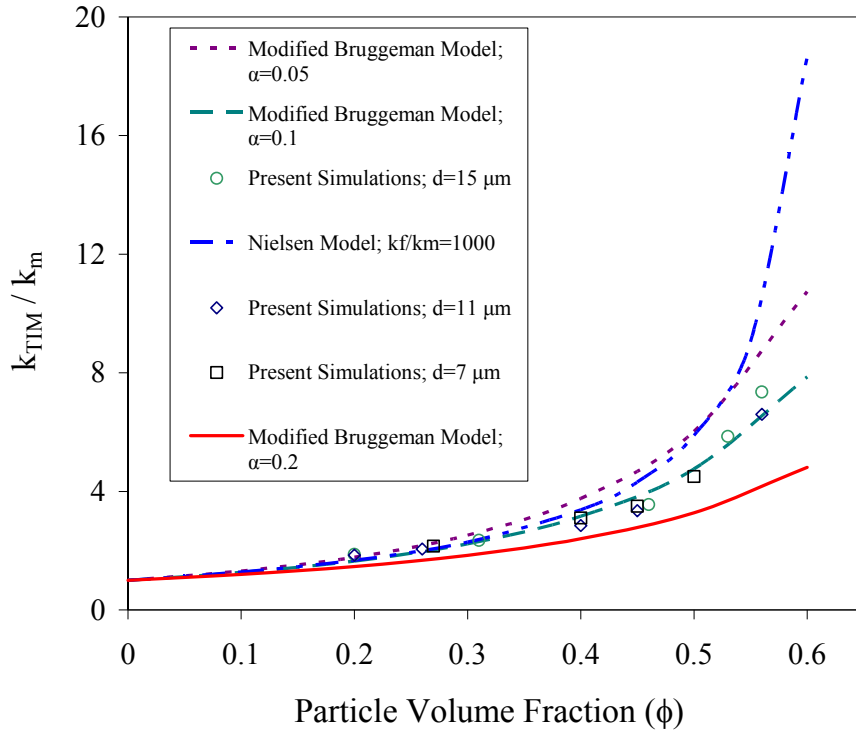


Figure 6.9. Effect of particle size on TIM effective thermal conductivity

6.5.2 Effect of Particle Shape on TIM conductivity

Figure 6.10 shows the effect of particle aspect ratio of elliptical particles on the effective conductivity at 20 percent particle loading. The TIM conductivity is normalized with the conductivity of TIM when $AR=1$. It is shown that TIM conductivity increases with increasing the aspect ratio. The case $AR=1$ is equivalent to cylindrical particles. When $AR<1$, the majority of particles are positioned such that their longer axis is perpendicular to the main heat flow direction. In this case the particle chains between the hot and cold plates require larger number of particles to form, compared to mixtures containing particles with higher aspect ratios. Therefore, the effective conductivity is

lower. The prediction of the Maxwell method is also presented in which a homogeneous and isotropic composite is considered. The effective conductivity is given by [107, 122]:

$$\frac{k_{TIM}}{k_m} = \frac{1 - \beta\phi}{1 + \beta\phi} \quad (6.4)$$

where β is given by: $\beta = \frac{(1 - r^2)(1 + AR)^2}{4(1 + AR.r)(AR + r)}$ and $r = \frac{k_f}{k_m}$ is the conductivity

ratio and AR is the aspect ratio of the particles.

The differential method is based on the Maxwell formulation. This formulation gives the effective conductivity implicitly. It considers a differential amount of inclusion in the base matrix and evaluates its effect based on the Maxwell method [123]. This process is repeated until the final formulation is obtained as:

$$\frac{1}{1 - \phi} = \left(\frac{k_{TIM}}{k_m} \right)^{2AR/(1+AR)^2} \frac{k_m - k_f}{k_{TIM} - k_f} \left(\frac{k_{TIM} + k_f}{k_m + k_f} \right)^{[(1-AR)/(1+AR)]^2} \quad (6.5)$$

Based on Figure 6.10 it is observed that there is a good agreement between this method and the present numerical results in this volume fraction. However, since the Maxwell method is for random distribution, the results for AR=0.5 and AR=2 are similar. Figure 6.11 shows the effect of particle aspect ratio on the effective conductivity at 40 percent particle loading. Comparing the numerical results with the Maxwell method, it is observed that the effective medium theory fails to accurately predict the effect of particle shape at high volume fractions. Specially, as aspect ratio increases the Maxwell method over estimates the TIM conductivity.

To further investigate the effect of particle shape and the accuracy of the effective medium based methods, the TIM conductivity for several aspect ratios and volume fractions is presented in Figure 6.12. It is seen that the effective medium based methods are not accurate in high volume fractions and over estimates the TIM conductivity. In this case the results of the Maxwell method and the differential method can be used in low and medium particle loading. However, in higher volume fractions they are not accurate. It suggests that the effective medium methods can be used for predicting the TIM conductivity when they are normalized based on a particular case.

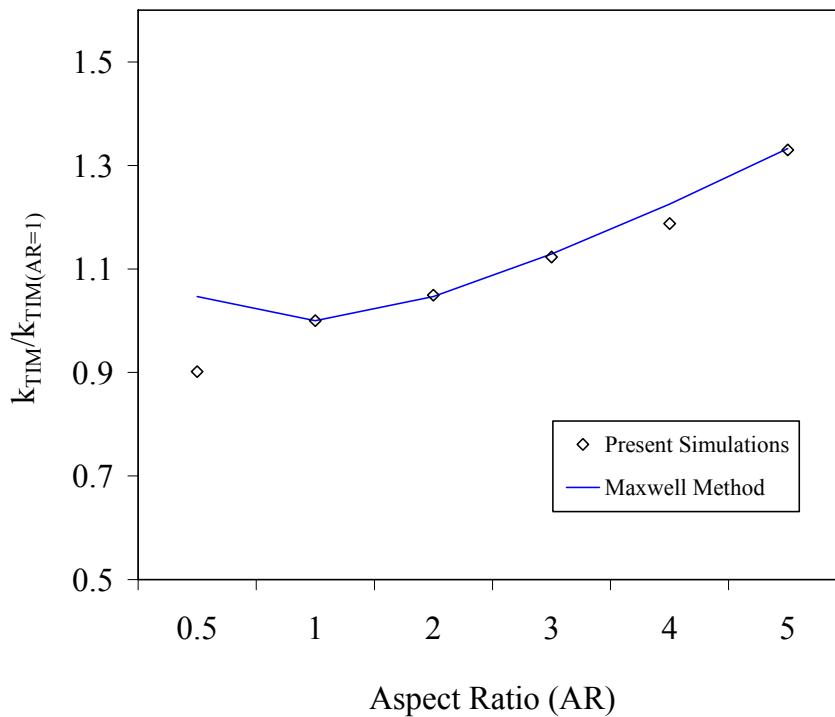


Figure 6.10. Effect of particle aspect ratio on TIM effective conductivity, $\phi=20\%$

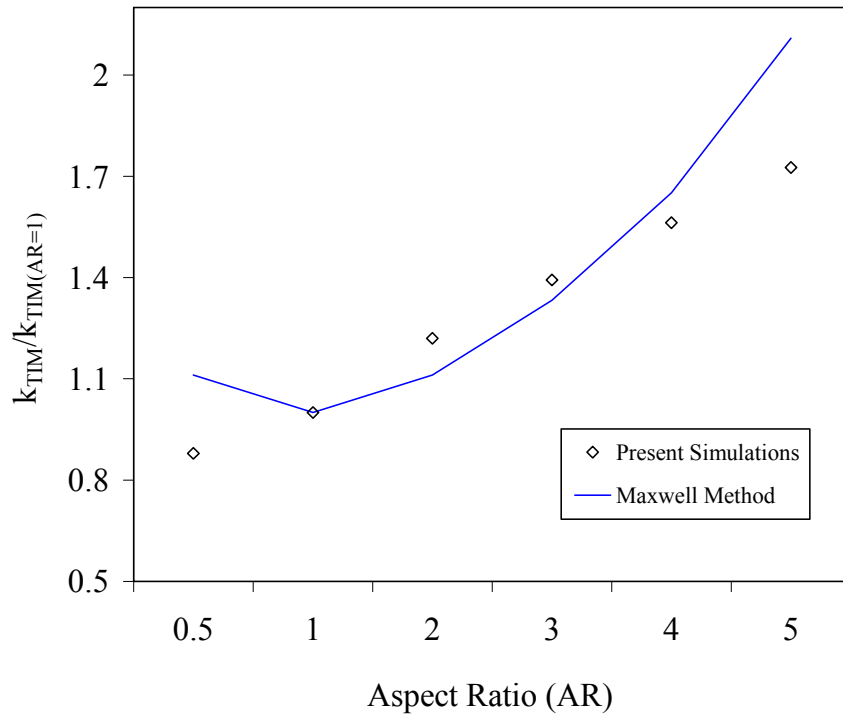


Figure 6.11. Effect of particle aspect ratio on TIM effective conductivity, $\phi=40\%$

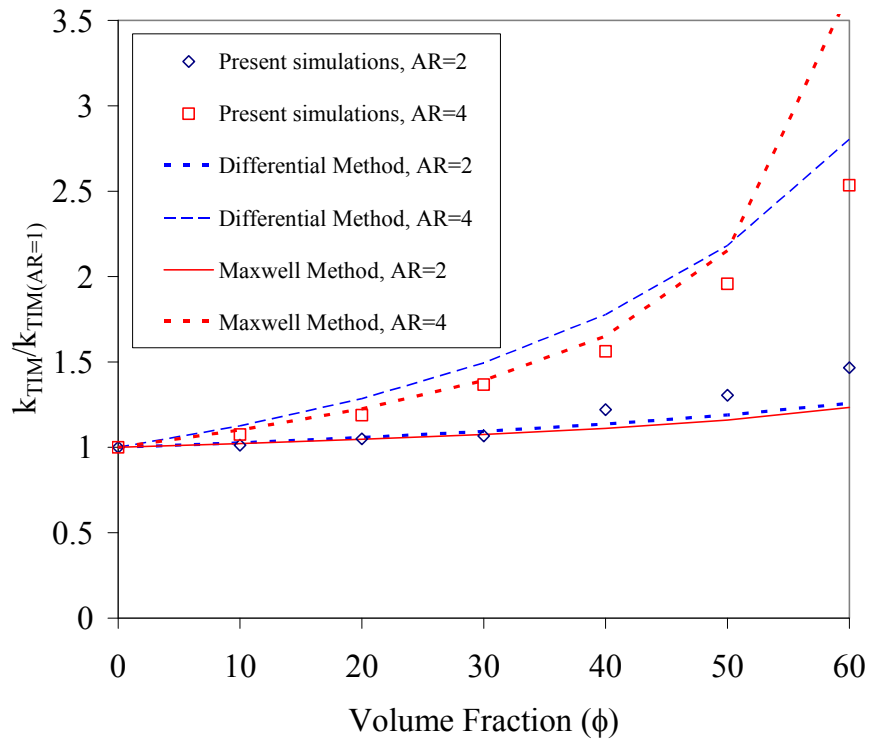


Figure 6.12. Effect of particle aspect ratio on TIM effective conductivity

6.5.3 Effect of Particle Conductivity on TIM conductivity

Figure 6.13 presents the effective thermal conductivity of TIM filled with particles with $d=11\mu\text{m}$ at different thermal conductivities. It is observed that the effective thermal conductivity of TIM increases with increasing thermal conductivity of the fillers. However, based on the Nielsen model [109], it is seen that when the thermal conductivity of the filler is much larger (>100 times) than the base fluid, increasing the thermal conductivity of the solid particles does not have a significant effect. Based on this model, the effective thermal conductivity is obtained as:

$$\frac{k_{TIM}}{k_m} = \frac{1 + AB\phi}{1 - \phi B\phi} \quad (6.6)$$

$$\text{Where, } B = \frac{k_f / k_m - 1}{k_f / k_m + A}, \quad \phi = 1 + \frac{(1 - \phi_{\max})\phi}{\phi_{\max}^2}, \quad A=1.5 \quad \text{and} \quad \phi_{\max}=0.637 \quad \text{for}$$

randomly packed spheres. Comparing the simulation results and the modified Bruggeman predictions with the Nielsen model it is evident that the Nielsen model is not realistic at high volume fractions and over estimates the thermal enhancement.

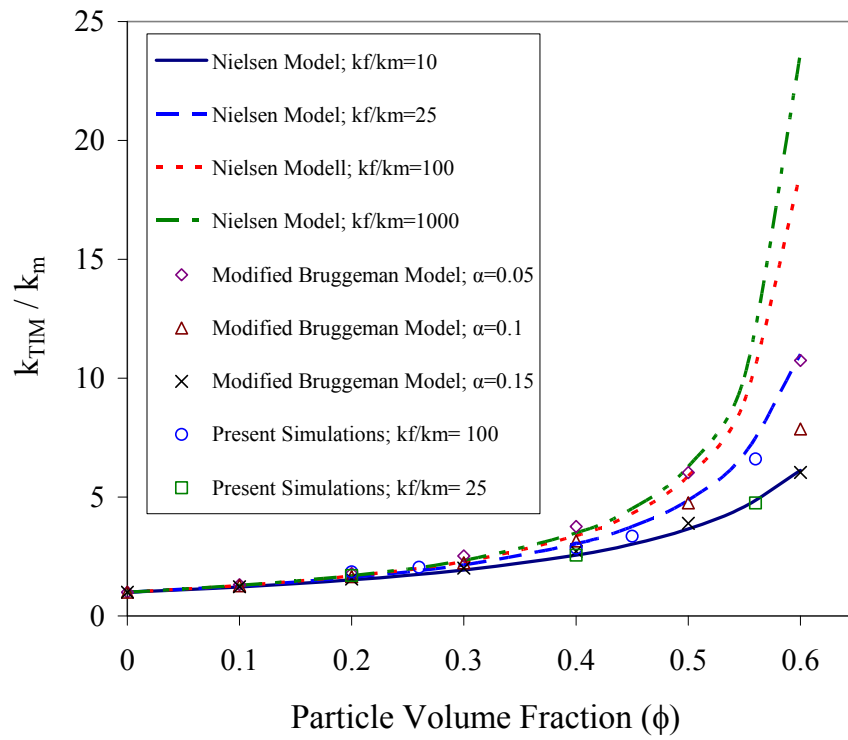


Figure 6.13. Effect of particle thermal conductivity on TIM effective thermal conductivity

CHAPTER 7

CONCLUDING REMARKS

In this research, a computational method based on Lattice-Boltzmann equation is developed for efficient simulation of fluid flow and heat transfer in complex geometries under transient conditions. The method presented here is based on solving the Lattice-Boltzmann equation for the fluid phase. It is coupled to the Newtonian dynamics equations to model the movement of particles and the energy equation to find the thermal properties in the fluid and solid phases. The flow and energy transport at particle scale are numerically predicted. This method is based on solving the basic conservation equations at particle scale and does not use any other models for predicting average suspension flow properties such as effective mixture viscosity or thermal conductivity. However, lubrication model is used to model inter-particle forces where particles are close to each other. This is a direct numerical simulation that models the free movement of the solid particles suspended in the flow and their effects on the temperature distribution. This is a robust and efficient computational method for the analysis of solid particles suspended in fluid. An advantage of the Lattice-Boltzmann method is that the code can be easily implemented on parallel processors because of the local nature of the time evolution operator.

The Lattice-Boltzmann method is described in Chapter 2. The developed thermal Lattice-Boltzmann method in the present research for modeling heat transfer in suspension flows is discussed. Sample problems and method validations are presented in Chapter 3. In section 3.2, the method used for parallel computations is described and the

infrastructure used in the large domain simulations is introduced. Benchmark studies show good scaling of the method on parallel systems. Large domain simulations are performed using parallel implementation of the numerical method. This method is used to simulate heat transfer in the systems that contain multi-component fluids including suspended particles.

Convective heat transfer in internal suspension flow is investigated in Chapter 4. The amount of thermal enhancement and the effect of different parameters on it is discussed. The results suggest that fluid flow disturbance due to movement of suspended particles near the channel walls is a critical factor in thermal enhancement in internal suspension flow. It affects the temperature gradient and results in local enhancements on heat transfer. The results show that at 5% volume fraction, the average performance is enhanced about 10%. The effect of particle volume fraction, size and thermal conductivity are investigated in section 4.4. It is observed that when $k_s/k_m > 50$, the thermal performance is not affected by conductivity of solids. Above this limit, thermal performance is enhanced 1% with 400% increase in thermal conductivity of solids. It is also observed that thermal performance is enhanced 1% with 30% increase in particle size.

In the second application, heat transfer in fiber suspensions during hot pressing in paper making process is studied in Chapter 5. The effects of efficient pre-heating on overall energy savings are discussed. It is shown that heat transfer enhancement in fiber suspension is essential in increasing the efficiency and energy savings in the paper making industry. The results show that the thermal properties are highly dependent on the

wood fiber types compared to fiber concentration or temperature. The effective thermal conductivity of fiber suspensions for three different wood fibers is calculated numerically. The effective thermal conductivity changes about 45% for suspensions of different softwood and hardwoods at 20-40% of solid fiber contents.

In Chapter 6, thermal properties of particle laden thermal interface materials are studied based on the micro-structure of the mixture. Squeeze flow of particle laden fluids is investigated numerically. The particle distribution is predicted based on practical conditions in the assembly of thermal components. The particles form low thermal resistance paths for heat transfer. The inter-particle distance is increased in horizontal plane and it is decreased in the main heat flow (vertical) direction. This affects the thermal properties and needs to be considered for realistic thermal predictions. The results show that effective thermal conductivity is enhanced 2-7 times at $\phi=55\%$ depending on particle size, shape, and conductivity. The results show that increasing particle aspect ratio results in thermal enhancement of up to 2.5 times at high ($\phi>50\%$) particle loading.

The main contributions from the current work are as following:

a) A numerical method is developed based on coupling Lattice-Boltzman equation, Newtonian dynamics equations and the energy equation. This method is especially useful to study heat transfer in complex and multi component particles. This method has all the advantages of Lattice Boltzmann method in simulating suspension flows. Additionally, the thermal calculations are performed based on first principles and the computational method is not complicated.

b) An efficient parallel computational model for large domain simulations of heat transfer in micro/nano multi-component fluids and fiber suspension flows is introduced based on the developed TLBM. Parallel implementation is performed using MPI method and benchmark studies on large computing clusters are performed.

c) The method is used to investigate the effect of suspended solid particles on local flow disturbances in forced internal flow. It has been shown that the particles have the most impact on local convective heat transfer in microchannel flow of suspensions.

d) The pre-heating process of fiber mixtures in paper making is investigated using numerical simulations. The advantage of the current method is that no experimental or semi-empirical modeling is used. Therefore, the predictions are more accurate and compare well with the existing experimental data. This provides an efficient method to predict thermal properties of fiber mixtures. The design parameters (such as energy supplying components in hot pressing or roll design) depend on these thermal properties. It is especially important considering the variety in wood fiber types that makes it difficult to do experiments for each individual case.

e) Thermal properties of particulate thermal interface materials are investigated based on the microstructure change during squeezing in assembly process. Particle distribution is an important factor in determining the thermal properties of solid suspensions. The previous numerical or analytical studies have examined arrangements such as simple cubic, body centered, face centered, or random. Here, utilizing squeeze flow simulations, we are able to generate the actual particle distribution resulting from a

given assembly process. Therefore, there is no need to assume pre-defined random distributions.

7.1 Recommended Future Work

In this section some recommended future work and possible extensions are discussed.

a) The current Thermal LBM does not include phase change simulations. However, it is possible to extend the method to cover phase change. It will need to use a multi-relaxation time LBM to be able to change the viscosity. This will provide a very useful numerical tool to directly simulate complex geometries which involve phase change. Especially it will be useful when the system includes a complex multi component of solid-liquid or gas-liquid mixtures.

b) The parallel implementation has been done for the current model based on MPI method. Although the benchmark studies show good performance, more efficiency studies may be needed to make the computations more efficient and less time consuming.

c) As outlined in Chapter 5, energy savings and heat transfer studies are very important in paper making process. An efficient and accurate numerical method to study the heat transfer process in impulse drying and evaporative drying is extremely useful. Therefore, further extensions of the method are required to simulate flexible fiber suspensions and to model phase change.

d) The method presented here provides the means and the general idea of predicting thermal properties of particulate TIMs based on particles microstructure during

practical conditions. The samples considered here are for solid fillers. The extension of this method to cover other types of TIMs such as CNT based TIMs is straightforward.

REFERENCES

- [1] M. Chopkar, P. K. Das and I. Manna, Synthesis and characterization of nanofluid for advanced heat transfer applications, *Scripta Materialia* 55 (6) (2006), 549-552.
- [2] P. Keblinski, S. R. Phillpot, S. U. S. Choi and J. A. Eastman, Mechanisms of heat flow in suspensions of nano-sized particles (nanofluids), *International Journal of Heat and Mass Transfer* 45 (4) (2002), 855-863.
- [3] J. V. Vadasz, S. Govender and P. Vadasz, Heat transfer enhancement in nanofluids suspensions: possible mechanisms and explanations, *International Journal of Heat and Mass Transfer* 48 (13) (2005), 2673-2683.
- [4] H. Xie, J. Wang, T. Xi and Y. Liu, Thermal Conductivity of Suspensions Containing Nanosized SiC Particles, *International Journal of Thermophysics* 23 (2) (2002), 571-580.
- [5] R. Prasher, W. Evans, P. Meakin, J. Fish, P. Phelan and P. Keblinski, Effect of aggregation on thermal conduction in colloidal nanofluids, *Applied Physics Letters* 89 (14) (2006), 143119.
- [6] N. Ce-Wen, R. Birringer, D. R. Clarke and H. Gleiter, Effective thermal conductivity of particulate composites with interfacial thermal resistance, *Journal of Applied Physics* 81 (10) (1997), 6692-6699.
- [7] R. Prasher, P. Bhattacharya and P. E. Phelan, Brownian-motion-based convective-conductive model for the effective thermal conductivity of nanofluids, *Journal of Heat Transfer* 128 (6) (2006), 588-595.
- [8] R. Prasher, P. Bhattacharya and P. E. Phelan, Thermal conductivity of nanoscale colloidal solutions (nanofluids), *Physical Review Letters* 94 (2) (2005), 025901.
- [9] P. Bhattacharya, S. K. Saha, A. Yadav, P. E. Phelan and R. S. Prasher, Brownian dynamics simulation to determine the effective thermal conductivity of nanofluids, *Journal of Applied Physics* 95 (11 I) (2004), 6492-6494.
- [10] Q. Z. Xue, Model for the effective thermal conductivity of carbon nanotube composites, *Nanotechnology* 17 (6) (2006), 1655-1660.
- [11] X. Qing-Zhong, Model for effective thermal conductivity of nanofluids, *Physics Letters A* 307 (5-6) (2003), 313-317.
- [12] J. Koo and C. Kleinstreuer, A new thermal conductivity model for nanofluids, *Journal of Nanoparticle Research* 6 (6) (2004), 577-588.

- [13] R. Prasher, Thermal interface materials: Historical perspective, status, and future directions, *Proceedings of the IEEE* 94 (8) (2006), 1571-1586.
- [14] R. J. Linderman, T. Brunswiler, U. Kloter, H. Toy and B. Michel, Hierarchical nested surface channels for reduced particle stacking and low-resistance thermal interfaces, *Annual IEEE Semiconductor Thermal Measurement and Management Symposium*, San Jose, CA, United States, 2007. p.87-94.
- [15] R. S. Prasher, P. Koning, J. Shipley and A. Devpura, Dependence of thermal conductivity and mechanical rigidity of particle-laden polymeric thermal interface material on particle volume fraction, *Journal of Electronic Packaging*, *Transactions of the ASME* 125 (3) (2003), 386-391.
- [16] Y. Xu, X. Luo and D. D. L. Chung, Sodium silicate based thermal interface material for high thermal contact conductance, *Journal of Electronic Packaging*, *Transactions of the ASME* 122 (2) (2000), 128-131.
- [17] T. Brunswiler, U. Kloter, R. J. Linderman, H. Rothuizen and B. Michel, Hierarchically nested channels for fast squeezing interfaces with reduced thermal resistance, *IEEE Transactions on Components and Packaging Technologies* 30 (2) (2007), 226-234.
- [18] P. Zhou and K. E. Goodson, Modeling and measurement of pressure-dependent junction-spreader thermal resistance for integrated circuits, *IMECE2001*, vol. 369, New York, NY, United States, American Society of Mechanical Engineers, New York, NY 10016-5990, United States, 2001. p.51-57.
- [19] R. S. Prasher, J. Shipley, S. Prstic, P. Koning and J.-L. Wang, Thermal resistance of particle laden polymeric thermal interface materials, *Journal of Heat Transfer* 125 (6) (2003), 1170-1177.
- [20] A. G. Every, Y. Tzou, D. P. H. Hasselman and R. Raj, The effect of particle size on the thermal conductivity of ZnS/diamond composites, *Acta Metallurgica et Materialia* 40 (1) (1992), 123-129.
- [21] S. Hou, Q. Zou, S. Chen and G. Doolen, Simulation of Cavity Flow by the Lattice Boltzmann Method, *Journal of Computational Physics* 118 (2) (1995), 329.
- [22] H. H. Hu, D. D. Joseph and M. J. Crochet, Direct simulation of fluid particle motions, *Theoretical and Computational Fluid Dynamics* 3 (5) (1992), 285-306.
- [23] H. Chen, S. Chen and W. H. Matthaeus, Recovery of Navier-Stokes equations using a lattice-gas Boltzmann method, *Physical Review A (Statistical Physics, Plasmas, Fluids, and Related Interdisciplinary Topics)* 45 (8) (1992), 5339-5342.
- [24] G. R. McNamara and G. Zanetti, Use of the Boltzmann equation to simulate lattice-gas automata, *Physical Review Letters* 61 (20) (1988), 2332-2335.

- [25] C. K. Aidun, Y. Lu and E. J. Ding, Direct analysis of particulate suspensions with inertia using the discrete Boltzmann equation, *Journal of Fluid Mechanics* 373 (1) (1998), 287-311.
- [26] F. J. Alexander, S. Chen and J. D. Sterling, Lattice Boltzmann thermohydrodynamics, *Physical Review E. Statistical Physics, Plasmas, Fluids, and Related Interdisciplinary Topics* 47 (4) (1993), 2249.
- [27] G. McNamara and B. Alder, Analysis of the lattice Boltzmann treatment of hydrodynamics, *Physica A: Statistical and Theoretical Physics* 194 (1-4) (1993), 218.
- [28] G. R. McNamara, A. L. Garcia and B. J. Alder, Stabilization of thermal lattice Boltzmann models, *Journal of Statistical Physics* 81 (1-2) (1995), 395-408.
- [29] P. Pavlo, G. Vahala and L. Vahala, Higher order isotropic velocity grids in lattice methods, *Physical Review Letters* 80 (18) (1998), 3960-3963.
- [30] P. Pavlo, G. Vahala, L. Vahala and M. Soe, Linear Stability Analysis of Thermo-Lattice Boltzmann Models, *Journal of Computational Physics* 139 (1) (1998), 79.
- [31] S. Chen and D. Doolen, Lattice Boltzmann method for fluid flows, In *Annual Review of Fluid Mechanics*, (1998).
- [32] J. G. M. Eggels and J. A. Somers, Numerical simulation of free convective flow using the lattice-Boltzmann scheme, *International Journal of Heat and Fluid Flow* 16 (5) (1995), 357.
- [33] X. Shan and G. Doolen, Multicomponent lattice-Boltzmann model with interparticle interaction, *Journal of Statistical Physics* 81 (1-2) (1995), 379-393.
- [34] A. Bartoloni, C. Battista, S. Cabasino, P. Paolucci, J. Pech, R. Sarno, G. M. Todesco, M. Torelli, W. Tross, P. Vicini, R. Benzi, N. Cabibbo, F. Massaioli and R. Tripicciono, LBE simulations of Rayleigh-Benard convection on the APE100 parallel processor, *International Journal of Modern Physics C (Physics and Computers)* 4 (5) (1993), 993-1006.
- [35] X. Shan, Simulation of Rayleigh-Benard convection using a lattice Boltzmann method, *Physical Review E (Statistical Physics, Plasmas, Fluids, and Related Interdisciplinary Topics)* 55 (3) (1997), 2780-2788.
- [36] X. He and L.-S. Luo, A priori derivation of the lattice Boltzmann equation, *Physical Review E (Statistical Physics, Plasmas, Fluids, and Related Interdisciplinary Topics)* 55 (6) (1997), 6333-6336.
- [37] T. Abe, Derivation of the lattice Boltzmann method by means of the discrete ordinate method for the Boltzmann equation, *Journal of Computational Physics* 131 (1) (1997), 241-246.

- [38] X. He, H. Chen and G. D. Doolen, A novel thermal model for the lattice Boltzmann method in incompressible limit, *Journal of Computational Physics* 146 (1) (1998), 282-300.
- [39] X. Shan, X.-F. Yuan and H. Chen, Kinetic theory representation of hydrodynamics: A way beyond the Navier-Stokes equation, *Journal of Fluid Mechanics* 550 (2006), 413-441.
- [40] Y. Shi, T. S. Zhao and Z. L. Guo, Thermal lattice Bhatnagar-Gross-Krook model for flows with viscous heat dissipation in the incompressible limit, *Physical Review E - Statistical, Nonlinear, and Soft Matter Physics* 70 (6 2) (2004), 066310.
- [41] Z. Guo, C. Zheng, B. Shi and T. S. Zhao, Thermal lattice Boltzmann equation for low Mach number flows: Decoupling model, *Physical Review E - Statistical, Nonlinear, and Soft Matter Physics* 75 (3) (2007), 036704.
- [42] G. Gonnella, A. Lamura and V. Sofonea, Lattice Boltzmann simulation of thermal nonideal fluids, *Physical Review E (Statistical, Nonlinear, and Soft Matter Physics)* 76 (3) (2007), 1-5.
- [43] X. Nie, X. Shan and H. Chen, Thermal lattice Boltzmann model for gases with internal degrees of freedom, *Physical Review E - Statistical, Nonlinear, and Soft Matter Physics* 77 (3) (2008), 035701.
- [44] G. H. Tang, W. Q. Tao and Y. L. He, Thermal boundary condition for the thermal lattice Boltzmann equation, *Physical Review E - Statistical, Nonlinear, and Soft Matter Physics* 72 (1) (2005), 016703.
- [45] X. Shan and H. Chen, Simulation of nonideal gases and liquid-gas phase transitions by the lattice Boltzmann equation, *Physical Review E (Statistical Physics, Plasmas, Fluids, and Related Interdisciplinary Topics)* 49 (4) (1994), 2941-2948.
- [46] M. R. Swift, E. Orlandini, W. R. Osborn and J. M. Yeomans, Lattice Boltzmann simulations of liquid-gas and binary fluid systems, *Physical Review E. Statistical Physics, Plasmas, Fluids, and Related Interdisciplinary Topics* 54 (5) (1996), 5041.
- [47] K. Kono, T. Ishizuka, H. Tsuda and A. Kurosawa, Application of lattice Boltzmann model to multiphase flows with phase transition, *Computer Physics Communications* 129 (1) (2000), 110-120.
- [48] T. Lee and C.-L. Lin, Pressure evolution lattice-Boltzmann-equation method for two-phase flow with phase change, *Physical Review E* 67 (5 2) (2003), 056703-056701.
- [49] T. Lee and C.-L. Lin, A stable discretization of the lattice Boltzmann equation for simulation of incompressible two-phase flows at high density ratio, *Journal of Computational Physics* 206 (1) (2005), 16-47.

- [50] B. J. Palmer and D. R. Rector, Lattice-Boltzmann algorithm for simulating thermal two-phase flow, *Physical Review E (Statistical Physics, Plasmas, Fluids, and Related Interdisciplinary Topics)* 61 (5) (2000), 5295-5306.
- [51] W.-S. Jiaung, J.-R. Ho and C.-P. Kuo, Lattice Boltzmann method for the heat conduction problem with phase change, *Numerical Heat Transfer, Part B (Fundamentals)* 39 (2) (2001), 167-187.
- [52] C. Huber, A. Parmigiani, B. Chopard, M. Manga and O. Bachmann, Lattice Boltzmann model for melting with natural convection, *International Journal of Heat and Fluid Flow* 29 (5) (2008), 1469-1480.
- [53] R. H. Khiabani, Y. Joshi and C. K. Aidun, Heat transfer characteristics of suspension flow inside a microchannel, *IMECE2007*, Seattle, Washington, USA, 2007.
- [54] R. H. Khiabani, Y. Joshi and C. K. Aidun, Heat transfer in microchannels with suspended solid particles: Lattice-Boltzmann based computations, *ASME Journal of Heat Transfer* 132 (4) (2010).
- [55] H. K. Versteeg and W. Malalasekera, *An introduction to computational fluid dynamics : the finite volume method 1st ed.*, Longman Ltd, London, 1995.
- [56] E.-J. Ding and C. K. Aidun, Extension of the Lattice-Boltzmann method for direct simulation of suspended particles near contact, *Journal of Statistical Physics* 112 (314) (2003), 685-708.
- [57] J. R. Clausen and C. K. Aidun, Galilean invariance in the lattice-Boltzmann method and its effect on the calculation of rheological properties in suspensions, *International Journal of Multiphase Flow* 35 (4) (2009), 307-311.
- [58] R. M. MacMeccan, J. R. Clausen, G. P. Neitzel and C. K. Aidun, Simulating deformable particle suspensions using a coupled lattice-Boltzmann and finite-element method, *Journal of Fluid Mechanics* 618 (2009), 13-39.
- [59] C. K. Aidun and J. R. Clausen, Lattice-Boltzmann method for complex flows, *Annual Review of Fluid Mechanics* 42 (2010), 439-472.
- [60] R. Hilpert, Waermeabgabe von geheizten Draechten und Rohren im Luftstrom, *Forschungsarbeiten auf dem Gebiete des Ingenieurwesens -- Ausgabe B* 4 (5) (1933), 215-224.
- [61] S. Mettu, N. Verma and R. P. Chhabra, Momentum and heat transfer from an asymmetrically confined circular cylinder in a plane channel, *Heat and Mass Transfer* 42 (11) (2006), 1037-1048.
- [62] W. A. Khan, J. R. Culham and M. M. Yovanovich, Fluid flow and heat transfer from a cylinder between parallel planes, *Journal of Thermophysics and Heat Transfer* 18 (3) (2004), 395-403.

- [63] <http://www.ncsa.illinois.edu/UserInfo/Resources/Hardware/TGIA64LinuxCluster>, April, 2010.
- [64] <http://www.rcac.purdue.edu/userinfo/resources/steele>, April, 2010.
- [65] R. K. Shah and A. L. London, *Laminar flow forced convection in ducts*, ed., Academic Press, New York, 1978.
- [66] T. C. Hung and C. S. Fu, Conjugate heat transfer analysis for the passive enhancement of electronic cooling through geometric modification in a mixed convection domain, *Numerical Heat Transfer, Part A (Applications)* 35 (5) (1999), 519-535.
- [67] Y. Wang and A. J. Ghajar, Effect of component geometry and layout on flow distribution for surface mounted electronic components. A smoke flow visualization study, 183 (1991), 25-31.
- [68] M. H. Saidi and R. H. Khiabani, Forced convective heat transfer in parallel flow multilayer microchannels, *ASME Journal of Heat Transfer* 129 (9) (2007), 1230-1236.
- [69] C. K. Aidun and S. P. Lin, Large amplitude modulation of heat transfer from a circular cylinder, *International Journal of Heat and Mass Transfer* 30 (2) (1987), 405-408.
- [70] C. K. Aidun and S. P. Lin, conjugate heat transfer from a hollow cylinder *Proceedings of the International Heat Transfer Conference*, vol. 2, San Francisco, CA, USA, Hemisphere Publ Corp, Washington, DC, USA, 1986. p.373-378.
- [71] S. C. R. Dennis, J. D. Hudson and N. Smith, Steady laminar forced convection from a circular cylinder at low Reynolds numbers, *Physics of Fluids* 11 (5) (1968), 933-934.
- [72] S. Nakagawa, M. Senda, S. Kikkawa, H. Wakasugi and A. Hiraide, Heat transfer in channel flow around a rectangular cylinder, *Heat Transfer - Japanese Research* 27 (1) (1998), 84-97.
- [73] A. Sharma and V. Eswaran, Effect of channel-confinement and aiding/opposing buoyancy on the two-dimensional laminar flow and heat transfer across a square cylinder, *International Journal of Heat and Mass Transfer* 48 (25-26) (2005), 5310-5322.
- [74] H.-W. Wu, S.-W. Perng, S.-Y. Huang and T.-C. Jue, Transient mixed convective heat transfer predictions around three heated cylinders in a horizontal channel, *International Journal of Numerical Methods for Heat and Fluid Flow* 16 (6) (2006), 674-692.
- [75] W. S. Fu and S. J. Yang, Numerical simulation of heat transfer induced by a body moving in the same direction as flowing fluids, *Heat and Mass Transfer* 36 (3) (2000), 257-264.

- [76] W. S. Fu and B. H. Tong, Numerical investigation of heat transfer of a heated channel with an oscillating cylinder, *Numerical Heat Transfer; Part A: Applications* 43 (6) (2003), 639-658.
- [77] C. Gau, J. M. Wu and C. Y. Liang, Heat transfer enhancement and vortex flow structure over a heated cylinder oscillating in the crossflow direction, *Transactions of the ASME. Journal of Heat Transfer* 12 (4) (1999), 789-795.
- [78] B. S. V. Patnaik, Y. T. K. Gowda, M. S. Ravisankar, P. A. A. Narayana and K. N. Seetharamu, Finite element simulation of internal flows with heat transfer using a velocity correction approach, *Sadhana - Academy Proceedings in Engineering Sciences* 26 (3) (2001), 251-283.
- [79] J. J. Stickel and R. L. Powell, Fluid mechanics and rheology of dense suspensions, *Annual Review of Fluid Mechanics* 37 (2005), 129-149.
- [80] D. Semwogerere, J. F. Morris and E. R. Weeks, Development of particle migration in pressure-driven flow of a Brownian suspension, *Journal of Fluid Mechanics* 581 (2007), 437-451.
- [81] M. Frank, D. Anderson, E. R. Weeks and J. F. Morris, Particle migration in pressure-driven flow of a Brownian suspension, *Journal of Fluid Mechanics* 493 (493) (2003), 363-378.
- [82] T. C. Maloney, On the pore structure and dewatering properties of the pulp fiber cell wall, *Acta Polytechnica Scandinavica, Chemical Technology Series* (275) (2000), 2-45.
- [83] E. L. Back and L. I. Andersson, Effect of Temperature on Wet-Web Strength Properties, *TAPPI Journal* 76 (5) (1993), 164-172.
- [84] J. D. Lindsay, New Drying and Dewatering Processes in Papermaking, In *IPST Technical Paper Series*, (1990).
- [85] K. Walker, Advances in Hot-Pressing Technology, *TAPPI Journal* 73 (8) (1990), 99-101.
- [86] J. W. Crouse, Y. D. Woo and C. H. Sprague, Delamination - Stumbling Block to Implementing Impulse Drying Technology for Linerboard, *TAPPI Journal* 72 (10) (1989), 211-215.
- [87] R. Krook and S. Stenstrom, Temperature gradients and heat flux measurements in hot pressing of paper, *Experimental Heat Transfer* 11 (3) (1998), 221-240.
- [88] L. H. Busker and D. C. Cronin The relative importance of wet press variables in water removal, *Pulp and Paper Canada* 85 (6) (1984), 87-101.

- [89] T. Patterson, M. A. Strand and D. I. Orloff, An apparatus for the evaluation of web-heating technologies: Development, capabilities, preliminary results, and potential uses, *Tappi journal* 79 (3) (1996), 269-278.
- [90] B. M. Suleiman, J. Larfeldt, B. Leckner and M. Gustavsson, Thermal conductivity and diffusivity of wood, *Wood Science and Technology* 33 (6) (1999), 465-473.
- [91] O. A. Plumb, G. A. Spolek and B. A. Olmstead, Heat and mass transfer in wood during drying, *International Journal of Heat and Mass Transfer* 28 (9) (1985), 1669-1678.
- [92] H. Paulapuro and L. Nordman, Wet pressing. History and future trends, *Pulp & Paper Canada* 92 (1) (1991), 41-50.
- [93] L. M. H. Carvalho and C. A. V. Costa, Modeling and simulation of the hot-pressing process in the production of medium density fiberboard (MDF), *Chemical Engineering Communications* 170 (1998), 1-21.
- [94] C. Pereira, L. M. H. Carvalho and C. A. V. Costa, Modeling the continuous hot-pressing of MDF, *Wood Science and Technology* 40 (4) (2006), 308-326.
- [95] H. A. Ribeiro and C. A. V. Costa, Modeling and simulation of the hot-pressing process in paper production: A heat- and mass-transfer analysis, *Industrial and Engineering Chemistry Research* 46 (24) (2007), 8205-8219.
- [96] F. W. Ahrens, Heat transfer aspects of hot surface drying at high temperature and mechanical loading *Journal of Pulp and Paper Science* 9 (3) (1983), 79-83.
- [97] J. D. Lindsay, A. Haberl and D. Poirier, Potential for Higher Drying Rates in Cylinder Drying of Paper, In *IPST Technical Paper Sereries*, (1992).
- [98] J. Nilsson and S. Stenstrom, Modelling of heat transfer in hot pressing and impulse drying of paper, *Drying Technology* 19 (10) (2001), 2469-2485.
- [99] B. G. Zombori, F. A. Kamke and L. T. Watson, Simulation of the internal conditions during the hot-pressing process, *Wood and Fiber Science* 35 (1) (2003), 2-23.
- [100] C. Dai and C. Yu, Heat and mass transfer in wood composite panels during hot-pressing: Part I. A physical-mathematical model, *Wood and Fiber Science* 36 (4) (2004), 585-597.
- [101] C. Dai, C. Yu and X. Zhou, Heat and mass transfer in wood composite panels during hot pressing. Part II. Modeling void formation and mat permeability, *Wood and Fiber Science* 37 (2) (2005), 242-257.
- [102] H. Thoemen and P. E. Humphrey, Modeling the physical processes relevant during hot pressing of wood-based composites. Part I. Heat and mass transfer, *Holz als Roh - und Werkstoff* 64 (1) (2006), 1-10.

- [103] H. Thoemen, T. Walther and A. Wiegmann, 3D simulation of macroscopic heat and mass transfer properties from the microstructure of wood fibre networks, *Composites Science and Technology* 68 (3-4) (2008), 608-616.
- [104] H. P. Steinhagen, Thermal Conductive Properties of Wood, Green or Dry, from minus 40 degree to plus 100 degree C: A Literature Review, USDA Forest Service General Technical Report FPL (Forest Products Laboratory) (1977).
- [105] F. P. Incropera and D. P. DeWitt, Introduction to heat transfer 3ed., New York : Wiley, 1996.
- [106] N. Goel, T. K. Anoop, A. Bhattacharya, J. A. Cervantes, R. K. Mongia, S. V. Machiroutu, L. Hau-Lan, H. Ya-Chi, F. Kuang-Cheng, D. Bar-Long, L. Chen-Hua, L. Chun-Hung, T. Chi-Wei and J. H. Pan, Technical review of characterization methods for thermal interface materials (TIM), 2008 11th Intersociety Conference on Thermal and Thermomechanical Phenomena in Electronic Systems (ITHERM '08), Piscataway, NJ, USA, 2008. p.248-258.
- [107] J. C. Maxwell, A treatise on electricity and magnetism, 2nd ed., Oxford, Clarendon Press, 1873.
- [108] Z. Hashin and S. Shtrikman, Variational approach to theory of elastic behaviour of multiphase materials, *Journal of Mechanics and Physics of Solids* 11 (2) (1963), 127-140.
- [109] L. E. Nielsen, The thermal and electrical conductivity of two-phase systems, *Industrial and Engineering Chemistry, Fundamentals* 13 (1) (1974), 17-20.
- [110] P. E. Phelan and R. C. Niemann, Effective thermal conductivity of a thin, randomly oriented composite material, *Journal of Heat Transfer* 120 (4) (1998), 971-976.
- [111] R. C. McPhedran and D. R. McKenzie, The conductivity of lattices of spheres. I. The simple cubic lattice, *Proceedings of the Royal Society of London, Series A (Mathematical and Physical Sciences)* 359 (1696) (1978), 45-63.
- [112] D. R. McKenzie, R. C. McPhedran and G. H. Derrick, The conductivity of lattices of spheres. II. The body centred and face centred cubic lattices, *Proceedings of the Royal Society of London, Series A (Mathematical and Physical Sciences)* 362 (1709) (1978), 211-232.
- [113] L. Rayleigh, On the influence of obstacles arranged in rectangular order upon the properties of a medium, *Philosophical Magazine* 34 (1892), 481-502.
- [114] S. Torquato, Effective electrical conductivity of two-phase disordered composite media, *Journal of Applied Physics* 58 (10) (1985), 3790-3797.

- [115] D. C. Pham and S. Torquato, Strong-contrast expansions and approximations for the effective conductivity of isotropic multiphase composites, *Journal of Applied Physics* 94 (10) (2003), 6591-6602.
- [116] I. C. Kim and S. Torquato, Determination of the effective conductivity of heterogeneous media by Brownian motion simulation, *Journal of Applied Physics* 68 (8) (1990), 3892-3903.
- [117] I. C. Kim and S. Torquato, Effective conductivity of suspensions of hard spheres by Brownian motion simulation, *Journal of Applied Physics* 69 (4) (1991), 2280-2289.
- [118] I. C. Kim and S. Torquato, Effective conductivity of suspensions of overlapping spheres, *Journal of Applied Physics* 71 (6) (1992), 2727-2735.
- [119] S. Kanuparthi, M. Rayasam, G. Subbarayan, B. Sammakia, A. Gowda and S. Tonapi, Hierarchical field compositions for simulations of near-percolation thermal transport in particulate materials, *Computer Methods in Applied Mechanics and Engineering* 198 (5-8) (2009), 657-668.
- [120] R. T. Bonnecaze and J. F. Brady, A method for determining the effective conductivity of dispersions of particles, *Proceedings of the Royal Society of London, Series A (Mathematical and Physical Sciences)* 430 (1879) (1990), 285-313.
- [121] R. T. Bonnecaze and J. F. Brady, The effective conductivity of random suspensions of spherical particles, *Proceedings of the Royal Society of London, Series A (Mathematical and Physical Sciences)* 432 (1886) (1991), 445-465.
- [122] R. W. Zimmerman, Effective conductivity of a two-dimensional medium containing elliptical inhomogeneities, *Proceedings of the Royal Society of London, Series A: Mathematical, Physical and Engineering Sciences* 452 (1950) (1996), 1713-1727.
- [123] R. McLaughlin, A study of the differential scheme for composite materials, *International Journal of Engineering Science* 15 (4) (1977), 237-244.